Novel SMA Dowel Connections For Seismically Resilient Timber Buildings

by

Maxime Daniel Cléroux

A thesis

presented to the University of Waterloo

in fulfillment of the

thesis requirement for the degree of

Master of Applied Science

in

Civil Engineering

Waterloo, Ontario, Canada, 2022

AUTHOR'S DECLARATION

I hereby declare that I am the sole author of this thesis. This is a true copy of the thesis, including any required final revisions, as accepted by my examiners.

I understand that my thesis may be made electronically available to the public.

Abstract

The trend towards sustainable construction practices has led to a growing demand for mid- to high-rise mass timber structures and a growing interest in their behaviour during earthquakes. Due to the brittle nature of wood, timber-based seismic force resisting systems (SFRSs) rely on connections to dissipate energy; these connections effectively act as a ductile energy-dissipative fuse in extreme loading events. Ductile timber connections traditionally fail from a combination of yielding of fasteners and the crushing of wood below the fasteners. While this ensures ductile behaviour, seismic resilience is an increasingly desired trait in SFRSs. Seismically resilient systems seek to reduce or eliminate all disruptions to occupants caused by an earthquake, which can be achieved by designing easily replaceable fuses that absorb permanent damage, or through the design of self-centering systems.

Recently, superelastic shape memory alloys (SMAs) have garnered interest in the construction industry for their potential use in resilient self-centering structural systems. Superelasticity is a property which enables a material to recover large strains with no permanent damage. The overarching aim of the current study is to investigate the effectiveness of using superelastic nickel-titanium (NiTi) SMA bars as slender fasteners in timber dowel-type connections to create a self-centering connection for braced timber frames (BTFs).

Initially, the self-centering ability of the SMA bars in bending was evaluated by performing cyclic three-point bending tests on the SMA bars. The performance of SMA bars used as straight dowels in a single fastener wood-steel-wood connection was investigated and compared to the behaviour of a traditional steel dowel using the same connection detail. These single dowel tests were modelled in Abaqus, and modelling results showed good agreement with experimental results. Then, the SMA bars were threaded and used in a four-bolt wood-steel-wood connection that was tested in monotonic and cyclic loading. These tests were also performed with traditional ASTM A307 bolts to compare connection behaviour to the current industry standard.

The SMA dowel and bolted connections both showed great self-centering abilities and increased strength when compared to connections with traditional steel fasteners. However, the NiTi alloys used in this study showed a tendency to shear suddenly at the wood-steel interface. Additionally, the higher bending strength of the NiTi alloys led to slightly greater wood crushing compared to connections with traditional steel fasteners. While the great self-centering effect of the SMA fasteners show promise for the use of SMAs in connections, it is recommended that further research be conducted on the fatigue behaviour of NiTi dowels in cyclic shear. Additionally, dowel-type fasteners employing a different superelstic alloy, such as iron-based SMAs, should be investigated as they become available. While these alloys are currently still in development, they could be an inexpensive alternative to NiTi with cyclic shear behaviour that is better suited for dowel-type fasteners.

Acknowledgements

The completion of this degree would not have been possible without the help and support of many individuals. First, I'd like to thank my two supervisors, Drs. Eugene Kim and Daniel Lacroix for their guidance, patience, and support over the last two years. Your commitment to meeting with me weekly and always being there to answer questions was greatly appreciated. Graduate school is not easy but having amazing supervisors like you makes the workload and stress a lot more tolerable. I look forward to staying in touch with you both. I would also like to thank Yannick Vetter for all the laughs, as well as his help completing my lab work.

To my girlfriend Shelby, I'm grateful for your love and support while I finished school. I look forward to this next chapter of my life with you. Lastly, to my parents, sister, and grandparents, thank you for your unconditional love and support in all that I do; I love you all very much!

Table of Contents

List of Figures

List of Tables

Chapter 1 - Introduction

1.1   Research Needs

The substitution of conventional building materials with mass timber has been shown to reduce construction phase CO_2 emissions by an average of 69% (Himes & Busby, 2020). Consequently, recent efforts towards achieving carbon neutrality are driving a rising demand for mid- to high-rise mass timber buildings. As taller buildings are constructed using mass timber products such as glue-laminated timber (glulam) and cross-laminated timber (CLT), the need to develop an understanding of the behaviour of timber structures under earthquake loads becomes increasingly critical. The high strength-to-weight ratio of wood makes it a favorable material in high seismic zones, as lower building weight results in lower seismic design forces. However, the brittle failure modes associated with this natural material leads to challenges that must be overcome through creative design and innovations.

To achieve ductile seismic force resisting systems (SFRSs), the adoption of a capacity-based design approach is essential. This approach enables designers to ensure that brittle structural components remain elastic while inelastic deformations occur in specifically designed ductile elements. In steel structures, this typically entails designing strong connections with a higher capacity than the steel members they support (Popovski & Karacabeyli, 2008), since members like steel beams in bending have significant ductility and deformation capacity. In contrast, due to the brittle nature of wood, connections in timber SFRSs must be designed with a lower capacity than the members they support, as the connections make use of steel fasteners which behave in a ductile manner (Popovski & Karacabeyli, 2008).

One of the most efficient wood-based SFRSs that can be used in mass timber buildings consists of braced timber frames (BTFs). In BTFs, dowel-type timber connections are heavily relied upon to dissipate seismic energy and ensure that the deformations occur at the connection level. To effectively act as a ductile structural fuse, these connections need to be designed to deform as a combination of fastener yielding and embedment into wood: two deformation modes which do not lead to sudden failures. While this is an efficient way to ensure life safety in the case of seismic events, there is a growing desire for structures to remain functional following extreme loading events. The concept of sustained functionality of a building after extreme loading, often referred to as *resilience*, is one of the main motivations for this study. In fact, this research seeks to fulfill a need for resilient BTF connections that can easily be designed and installed in mass timber buildings.

Shape memory alloys (SMAs) possess unique characteristics that make them appealing for applications in resilient structural systems. One property of SMAs, commonly known as superelasticity, allows the material to undergo large displacements without any permanent deformations. The research presented in this thesis seeks to exploit this unique property to develop simple dowel-type connections which have

limited permanent damage after being subject to large displacements. The use of SMA round bars as fasteners in the wood-steel-wood connections commonly found in BTFs is critical to the development of a resilient wood-based SFRS that is simple to design, manufacture, and assemble.

1.2 Objectives

The overarching aim of this study is to investigate experimentally and analytically the potential of a shape-memory-alloy (SMA) dowel-type connection for braced timber frames (BTFs) that is simple to design and non-intrusive to the aesthetics of traditional BTFs. This novel connection seeks to provide BTFs with improved seismic resilience compared to BTFs with traditional dowel-type connections through the self-centering abilities inherent to SMAs. Of particular interest in the current study is the experimental and analytical behaviour of the SMA connection in the diagonal brace. The global response of the BTF with SMA dowels will be investigated in further studies. The BTF configuration and detailing in Figure 1.1 is representative of what is commonly found in mass timber buildings. Traditionally, the diagonal brace uses steel bolts (dowels), rivets, or self-tapping screws in lieu of SMA dowels.

a) Typical BTF

b) BTF Connection Cross-Section
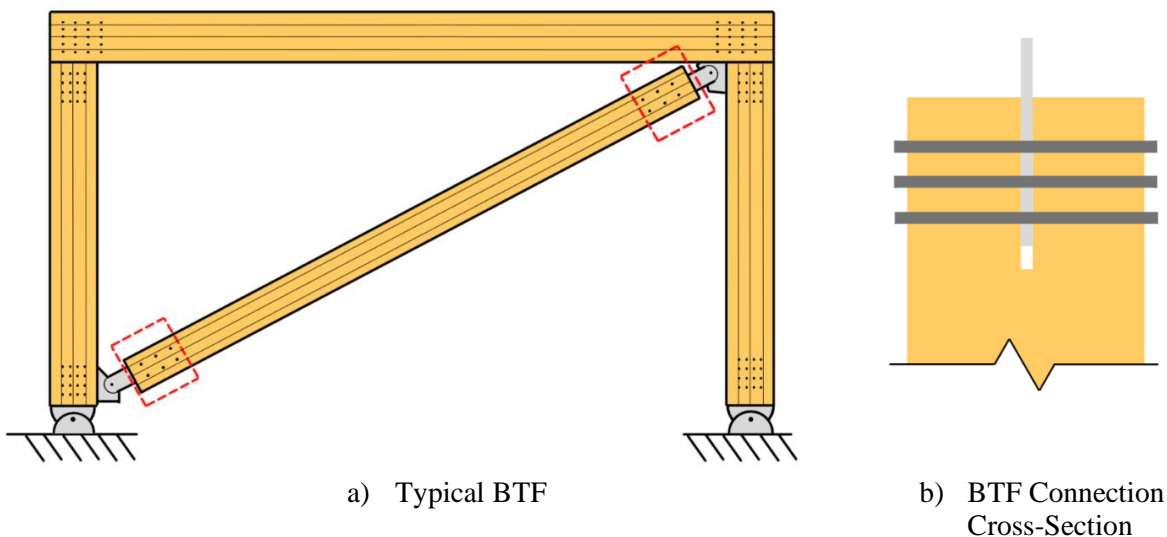
Figure 1.1: Typical BTF and the Connections of Interest

To investigate the performance of SMA dowels in wood-steel-wood connections (Figure 1.1), the following sub-objectives have been defined:

1. Experimentally evaluate the self-centering ability of SMA bars in bending in comparison to traditional steel fasteners with the same diameter.

2. Experimentally investigate the material behaviour of smooth SMA and steel dowels free of threads, nuts, and washers in single dowel wood-steel-wood connections under monotonic and cyclic loading.

3. Experimentally investigate the monotonic and cyclic behaviour of wood-steel-wood connections with a group of SMA dowels and steel bolts that are fastened to the specimens using nuts and washers, representative of conventional construction practices when employing bolted connections in BTFs.

4. Develop a finite element model capable of predicting the behaviour of steel and SMA dowel wood-steel-wood connections. The predicted force-displacement curves will be compared to the experimental results.

5. Evaluate the feasibility of using SMAs as dowels in BTF connections by comparing the behaviour of the SMAs to the traditional alternatives (i.e., steel bolts). Make suggestions regarding the use of SMAs as dowels in BTF connections and the possibilities for future work on this topic including other potential applications of SMAs in wood-based SFRSs.

1.3 Thesis Organization

This thesis is divided into seven chapters; the information presented in each chapter is summarized in this section.

Chapter 1 consists of a brief introduction of the research topic. The relevance of the research being conducted is justified in the context of trends in the construction industry, such as mass timber buildings, seismic design, and resilient structural systems.

Chapter 2 provides a literature review. The main topics covered in this section include general information on wood as a material, timber dowel-type connections, typical wood-based SFRSs, the concept of structural resilience, and the properties of SMAs along with a review of resilient structural systems developed using SMAs.

Chapter 3 presents the methods used to develop the experimental program. This includes the results of three-point bending tests of fasteners, embedment tests on wood, and monotonic and cyclic testing of connections with various types of dowels.

Chapter 4 presents experimental results for material tests and full connection tests introduced in Chapter 3.

Chapter 5 presents a three-dimensional (3D) finite element model developed to replicate the experimental results of wood-steel-wood dowel type connections. Force-displacement relationships are extracted from the model for comparison to the experimental results.

Chapter 6 discusses the findings from the experimental and analytical study. Results presented in Chapters 4 and 5 are summarized and critically analyzed.

Chapter 7 concludes the thesis and discusses some shortcomings of the experimental and analytical program. Suggestions for future work are also included in this chapter.

Chapter 2 - Literature Review

2.1   General

This chapter summarizes information from literature on the main themes related to this study. First, wood properties important to understanding the development of models and interpretation of experimental results are introduced in Section 2.2, and design considerations for traditional dowel-type timber connections are discussed in Section 2.3. Then, the design of traditional timber SFRSs is briefly explained in Section 2.4 to help readers understand how timber buildings can be designed to dissipate seismic energy; this section helps further highlight the importance of dowel-type connections. The concept of seismic resilience is then introduced; a literature review of resilient design methodologies and structural systems is presented. Finally, SMAs are introduced as a means of achieving resilience in structural systems, and a review of previous uses of SMAs in structural systems is provided.

2.2   Wood as a Construction Material

Wood is a complex material that is subject to many important considerations during design. For instance, wood is a viscoelastic material, which means its properties are affected by the rate and duration of loading, and wood is hygroscopic, which implies that it can absorb moisture from the air (O'Callaghan, 2021). Additionally, wood is an orthotropic material with different mechanical properties in three directions relative to the wood's grain (longitudinal, radial, and tangential to grain). Because the radial and tangential properties are similar, wood is often idealized as transversely isotropic, and the radial and tangential properties are called the "perpendicular" direction (Oliveira, 2021). Wood is strong and ductile in compression (parallel and perpendicular to grain) since fibres densify as they are crushed under compressive loads, however, the behaviour of wood in tension is less favorable (Oliveira, 2021). The tensile capacity of wood is particularly low in the direction perpendicular to grain, and high tensile stresses in this direction can lead to splitting, which is a brittle mode of failure that should be avoided at all costs. While designers can carefully detail wood members not to resist loads primarily through tension in the radial or tangential directions, the presence of knots can cause localized weak spots in wood members. Knots effectively alter the direction of wood grain, meaning a member that is in tension parallel to grain along most of its length, may experience perpendicular to grain tensile stresses where knots interrupt the grain direction.

The wood properties mentioned above introduce some factors engineers must consider when designing wood structures. The viscoelastic nature of wood is considered through a load duration factor in the Canadian design standard (CSA 086), while the possibility for the presence of knots is considered by using a size reduction factor on the resistance of the wood component being designed (Canadian Standards Association [CSA], 2019). The orthotropic nature of wood is simply dealt with by using

different mechanical properties depending on the direction a member is loaded relative to the wood grain. The direction of loading relative to wood grain is particularly important to consider in connections, where brittle failure modes can occur in poorly detailed connections. Considerations for the design of timber connections are discussed in more detail in the next section.

2.3   Timber Dowel-Type Connections

Connections are a critical part of timber buildings as they are relied upon to provide ductility to structures made of members that are otherwise brittle, such as wood columns and beams. This is achieved by ensuring that wood members behave elastically at load levels at which connections experience plastic behaviour. The two primary types of modern timber connections consist of adhesive and mechanical joints (Oudjene & Khelifa, 2010). Mechanical connections are most common and are available in many different forms including split rings and shear plates, proprietary connectors, and dowel-type fasteners (e.g., nails, screws, bolts, etc.). Some proprietary connectors have been developed for use in SFRSs and have shown to be effective at improving the seismic performance of timber buildings. However, dowel-type connections remain the most common connection type for wood-based SFRSs, as they appear in the form of nailed connections in light-frame shear walls, screwed connections in CLT shear walls, and bolted or riveted connections in BTFs.

In designing dowel-type connections in wood, much effort is put into avoiding brittle failure modes to maximize ductility and energy dissipation during seismic events. Brittle failure modes in such connections can be the result of the development of shear or tensile forces parallel-to-grain, leading to row shear or net tension failures, respectively. Alternatively, a combination of shear and tension forces parallel-to-grain can cause failure by group tear-out, and tension perpendicular-to-grain could result in splitting of wood members. Figure 2.1 illustrates the four failure modes described herein.

a) Row Shear b) Group Tear-Out c) Net Tension

d) Splitting Perpendicular-to-Grain
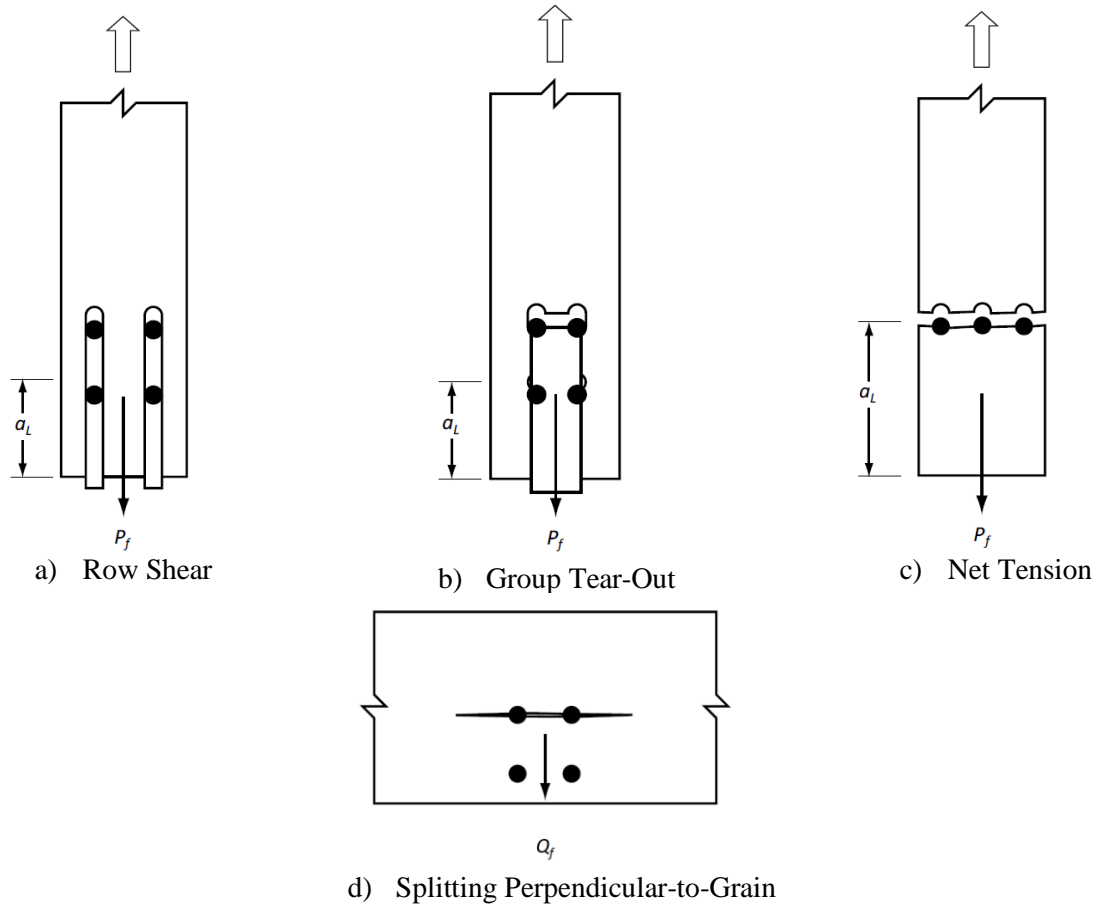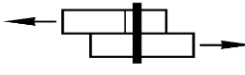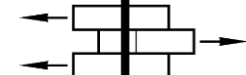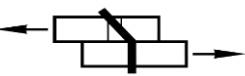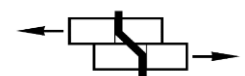
Figure 2.1: Brittle Failure Modes (CSA, 2019)

Splitting perpendicular-to-grain can be avoided by careful detailing of connections to minimize or eliminate forces which cause tension perpendicular-to-grain. Meanwhile, by providing sufficient distance between the end of wood members and the dowels (a_L), it is possible to prevent row shear, group tear-out, and net tension failures. Furthermore, it has been shown that using dowels with a higher slenderness ratio (i.e., small diameter) can help prevent the brittle failure modes shown in Figure 2.1 (Jorissen, 1998). In fact, Jorissen (1998) found that the capacity of rigid (i.e., low slenderness ratio) dowel-type fasteners in wood-wood connections is not accurately predicted by Johansen's Yield Model since these connections fail due to splitting of the wood rather than embedment into the wood member or yielding of fasteners. Johansen's Yield Model, commonly referred to as the European Yield Model (EYM), makes use of equations developed by Johansen (1949) to describe the deformation of dowel-type connections as a product of embedment of dowels into wood, yielding of dowels, or a combination of the two. These are ductile failure modes, since crushing of wood (i.e., embedment) and yielding of steel fasteners do not lead to sudden failure. EYM deformation modes are illustrated in Table 2.1, along with the equations used to calculate the strength for each mode; the lowest strength calculated from all equations governs the design.

7

Table 2.1: European Yield Model Deformation Modes (CSA, 2019)

Mode of Deformation	Two-Member Connections	Three-Member Connections	Design Equation
a)			$f_1 d_f t_1$
b)		n/a	$f_2 d_f t_2$
c)	n/a		$\dfrac{1}{2} f_2 d_f t_2$
d)			$f_1 d_f^2 \left(\sqrt{\dfrac{1}{6}\dfrac{f_2}{(f_1+f_2)}\dfrac{f_y}{f_1}} + \dfrac{1}{5}\dfrac{t_1}{d_f} \right)$
e)		n/a	$f_1 d_f^2 \left(\sqrt{\dfrac{1}{6}\dfrac{f_2}{(f_1+f_2)}\dfrac{f_y}{f_1}} + \dfrac{1}{5}\dfrac{t_2}{d_f} \right)$
f)		n/a	$f_1 d_f^2 \dfrac{1}{5}\left(\dfrac{t_1}{d_f} + \dfrac{f_2}{f_1}\dfrac{t_2}{d_f} \right)$
g)			$f_1 d_f^2 \left(\sqrt{\dfrac{2}{3}\dfrac{f_2}{(f_1+f_2)}\dfrac{f_y}{f_1}} \right)$

In the equations, t_1 and t_2 are the thicknesses of each member, d_f is the fastener diameter, and f_y is the bending yield strength of the fastener. f_1 and f_2 are embedment strengths for the members being connected. For wood members, embedment strength is a function of relative density, fastener bearing area, and loading angle relative to the wood grain (CSA, 2019). In Table 2.1, modes a) to c), and f) only experience damage by embedment of dowels into wood. In contrast, modes d), e), and g) show a combination of timber embedment and fastener yielding. It is desirable to design for failure modes which include fastener yielding, since a dependence on wood embedment alone often leads to high stresses in wood members, ultimately leading to brittle failure modes illustrated in Figure 2.1. Thus, slender dowel-type fasteners are often preferred over fewer rigid fasteners. Examples of slender fasteners include nails, timber rivets and small diameter steel bolts which can all be designed following the Engineering design in wood standard (CSA 086) (CSA, 2019) guidelines. Proprietary fasteners in the form of self-drilling screws are another common type of slender dowel-type fastener which have shown improved stiffness and strength compared to traditional steel bolts (Schreyer, 2002). These screws also have the advantage of not requiring pre-drilling, making installation more efficient than most available alternatives.

In short, dowel-type connections using slender dowels are a very popular type of connection in timber SFRSs, where having ductile connections is paramount. These connections appear as critical components in the three most common types of timber SFRSs, as discussed in the upcoming section.

2.4   Wood-based Seismic Force Resisting Systems

Wood-based SFRSs come in a variety of forms; three of the most popular systems include light-frame shear walls, CLT shear walls, and BTFs. These three systems are introduced in this section, and the importance of dowel-type connections in each system is emphasized.

2.4.1   Light-Frame Shear Walls

Light-frame shear walls are among the most common types of wood-based SFRS, as they are used in most low-rise residential and commercial structures (Plesnik et al., 2016). Light-frame walls consist of many closely spaced framing elements on which structural panels (e.g., oriented strand board or plywood) are fastened, typically using common-wire nails. The performance of this system primarily depends on the nailed sheathing-to-stud dowel-type connections (Plesnik et al., 2016). In fact, the wind and seismic loads on light-frame structures are absorbed by the shear walls' sheathing panels, which act in shear and in turn cause bending in the nails, which act like slender dowel-type fasteners. Although ease of construction and material availability make this a popular system, its applications are limited to low-rise structures due to the higher load demands experienced in high-rise construction.

2.4.2   Cross-laminated Timber Shear Walls

CLT is a prefabricated panelized system consisting of three to nine layers of sawn lumber glued in alternating orientations (see Figure 2.2).

a) CLT Configuration   b) CLT Cross-Sections
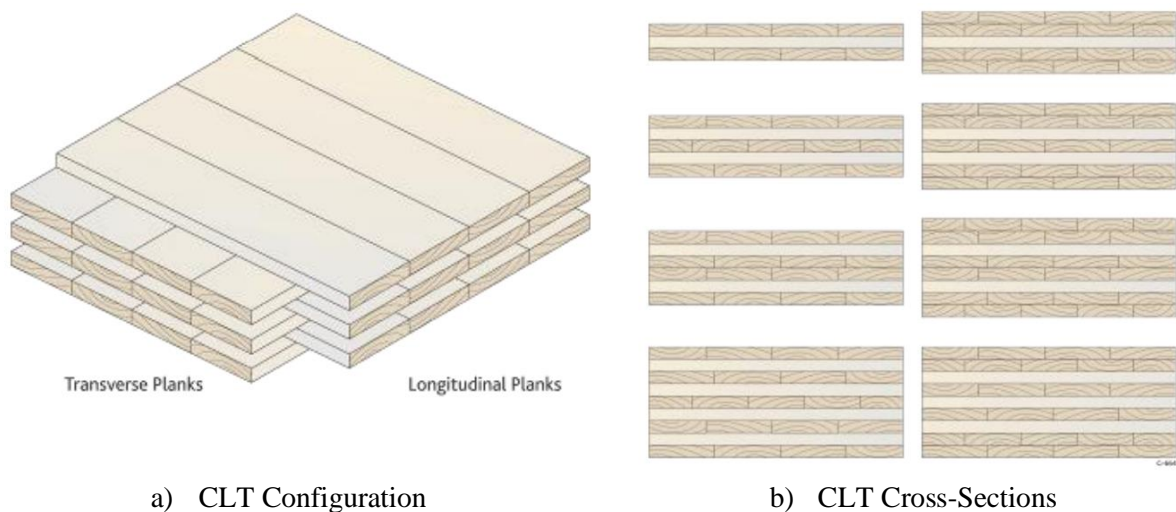
Figure 2.2: CLT Configuration and Cross-Sections (Karacabeyli & Gagnon, 2019)

When used in shear walls, these panels are designed to remain elastic, allowing them to rock in a rigid manner while connections are relied upon to dissipate energy. The energy-dissipative connections are traditionally found at the interface of the CLT shear walls and the supporting floor diaphragm, and between shear wall panels adjacent to each other (Canadian Wood Council [CWC] & CSA, 2017). The connections between shear walls and the floor diaphragm typically consist of hold-downs in which slender dowel-type fasteners are used to secure the steel hold-down to the CLT wall. Meanwhile, traditional connections between CLT shear wall segments consist of lap or spline joints fastened using slender lag screws or self-drilling screws. Figure 2.3 and Figure 2.4 highlight the locations and detailing of the energy-dissipative connections in CLT shear walls.
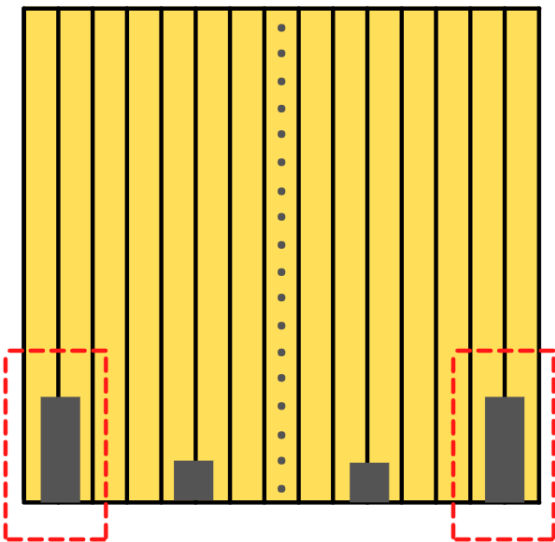
a) CLT Shear wall to Floor Energy-Dissipative (Hold-down) Connection Location

b) Hold-down Connection (Karacabeyli & Gagnon, 2019)

Figure 2.3: Location and Typical Detailing of CLT Panel to Floor Connection
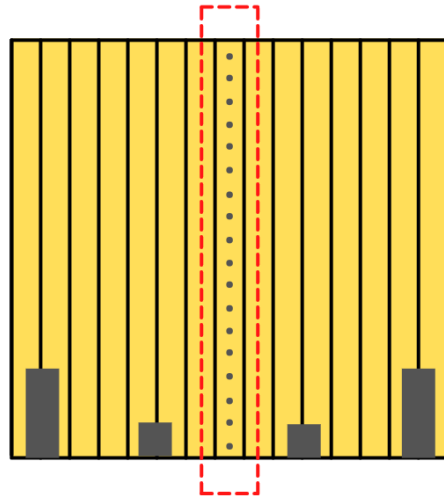
a) CLT Panel-to-Panel Energy-Dissipative Connection Location
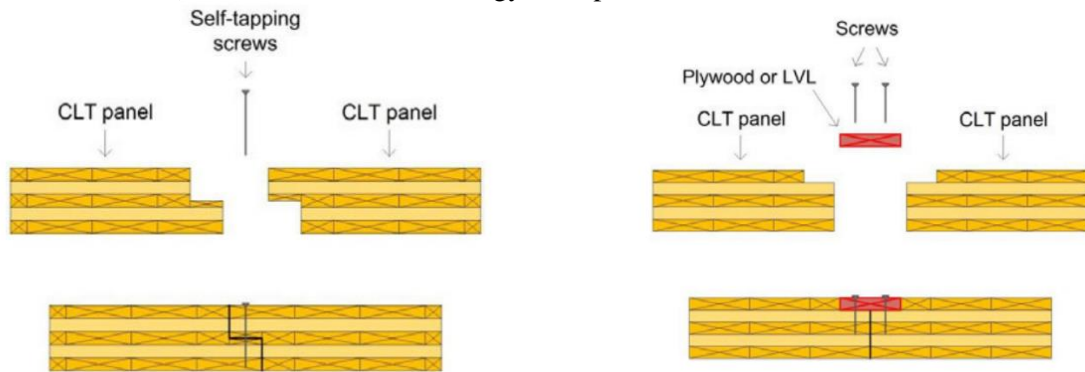
b) Half-Lap Joint (Karacabeyli & Gagnon, 2019)

c) Surface Spline Joint (Karacabeyli & Gagnon, 2019)

Figure 2.4: Location and Typical Detailing of CLT Panel-to-Panel Connections

In designing these connections, one must ensure that a yielding mode of failure governs the design of the dowel-type connections (CWC & CSA, 2017). In other words, deformation modes shown in the EYM (Table 2.1) should govern the connection design rather than the brittle modes shown in Figure 2.1. Additionally, connections need to be able to deform enough to allow the CLT shear walls to move by rocking, sliding, or a combination of both (CWC & CSA, 2017), thus further emphasizing the importance of slender dowel-type fasteners in timber SFRSs.

2.4.3   Braced Timber Frames

BTFs consist of a wood member, usually glulam, parallel strand lumber (PSL), or laminated veneer lumber (LVL), fastened to a wooden frame using dowel-type connectors through the wooden brace and steel plates. For improved fire protection, internal steel knife plates are often used, in which one or many steel plates are inserted into pre-cut openings in the wood brace. Alternatively, two steel plates on either side of the brace can be used to create a steel-wood-steel connection. In either case, slender dowel-type

fasteners are traditionally used to ensure ductile failure modes govern the design of the connections. BTFs differ from the previous two SFRSs introduced (i.e., light-frame and CLT shear walls) in that they are the only non-panel-based system; this gives them the advantage of allowing sunlight to enter when placed on the perimeter of a building, leading to a more vibrant and open atmosphere. BTFs also use material more efficiently than their panel-based counterpart (i.e., CLT shear walls), as one can easily see that braces use less wood than solid walls.

BTFs are included in the National Building Code of Canada (NBCC) and are categorized as having *limited* or *moderate* ductility levels, with different ductility design factors (R_d) assigned for each rating (Canadian Commission on Building and Fire Codes [CCBFC], & National Research Council of Canada [NRCC], 2015). The ductility levels achieved by BTFs are primarily dependent on the fasteners used in the connections of the brace, and although there have been successful implementations of BTFs in wood buildings (Figure 2.5), the widespread adoption of this efficient system has been slowed by a lack of design guidelines. In fact, timber rivets, slender steel bolts, and self-drilling screws have traditionally been used to achieve the NBCC ductility requirements, but there are no guidelines on how to achieve this in the CSA 086 (CSA, 2019).

a.) University of Massachusetts Olver Design Building (Schreyer, 2017)

b.) University of British Columbia Earth Sciences Building Chevron BTF (Equilibrium Consulting, 2013)

Figure 2.5: Examples of BTFs in Buildings

Recently, the NBCC's Committee on Earthquake Design has signaled that BTFs are at risk of being removed from the NBCC due to the lack of design guidelines in the CSA 086 (Chen & Popovski, 2020). Therefore, research is currently underway to quantify ductility levels for BTF connections using steel

bolts and glulam rivets to enable future inclusion of BTFs in the Canadian standard (Chen and Popovski 2020).

In addition to BTFs that rely on dowel-type connections to dissipate seismic energy, studies have been conducted on different systems in an attempt to enable the widespread use of BTFs in mass timber buildings. In fact, Blomgren et al. (2016) showed that heavy timber buckling restrained braces can provide BTFs with better deformation capabilities and strength when compared to traditional BTFs with dowel-type connections. Furthermore, a hybrid timber-steel system consisting of a friction brace connected to wood by glued-in steel rods has been shown to be capable of achieving drift performance levels exceeding NBCC requirements (Miller et al., 2020). Despite the remarkable performance of such systems, manufacturing and design difficulties have prevented them from gaining industry-wide adoption. As a result, simple connections using glulam rivets and steel dowels through steel plates continue to be the prevalent connection type for BTFs, thereby emphasizing the need for solutions that do not necessitate complicated manufacturing or design methods.

2.5   Seismic Resilience

2.5.1   Background

The previous sections focused on the importance of dowel-type connections in timber SFRSs; however, an important concept of any SFRS is their resilience. This section provides background and introduces the concept of seismic resiliency in the context of the scope of this study: the development of a resilient connection type that can be used and easily implemented in timber SFRSs. Examples of seismically resilient structural systems are also provided, and a section is dedicated to discussing existing resilient timber structural systems.

The importance of having ductile structural systems is recognized in the previous sections when discussing the design of ductile connections to protect brittle members in wood buildings. In this study, ductility refers to the ability of a system to show warning signs before critical failures occur, thereby ensuring life safety when coupled with proper maintenance and monitoring. This implies that in the case of extreme loading events (e.g., earthquakes), a ductile design can be considered effective even if the system loses some or all its functional abilities, so long as no lives are lost. While life safety is important, the loss of functionality of buildings can also be critical during disasters such as earthquakes. For instance, following the 8.8 Magnitude earthquake in Chile in 2010, it was found that of 130 hospitals in the affected region, four became non-habitable, twelve experienced more than 75% reduction in functionality, and in total 62% needed repairs or replacement (Earthquake Engineering Research Institute [EERI], 2010). As a result, one month after the tremor 18% of beds in public hospitals remained out of service (EERI, 2010) at a time where illness and injuries were heightened due to damaged infrastructure

in the surrounding areas. Hence, while structural failures of hospitals may not have directly led to many deaths, thereby achieving the goal of a ductile system, the impact of reduced hospital capacity and functionality should not be undervalued.

Resilient structural systems aim to reduce or prevent the need for maintenance or replacements following extreme loading events. Bruneau et al. (2003) states that the objectives of enhanced seismic resilience are to minimize loss of life, injuries, and other economic losses to lessen any reduction in quality of life due to an earthquake. This can be achieved by improving the seismic performance of infrastructure to enable communities to re-gain pre-disaster levels of functioning as quickly as possible (Bruneau et al., 2003).

To qualify as a resilient system, a structure should have the following traits: reduced failure probability, reduced consequences from failures, and reduced time to recovery (Bruneau & Reinhorn, 2007). This notion is represented graphically in Figure 2.6 and mathematically defined by Equation (2.1).
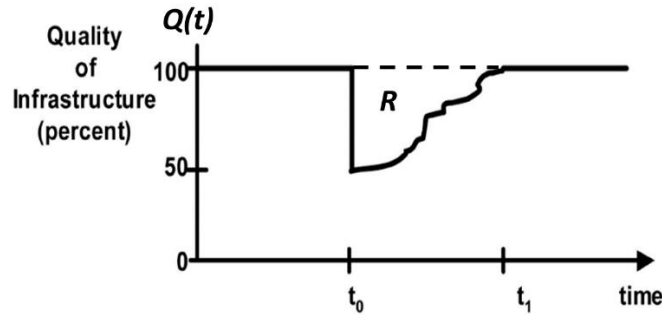
Figure 2.6: Visual Representation of Seismic Resilience (Adapted from Bruneau et al., 2003)

$$R \; = \; \int_{t_0}^{t_1} [100 - Q(t)] dt \tag{2.1}$$

In Equation (2.1) t_0 is the time when a disaster occurs, t_1 is the time when the system is completely repaired and functional, $Q(t)$ is the measure of quality of the infrastructure, and R is the measure of earthquake loss of resilience to the community. Visually, R is the area between the dashed and solid lines in Figure 2.6. Thus, by decreasing the time between t_0 and t_1, or by reducing the drop in $Q(t)$ at t_0, the loss of resilience (R) can be minimized.

In the next section, various strategies used by researchers and designers to improve resilience (i.e., minimize R) in structures are presented. Then, in Section 2.5.3, resilient wood-based SFRSs that have been used in practice or research are presented and discussed.

2.5.2   Seismic Resilience in Structural Engineering

A common approach for designing seismically resilient structural systems consists of using sacrificial "fuses", which are non-critical members that can dissipate energy and easily be replaced. When used effectively, this concept allows for the preservation of critical structural members and rapid replacement of the fuses.

   When designing seismically resilient structures using fuses, the structural fuses must typically be part of the lateral system while still allowing the SFRS to withstand ground motions in a stable manner and the gravity system to remain elastic (Farsangi et al., 2019). Thus, the fuse in the lateral system may be subject to large and irrecoverable damage, but its damaged components should be easily and quickly replaceable to limit the economic impact of earthquake remediation; this effectively decreases the time between t_0 and t_1, thereby decreasing R (see Figure 2.6).

   Vargas and Bruneau (2006) proposed a design and retrofit procedure for a single degree of freedom systems using passive energy dissipation (PED) devices as structural fuses. The three PED devices evaluated in the study consisted of buckling-restrained braces (BRBs), triangular added damping and stiffness (T-ADAS), and shear panels. The proposed design procedure was then expanded to multiple degree of freedom systems, and it was found that the structural fuse concept could still provide adequate system performance (Vargas & Bruneau, 2006). To validate these findings, Vargas and Bruneau (2009) experimentally tested a three-story frame equipped with BRBs acting as metallic structural fuses. The authors deemed that the proposed procedure was reliable enough to be used to design structural fuse systems with adequate seismic performance, and that the procedure can be used to systematically design metallic fuses to protect beams and columns from permanent deformations (Vargas and Bruneau, 2009). Figure 2.7 illustrates the BRBs efficacy in absorbing permanent deformations while ensuring the beams in the gravity system remain elastic.
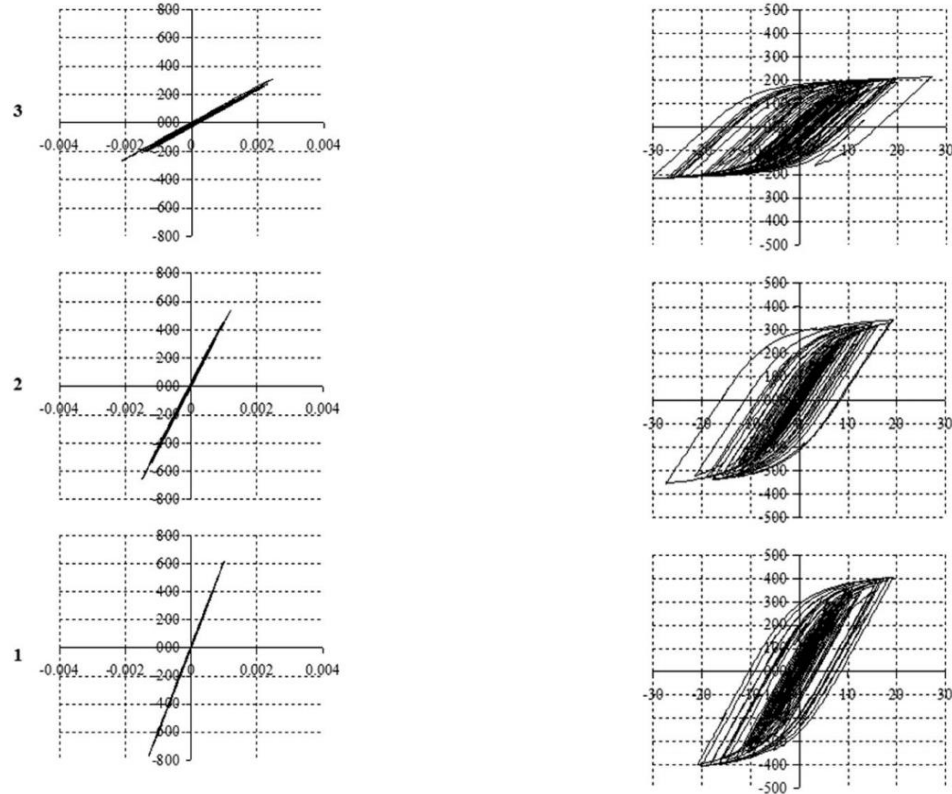
a.) Beam Response (MN-mm vs. rad)   b.) BRBs Response (kN vs mm)

Figure 2.7: Beam (elastic) and BRB (inelastic) Response at Each Story (Vargas & Bruneau, 2009)

A different application of the metallic structural fuse was developed and analytically tested by Nikoukalam and Dolatshahi (2015) in the form of a shear fuse for steel moment resisting frames (MRFs). The traditional approach to designing ductile MRFs consists of placing strategically reduced beam sections near the connections to allow for plastic hinges to form in the beams during extreme loading events. Plastic hinges in the ductile beams prevent failure in the brittle beam-column connections, thereby ensuring ductile behaviour. The behaviour of this conventional ductile MRF design when subjected to a major earthquake is compared to that of an equivalent MRF equipped with a shear fuse in Figure 2.8. Results showed that the shear fuse, which can easily be replaced, successfully absorbed all accumulative damages when equipped on a MRF subjected to a simulated major earthquake. (Nikoukalam & Dolatshahi, 2015).
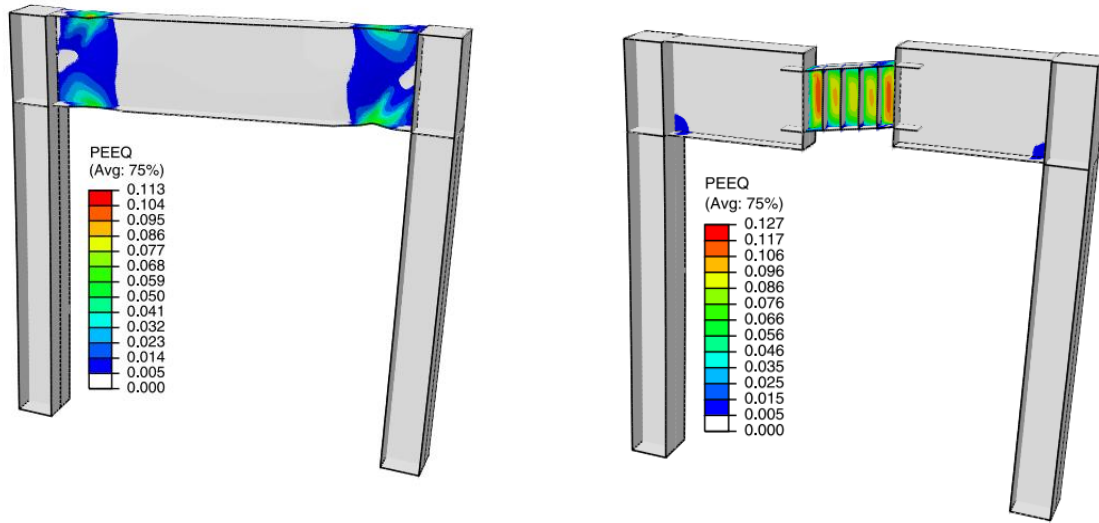
a.) MRF With Reduced Beam Section   b.) MRF With Shear Fuse

Figure 2.8: Comparison of Conventional MRF vs MRF With Shear Fuse (Nikoukalam & Dolatshahi, 2015)

The examples of shear fuses provided above do not constitute an exhaustive list, but the examples help illustrate the goal of using such fuses: making post-disaster repairs and replacements less time consuming and expensive.

While structural fuses limit the time required for a building to re-gain serviceability, some recently developed alternatives seek to eliminate the need for post-earthquake restorations altogether. These systems are commonly referred to as "self-centering", since residual displacements are reduced to an acceptable threshold such that replacement of the structural components is not required. Such self-centering systems aim to achieve what is commonly referred to as "flag-shaped" hysteretic behaviour. This implies a force-displacement relationship which passes through the origin upon reverse loading or unloading, as shown in Figure 2.9.
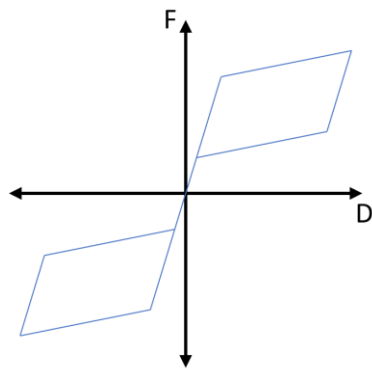
Figure 2.9: Typical Flag-Shaped Hysteretic Behaviour

17

In the past, self-centering systems have primarily been achieved in two ways: shape memory alloys (SMAs), and self-centering mechanisms. The main difference between these two methods is the following: the use of SMAs allows for a self-centering behaviour that is inherent to the material properties, while self-centering mechanisms are achieved through the creative design of structural elements. The two strategies are discussed in more detail below.

First, austenitic (superelastic) SMAs can be used to give a SFRS a flag-shaped hysteretic response because, as was previously stated, the material itself has a self-centering ability (see Figure 2.10).
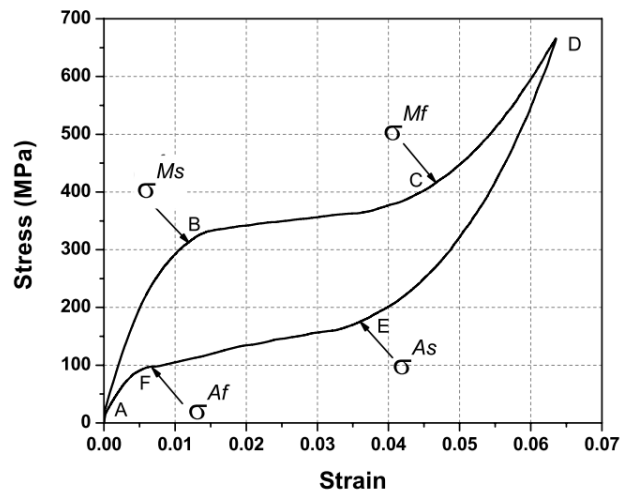
Figure 2.10: Flag-Shaped Response of Superelastic SMAs (Lagoudas, 2008)

Meanwhile, martensitic SMAs can also give structures a self-centering effect because, although they don't exhibit a flag-shaped response, they can re-gain their shape after being heated. Sections 2.6.1 and 2.6.2 are dedicated to explaining the behaviour of these alloys in more detail, while section 2.6.3 provides many examples of their use in structures. Thus, the upcoming paragraphs shift the focus towards literature on the second type of self-centering structural system: those which use mechanisms.

A common way to introduce a self-centering mechanism to a SFRS involves the use of post- or pre-tensioning. The tensioning process pre-compresses two surfaces together (e.g., a column and beam in a moment frame) such that when the system is loaded and a gap develops between the two surfaces, the tensioned components pull the surfaces back together. This effectively closes the gap that had formed between the surfaces, leading to the desired self-centering effect (Chancellor et al., 2014). While pre-stressed tendons give a structure the ability to self-center, the use of these tendons alone seldom provides adequate energy dissipation for seismic design. They must therefore be used in conjunction with an energy dissipative device that is usually one of the following: a yielding elastic-plastic component, a

friction damper, or a viscous damper. The resulting flag-shaped response for the three different dissipaters is shown in Figure 2.11.
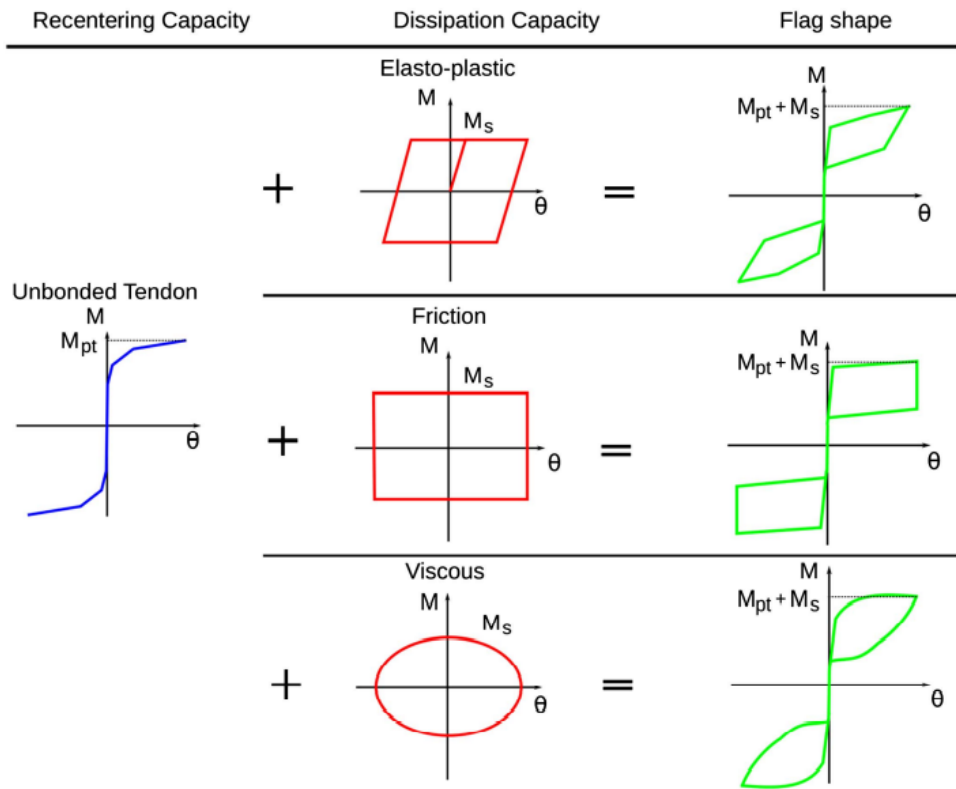
Figure 2.11: Response for Post-Tensioned Systems with Different Damping Types (Granello et al., 2020)

Kim and Christopoulos (2008) proposed a seismic design procedure for a post-tensioned self-centering steel moment frame, which enables the gap opening behaviour at the interface between beams and columns. They then used this design procedure to incorporate the self-centering frames in a six-story building. Time-history analyses showed that the building had almost zero residual drift, while maintaining maximum interstory drifts and floor accelerations similar to what was observed in traditional steel welded moment-resisting frames (Kim & Christopoulos, 2008). Pre-tensioning was also used to develop a self-centering energy-dissipative (SCED) bracing system by Christopoulos et al. (2008). The use of pre-tensioned tendons coupled with a friction-dissipative device led to stable and repeatable self-centering behaviour that demonstrated a flag-shaped response in the full-scale steel braced frame that was experimentally tested (Christopoulos et al., 2008). Multi-story SCED braced frames were later tested in a shake table, and it was confirmed that the system prevented residual drifts of the frame (Erochko et al., 2013). The SCED system developed and tested in these studies is shown in Figure 2.12.
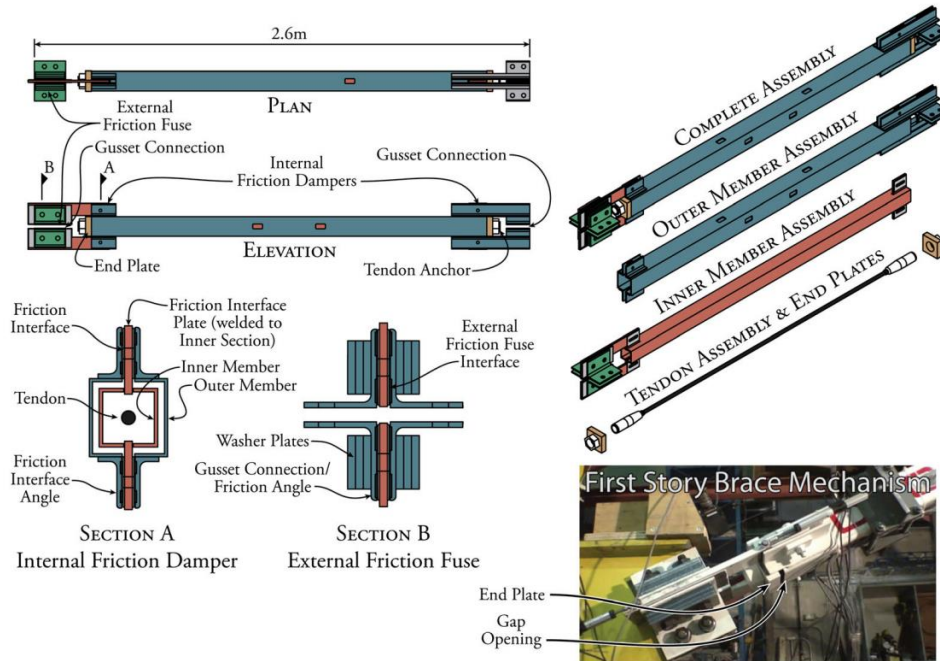
Figure 2.12: SCED System Schematic (Erochko et al., 2013)

Another recently developed method that can be used to introduce self-centering to SFRSs consists of Resilient Slip Friction Joints (RSFJ) (Figure 2.13).
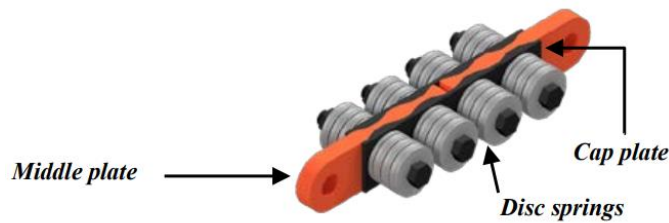
Figure 2.13: RSFJ Schematic (Hashemi et al., 2019)

These resilient connectors have successfully been used to give shear walls (Hashemi et al., 2017a; Hashemi et al., 2017b), braced frames (Yousef-Beik et al., 2019), and moment frames (Hashemi et al., 2018) a flag-shaped hysteretic response. This innovative system also has the advantage of being compatible with steel, concrete, and timber construction since the connector can easily be fastened to any material. Applications of the RSFJ in timber systems will be discussed further in section 2.5.3, and successful implementations of these joints in steel and concrete SFRSs are shown in Figure 2.14.

| a) Concrete Shear Walls (Darani et al., 2018) | b) Steel Moment Frames (Hashemi et al., 2018) |
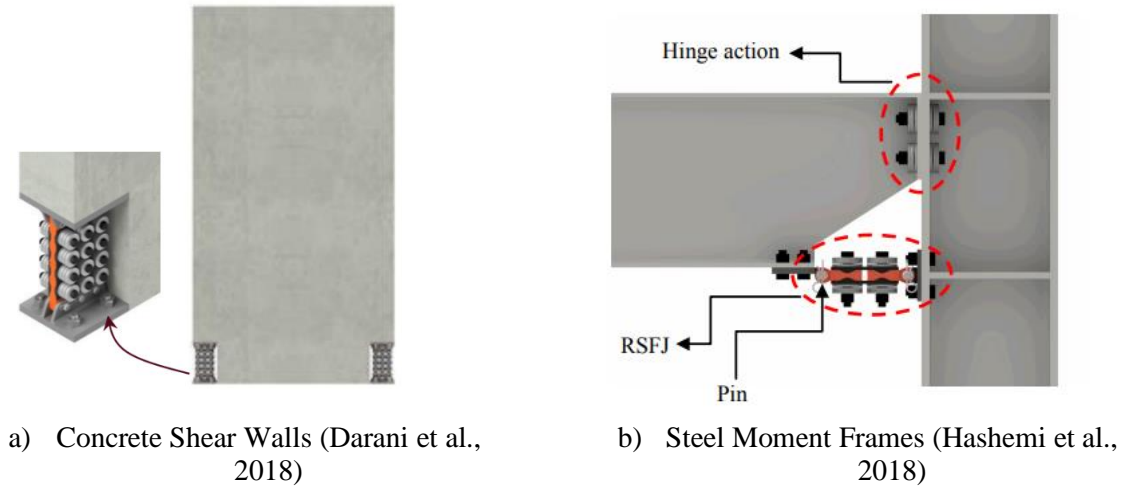
Figure 2.14: Examples of RSFJ Applications in Concrete and Steel SFRSs

The use of post- and pre-tensioning, and RSFJs make up the most widespread implementations of self-centering SFRSs for timber structures. The important innovations in resilient timber based SFRSs are discussed in the next section.

2.5.3   Resilient Timber SFRSs

Various systems have been developed recently to incorporate resilience in timber-based SFRSs, and the most prevalent resilient timber SFRSs use the technologies introduced in section 2.5.2. The first approach being discussed consists of a post-tensioned system commonly known as "Pres-Lam", originally developed by Palermo et al. (2005). In its original form (Figure 2.15), the innovation makes use of an unbonded post-tensioned tendon in LVL beams to provide self-centering to timber frames. Meanwhile, internal elastic-plastic dissipation devices were added to the beam-column connections to provide the LVL frame system with the required damping (Palermo et al., 2005).
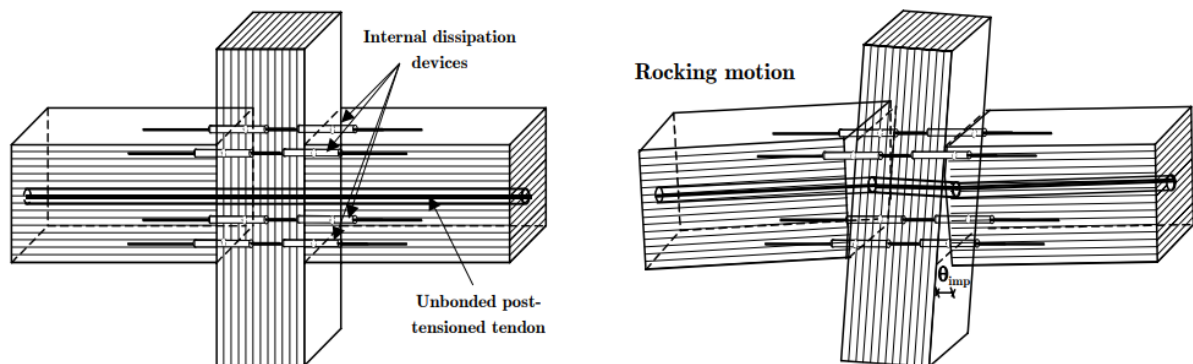
Figure 2.15: Self-Centering System for LVL Frames (Palermo et al., 2005)

Since the conception of the original Pres-Lam system, many different forms of post-stressed timber systems have been developed and tested. In fact, the Pres-Lam system has not only been used at beam-column joints, but also in column-foundation and wall-foundation joints (Granello et al., 2020). In Granello et al. (2020), various studies are highlighted as the state-of-the-art for the behaviour of wall subassemblies, frame subassemblies, and full building specimens using the Pres-Lam systems.

Regarding wall subassemblies, studies have been conducted on LVL (Sarti et al., 2015) and CLT (Ho et al., 2016) walls with elastoplastic energy dissipaters, while other studies employed the use of U-shaped flexural plates (UFP) at the rocking interface to dissipate energy (Iqbal et al., 2015; Ganey et al., 2017). Iqbal et al. (2017) also tested coupled shear walls connected by plywood panels with common wire nails; the system effectively dissipated energy through yielding of the nails and can serve as a cheaper, albeit less efficient alternative to the UFP dissipaters.

The second common use of the Pres-Lam system is in frame assemblies. This application was first tested in the form of a beam-column joint in the original study on the post-tensioned system (Figure 2.15) (Palermo et al., 2005). A later study showed that these beam-column joints could also be used effectively in glulam members, this time using a necked elastic-plastic steel plate to dissipate energy (Smith et al., 2014). A later study compared post-tensioned glulam beam-column connections to traditional bolted moment connections and found that residual deformations were significantly reduced in the novel system, however, the self-centering abilities were less pronounced when elastoplastic energy dissipative devices such as steel angles and caps were added to the assembly (Li et al., 2018).

Recently, the Pres-Lam system has been tested on scaled building and frame assemblies. Newcombe et al. (2010) first tested a 2/3 scale two-story LVL post-tensioned timber frame and wall building. Experimental results showed full re-centering and insignificant damage up to 2% lateral drifts (Newcombe et al., 2010). A full-scale two-story mass timber building equipped with post-tensioned CLT rocking walls and UFP dampers was then subjected to shake table tests (Pei et al., 2019). It was found that the system required no repair for design-basis earthquakes (DBE) (10% probability of exceedance in 50 years), and only minor repairs after maximum considered earthquake (MCE) (2% probability of exceedance in 50 years) level motions (Pei et al., 2019). Finally, Di Cesare et al. (2020) tested a 2/3 scale three-story building with post-tensioned timber frames and energy dissipative braces with UFP dampers. The global response of the system showed the desired flag-shape response and complete re-centering capability (Di Cesare et al., 2020).

Since 2010, the Pres-Lam system has been successfully implemented in buildings around the world to improve the resilience of timber SFRSs (Granello et al., 2020), but some downfalls have prevented the system from gaining widespread adoption. One such factor is that the design of this system lies outside of

the circle of competence of many designers, as the incorporation of post-tensioning in timber systems is not well documented in design guides. Furthermore, while the system allows for a global flag-shaped hysteretic response, it must still be coupled with an energy-dissipative fuse, whether in the form of UFPs, steel coupling beams, or mild steel dissipative devices to provide SFRSs with adequate damping capabilities.

The RSFJs introduced in the previous section successfully address one of the issues with the Pres-Lam system: it relies on friction rather than a sacrificial fuse to dissipate energy. These joints are versatile as they can be applied as shear wall hold-downs, connectors in tension-only or tension-compression braces, and in moment resisting frames (Hashemi et al., 2019). Their behavior is also independent of the building material (i.e., concrete, steel, or timber), since the main structural members are meant to remain elastic, while the inelastic demand is absorbed by the RSFJ (Hashemi et al., 2019).

One of the applications of RSFJs in timber buildings is their use as hold-down connectors for CLT shear walls. Hashemi et al. (2017a) performed experimental tests on a rocking CLT shear wall with RSFJ hold-downs and found that the system avoided permanent damage to the CLT and RSFJ, and the system displayed the desired flag-shaped hysteretic response. Yousef-Beik et al. (2019) then tested the RSFJ in a BTF connection and developed analytical models to simulate a four-story frame subjected to ground motions. Zero residual drifts were observed for the frame equipped with a RSFJ (Yousef-Beik et al., 2019). While this newly developed technology shows great promise for the development of seismically resilient SFRSs, it also requires special knowledge on the topic since RSFJs are not covered in traditional design guides. Additionally, the connectors are made of bulky steel components which can take away from the architectural appeal of exposed timber in buildings.

A persistent theme between the Pres-Lam and RSFJ systems is that designers cannot rely on traditional design guides to incorporate these systems in buildings. Additionally, their applications in BTFs, which are the focus of this thesis, require bulky steel members in the form of UFPs (Pres-Lam) or RSFJs to achieve self-centering and dissipate energy.

In BTFs, permanent damage is often the result of connection-level deformations in the form of wood crushing and dowel yielding. The wood crushing can be limited by carefully designing slender fasteners to ensure a "mode g" failure occurs as per Johansen's Yield Model (see Table 2.1). Wood crushing is undesirable since the permanent embedment deformations of wood around a dowel reduces the energy-dissipation capabilities of the connection upon reverse loading. In fact, when wood is crushed, it creates a gap in the bolt hole and when the connection is loaded along the same path the resistance from the wood member is no longer present. This phenomenon is commonly known as "pinching" since it leads to a pinched force-displacement relationship of the connection. Chan et al. (2021) developed a pinching-free

connector using a ratcheting mechanism that absorbed crushing-induced slack. While this application shows promise for resilient hold-down connectors in wood buildings, it remains unclear whether it can be applied in BTFs.

SMA bars have recently been tested as dowels in connections between wood members (Huang & Chang, 2017) (Huang et al., 2019). Results showed that the inherent self-healing properties of SMAs could provide traditional wood connections with good self-centering abilities. Besides introducing a new material, the proposed joints do not require any advanced knowledge since the design of dowel-type fasteners is commonly known and covered in design guides. This shows promise for the use of SMAs in conjunction with wood to develop self-centering timber systems that don't include bulky metallic components and can be designed using common structural engineering knowledge.

The upcoming section takes a closer look at SMA properties and various existing applications of the material in structural engineering.

2.6   Shape Memory Alloys

2.6.1   Background

SMAs are alloys with unique thermomechanical properties that allow the material to "remember" its original shape. An important discovery which has enabled the development of SMAs consists of the reverse transformation of martensite, which was justified by research performed on thermoelasticity by Kurdyumov and Khandros (1949). Kurdyumov and Khandros made their discoveries on CuZn and CuAl alloys in the late 1940s, but the reverse transformation of martensite was not exploited for practical use until the discovery of Nickel-Titanium (NiTi) alloys in 1963 (Lagoudas, 2008). Lagoudas (2008) cites Buehler et al. (1963) as the study in which NiTi was first discovered during an investigation of materials useful for heat shielding applications.

Since their inception, NiTi alloys, commonly referred to as Nitinol, have found uses in various disciplines. In fact, due to their corrosion resistance, stable configuration, and excellent biocompatibility, NiTi alloys have been used in numerous biomedical fields such as orthopedics (e.g., NiTi staples that compress disjointed bones), orthodontics (e.g., archwires in braces), and neurosurgery (e.g., NiTi coils and stents) to name a few (Lecce & Concilio, 2015). Nitinol has also found uses in aerospace applications and everyday uses such as eyeglass frames. More recently, Nitinol, and SMAs in general, have started being used in structural engineering applications due to their ability to provide functions such as sensing, energy dissipation, and self-healing to structures (Lecce & Concilio, 2015); examples of such applications are presented in Section 2.6.3.

While Nitinol remains the most common type of SMA due to its superior self-centering characteristics, they can be expensive and have an energy-intensive melting process compared to more recently developed alternatives like Cu- and Fe-based SMAs (Lecce & Concilio, 2015). The development of copper (Cu) and iron (Fe) based- SMAs shows promise for the use of SMAs in construction since cost often plays a critical role in decision-making in the industry.

Section 2.6.2 includes an explanation of the material properties of SMAs. Then, a review of literature evaluating the properties of Nitinol, and Cu- and Fe-based SMA bars is presented. Finally, examples of previous applications of SMAs in structures are provided in Section 2.6.3.

2.6.2 Material Properties and Alloy Alternatives

SMAs exist in two phases: austenite and martensite. In the martensite phase, SMAs exhibit what is known as the shape memory effect (SME). The SME allows martensitic SMAs to be subjected to large deformations that are seemingly permanent, then when heated beyond their austenite finish (A_f) temperature, the SMAs recover their original shape. This behaviour is illustrated in Figure 2.16.
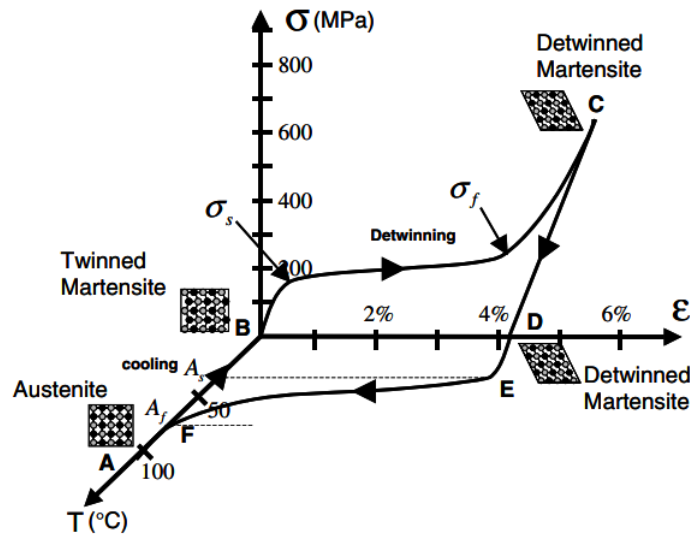
Figure 2.16: Stress-Strain Plot Illustrating the SME (Lagoudas, 2008)

In Figure 2.16, one can see that martensitic SMAs are in a "Twinned Martensite" molecular arrangement before being loaded. Once it starts being stressed, the SMA eventually reaches a stress level (σ_s) where the cellular structure begins to be detwinned. At this stress level, a "yield" plateau begins until a "detwinned finish" stress (σ_f) is reached, and the martensite becomes fully detwinned. Upon unloading, the SMA remains deformed and in a "Detwinned Martensite" phase until it is heated to A_f, at which point deformations are recovered. Upon cooling of the SMA below the "Austenite Start" (A_s) temperature, the SMA returns to its stable "Twinned Martensite" state.

25

In contrast, austenitic SMAs exhibit superelastic (SE) behaviour which allows the alloy to sustain large strains (6-8% strain) but recover its original shape upon unloading. A cycle of the SE effect under uniaxial loading is shown in Figure 2.17.
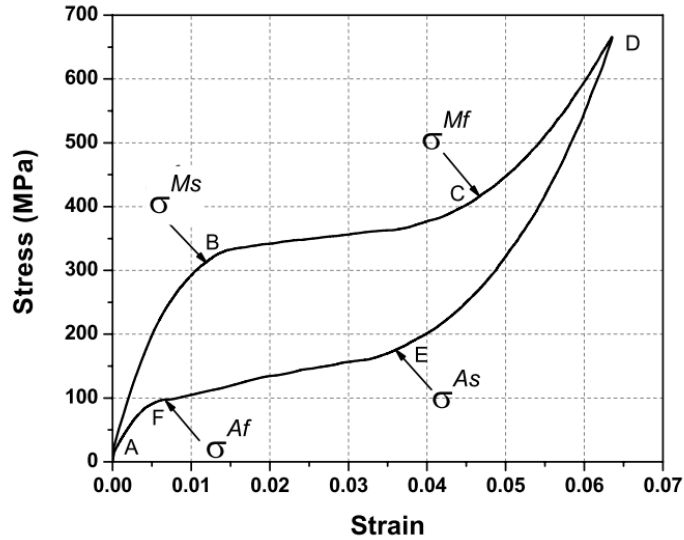
Figure 2.17: Stress-Strain Plot Illustrating the SE Effect of SMAs (Lagoudas, 2008)

It should be noted that for an SMA to display the behaviour shown in Figure 2.17, the alloy needs to be consistently held at a temperature above A_f. When loaded, a stress-induced phase transformation to martensite begins and ends at the martensite start (σ^{Ms}) and finish (σ^{Mf}) stresses, respectively. Upon unloading, the SMA recovers strains as it transforms back to austenite, passing through the austenite start (σ^{As}) and finish (σ^{Af}) stress levels. Figure 2.18 illustrates the SME and SE effects on the same plot, showing the change in behaviour depending on the alloys' transformation temperatures.
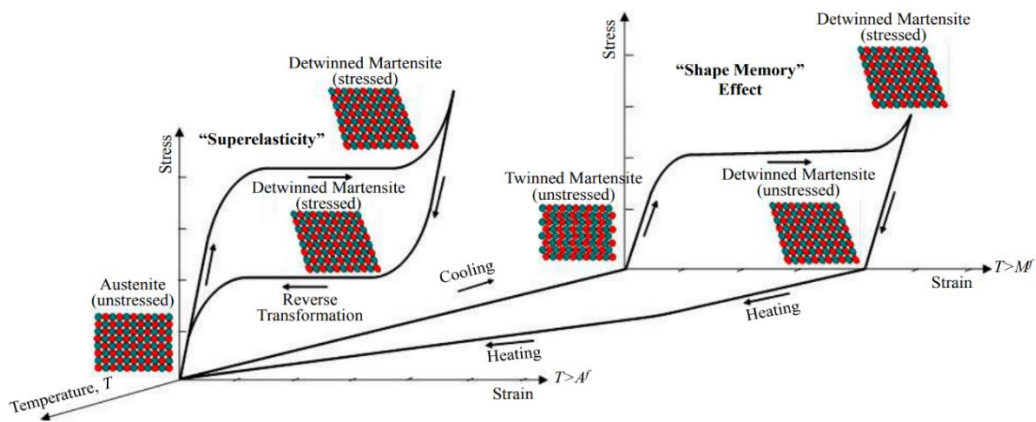
Figure 2.18: SMA Stress-Strain Plots and Phases (Seo et al., 2015)

In this study, the SE effect of SMAs is especially relevant since relying on heat treatment for the desired self-centering effect would be inconvenient. More specifically, SE SMA bars are of particular interest to evaluate their feasibility as self-healing dowels or bolts.

Recent studies have investigated the behaviour of SE SMA bars. In fact, a study by Fang et al. (2015) tested SE NiTi bars in cyclic tension and direct shear to determine the adequacy of such bars in connections. While the Nitinol bars showed good self-centering when subjected to cyclic tension, large diameter NiTi bars showed relatively poor self-centering abilities and energy dissipation under direct shear. However, smaller diameter bars showed improved performance in the direct shear tests, likely due to the inadvertent bending action that happens with slender bars in shear tests (Fang et al., 2015).

Recent studies have looked at the bending behaviour of SE SMA bars. Huang et al. (2019) showed that Cu-based SMA (CuAlMn) bars subjected to cyclic tension showed excellent self-centering abilities and better ductility and low-cycle fatigue relative to steel bars. Another study compared the bending fatigue of Nitinol and a CuAlMn SMAs. It was found that CuAlMn showed higher damping, while NiTi alloys showed greater stiffness in bending (Huang et al., 2020). The same study also credited CuAlMn with having a longer bending fatigue life than the NiTi alloys, though the Cu-based alloys experienced stiffness decay while Nitinol bars did not. Additionally, the Nitinol bars consistently experienced fractures at midspan, which is the location of maximum bending stresses. In contrast, CuAlMn bars were less predictable since fractures occurred along grain boundaries because of this alloys' bamboo-like grain structure (Huang et al., 2020). The Cu-based alloy's grains boundaries also caused the fatigue life of this SMA to be highly dependent on loading frequency, while the fatigue life of Nitinol proved to be independent of this parameter (Huang et al., 2020). In short, CuAlMn and Nitinol bars each have their advantages: CuAlMn has higher damping and a longer fatigue life while Nitinol is stiffer and more predictable when subjected to cyclic bending. Both alloys show largely good damping, stiffness, and fatigue life that is appropriate for civil engineering applications (Huang et al., 2020).

Recently, Fe-based SMAs (e.g., Fe-Mn-Al-Ni) have emerged as cheaper alternatives to NiTi and Cu-based alloys. Vollmer et al. (2019) states low cost of material and a processing route similar to that of the steel industry as two of the reasons why these Fe-based SMAs are a promising affordable option. The high level of workability of Fe-Mn-Al-Ni, and their ability to preserve their SE effect in extreme temperatures offer additional promise for the future use of these inexpensive SMAs (Omori et al., 2011). In fact, Omori et al. (2011) showed that, at low strain levels (1%), the SE effect of an Fe-Mn-Al-Ni SMA had very little change at -50°C, 20°C, and 150°C. One of the main issues with Fe-Mn-Al-Ni is that the recovery of the alloys during the SE effect is not as pronounced as that of Nitinol. However, promising research is being conducted to enable improved SE performance of Fe-based SMAs. Vollmer et al. (2019)

found that adding small amounts of titanium (Fe-Mn-Al-Ni-Ti) or chromium (Fe-Mn-Al-Ni-Cr) promotes abnormal grain growth (AGG) in the Fe-based SMAs. AGG is a process introduced by Omori et al. (2013) to increase the grain size in Cu-based SMAs, thereby reducing grain boundary areas, which improves the SE performance of the material. The development of the inexpensive Fe-based SMAs shows great promise for the future use of SE SMAs in the construction industry. However, since research on the improvement of their SE capabilities are still in early stages, their current applications are limited. The upcoming section discusses existing applications of SMAs in structures.

2.6.3 Applications of Superelastic Shape Memory Alloys in Structures

In practice, SE SMAs have been used numerous times to rehabilitate structures. One such case study is the San Giorgio Church Bell Tower, which was declared unsafe following an earthquake in 1996 (Maurizio et al., 2001). The innovative retrofit consisted of using vertical prestressed steel tie bars at each corner of the tower. All four tie bars were placed in series with a Shape Memory Alloy Device (SMAD) consisting of 60 SE NiTi wires post-tensioned to a force of 20 kN (Maurizio et al., 2001). The 20 kN post-tensioning force was chosen based on numerical analyses performed prior to installation and ensured that the masonry experienced minimal tensile stresses during a seismic event, thereby preventing excessive cracking. The effectiveness of this system was verified following an earthquake in the year 2000 with a similar epicentre and magnitude as the one experienced in 1996; following this event, the Bell Tower was investigated and showed no damage (Maurizio et al., 2001). Another use of SMAs for rehabilitation is in the strengthening of the Basilica of St Francis in Italy following an earthquake in 1997. For this structure, SMADs were used to connect the roof to its tympanum (see Figure 2.19).

Figure 2.19: Cylinders Containing SMADs to Connect the Tympanum to the Roof in the Basilica St Francis (Croci, 2001)

In this application, the phase changes that occur when loading SE SMAs were used to control displacements in the structure for various loading intensities. Croci (2001) explains that under low horizontal action, the SMADs provide great stiffness since the transformation to martensite has yet to begin. Then, under moderate horizontal action the SMADs were designed to allow "controlled displacements" as the SE "yield" plateau occurred due to a transformation from austenite to martensite; this allowed controlled micro cracks to form in the masonry. Finally, under extraordinary horizontal action the SMADs re-gained their stiffness due to the completed transformation to martensite, thereby preventing excessive displacements and instability. This system was verified using shake table tests and showed significantly improved seismic performance relative to using steel bars to tie walls (Croci, 2001). Another innovative use of SE SMAs consists of the strengthening of the Sherith Israel synagogue in San Francisco. Here Nitinol tension ties were used to prevent walls from falling outwards, while also having the ability to re-center the walls in case the outward motion is initiated (Paret et al., 2008).

In recent years, SE SMAs have been researched extensively for use in resilient structural systems. A self-centering BRB (Figure 2.20) was developed and experimentally tested by Miller et al. (2012). The system consists of a steel BRB connected to pre-stressed SE Nitinol rods in a manner that ensures the SMAs are elongated whether the brace is pushed or pulled. Experimental results showed that specimens had a stable hysteretic response, and excellent energy dissipation and self-centering ability (Miller et al., 2012).
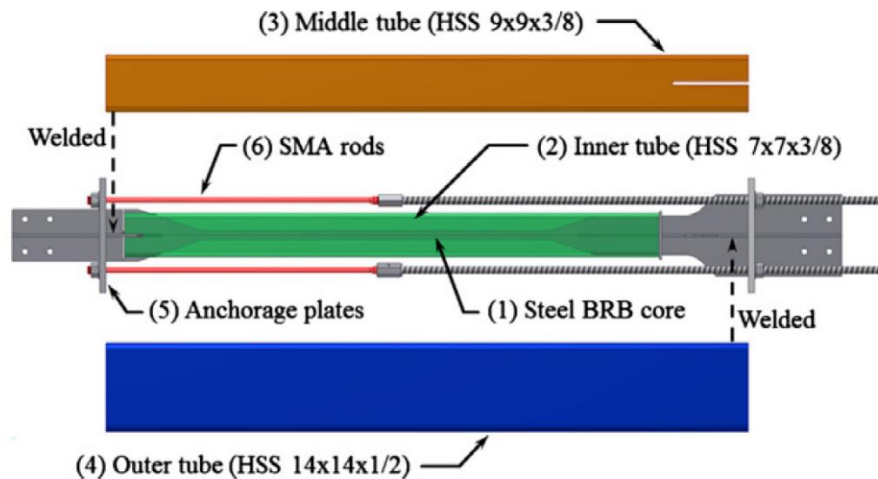
Figure 2.20: Self-Centering BRB Concept (Miller et al., 2012)

Another concept for a steel brace was later developed by Qiu & Zhu (2017), this time using SE NiTi wires (Figure 2.21). The concept was tested numerically and experimentally in a quarter scale 2-storey

braced frame and was able to endure multiple strong simulated earthquakes without severe damage or permanent deformation of the frame (Qiu & Zhu, 2017).
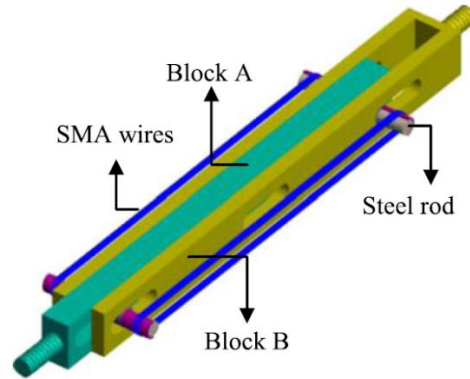
Figure 2.21: Self-Centering Steel Brace Concept with NiTi Wires (Qiu & Zhu, 2017)

Among the first to investigate the use of SE SMAs in connections is Ma et al. (2008) in a beam-column steel connection. In this study, a bolted end-plate connection using all SMA bolts were numerically investigated (Figure 2.22). It was found that deformations could be recovered by the superelastic hinge formed at the beam-column interface, but the authors expressed concerns regarding shear transfer from the beam to the column (Ma et al., 2008).
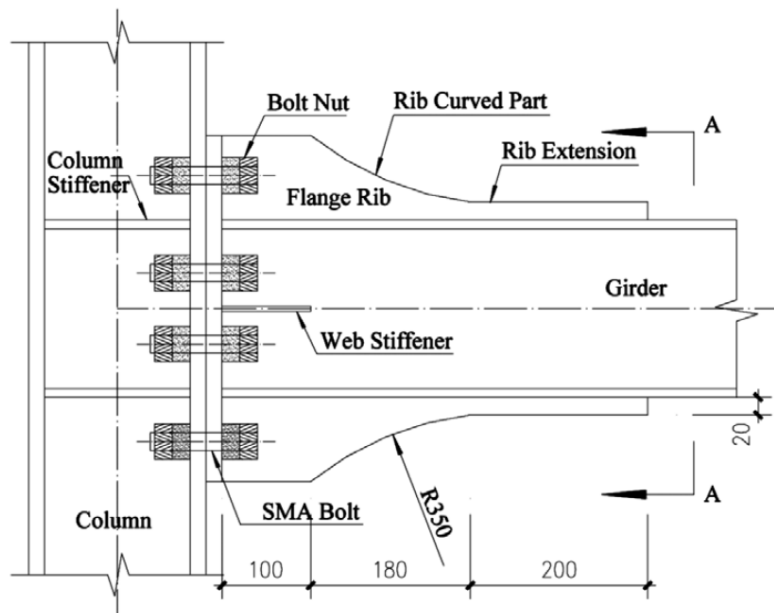
Figure 2.22: Beam-to-Column Connection with SMA Bolts (Ma et al., 2008)

Following tests which confirmed the poor self-centering behaviour of SE SMAs in cyclic direct shear tests, Fang et al. (2015) proposed an improved bolt pattern for the connections which includes a combination of SE SMA and high-strength steel bolts (Figure 2.23), and the system showed improved re-centering capabilities. In the study, Fang et al. (2015) also highlights the presence of undesirable failure modes in the threaded region of SMA bolts during direct tension and shear tests, stating that this should be a consideration in SMA bolt design.
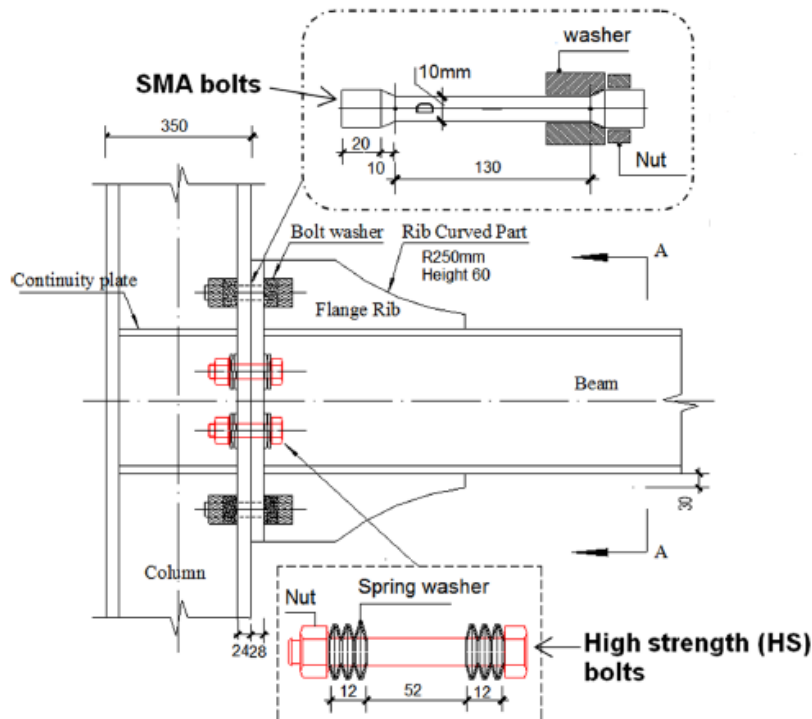
Figure 2.23: Improved Superelastic Beam-to-Column Connection (Fang et al., 2015)

The studies on SMAs in structures mainly focused on the use of unidirectional tensile resistance of the SE members, but some studies have shown that SMAs can also be effective in bending. Wang et al. (2020) used bending SE SMA angles in simulated beam-to-column connections (Figure 2.24 a). Experimental and numerical results showed excellent self-centering abilities and moderate energy dissipation. Wang et al. (2020) also observed degradation of strength during the loading protocol; however, this can be mitigated through the training process of the SMAs. Other examples of successful implementation of SMAs in bending include an innovative bracing system that employs a SE NiTi ring (Figure 2.24 b) and a seismic base isolation system that employs SE SMA U-shaped dampers (Figure 2.24 c).
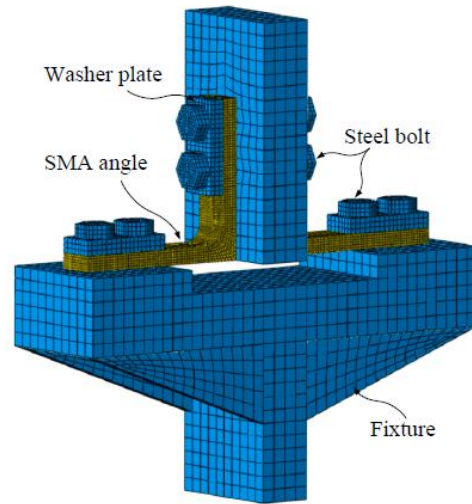
a) Simulated Beam-Column Connection with SMA Angles (Wang et al., 2020)
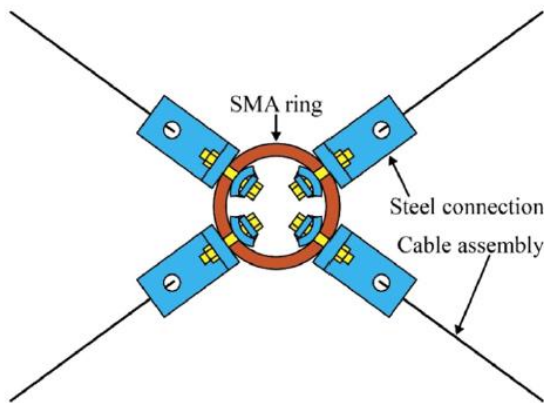
b) Bracing System Connected to SMA Ring (Gao et al., 2016)
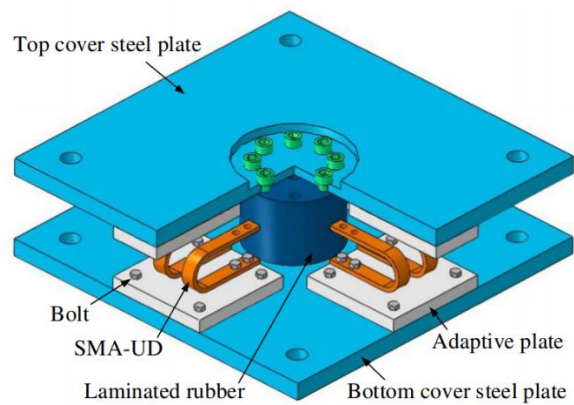
c) Base isolation System with U-Shaped SMA Dampers (Wang et al., 2020)

Figure 2.24: Systems Employing SE SMAs in Bending

Many other studies using SMAs with steel and concrete exist; however, applications of SE SMAs in timber are scarce. A recent study on circular and tubular SMA dowels has shown that SMAs in wood-wood connections demonstrate self-centering abilities while reducing residual deformations at large displacements compared to traditional steel fasteners (Huang & Chang, 2017). Huang et al. (2019) showed that the resistance and self-centering of wood-wood connections with SMA dowels could be further improved by strengthening the wooden region around the dowel with densified veneer wood to limit local wood crushing. Schwarze et al. (2021) compared the damping, stiffness, and residual displacements in double shear wood-to-wood connections using laminated veneer lumber (LVL) with SE NiTi or steel dowels. In the study, the effect of cutting out wood in the anticipated embedded region was

investigated and the use of spring washers to improve the joints' reversibility was also verified. The study corroborated Huang & Chang's (2017) conclusion that SMA dowels offer highly reversible deformation capacity while steel bolts exhibit large plastic deformations. The study found that the re-centering abilities of SMA dowels could be further improved by using cut-outs in wood or spring washers, but that connection detailing should be further improved to prevent the decline in initial stiffness caused by cutting out wood around the bolts (Schwarze et al., 2021). These results are promising for the use of SMAs in conjunction with timber, but wood-wood connections are rare in mass timber buildings as steel gusset plates are often required to fasten members. To the author's knowledge, no tests have been performed on wood-to-steel connections using SMA dowels.

Besides some of the rehabilitation projects mentioned, most applications of SMAs in structural engineering have been limited to research studies like the ones discussed in this chapter. Lecce and Concilio (2015) state manufacturing difficulties of SMAs and high costs as some of the reasons why this is the case, specifically in civil structures which tend to be material intensive. However, as mentioned in Section 2.6.2, the development of Fe- based SMAs in recent years shows promise for SE SMAs that are cheaper and less energy-intensive to manufacture. Additionally, the price of SMAs has been on the decline, going from more than \$1000/kg in the 1990s to around \$100/kg in 2010, a price that is expected to continue to decline as the material becomes more widely used (Alam et al., 2010).

2.7   Summary

This chapter opened with an explanation of the behaviour of timber dowel-type connections. This included an introduction to the EYM, which is used to describe ductile modes of failure in these types of connections. Then, the design of traditional timber SFRSs is explained while highlighting the importance of dowel-type connections when designing wood buildings to resist seismic loads. BTFs are emphasized as a highly efficient wood-based SFRS, and recent studies intended to make their design more attainable to average designers are discussed. These studies focus on the brace connections, as the connections have great influence on the global behaviour of BTFs.

After this, the concept of resilience is introduced and existing technologies for seismically resilient timber structures are discussed. Some of the shortcomings of available systems are assessed; these include a lack of design guidance for systems using proprietary technologies, and the need for bulky steel components. Recent studies using SMAs as dowels in traditional timber connections are then discussed. The use of SMA bars as dowels in wood-wood connections showed good self-centering in multiple studies (Huang & Chang, 2017) (Schwarze et al., 2021). These findings from available literature have motivated this study which seeks to use SMAs as bolts to create resilient timber connections that can be easily designed by practitioners using the widespread EYM.

Many factors were considered when choosing which type of SMA to use for this study. In short, Nitinol bars have been selected due to their availability and well-documented self-centering abilities. However, the continued development of less expensive alternatives such as Fe- and Cu-based alloys are critical to the use of SMAs in structural engineering applications.

In summary, this study seeks to verify the applicability of SMAs as dowels in the wood-steel-wood connections commonly found in BTFs. While other studies have tested SMAs as dowels in wood-wood connections, this has never been done for a connection detail that is typical to BTFs (i.e., wood-steel-wood or steel-wood-steel). Due to the interrelation between connection and system behaviour in BTFs, the successful development of a resilient connection would be a great step forward in the development of a resilient BTF. This research will advance the knowledge on resilient timber connections that can be easily installed and designed using methods that are presently common knowledge in the industry.

Chapter 3 - Experimental Program

3.1 General

An experimental program was developed to investigate the behaviour of steel and SMA dowels in wood-steel-wood connections. The experimental program can be subdivided into four distinct phases investigating:

1. Behaviour of single dowels in bending;

2. Embedment strength of glulam;

3. Connection behaviour of single dowels in wood-steel-wood connections;

4. Performance of a group of bolts in wood-steel-wood connections.

The experimental program involves the testing of 12 wood-steel-wood connections fastened with single dowels (6 SMA, 6 steel) and 12 wood-steel-wood connections fastened using four bolts (6 SMA, 6 steel) under uniaxial monotonic and cyclic loading. In addition to the connection tests, component tests on the steel and SMA dowels as well as on the wood were conducted to determine their respective properties. The following sections describe the conditioning of the wood, test specimens and their components, and the experimental protocols and setups.

3.2 Wood Storage and General Information

Wood is a hygroscopic material with properties that are highly dependent on its moisture content. Therefore, measures must be taken to ensure that moisture fluctuations in the wood being tested are limited for the duration of the experimental program.

The glulam members being used for testing arrived as six 6.1 m long members in August 2021. The wood used was 20F-EX spruce-pine glulam with an industrial finish and a 127 mm × 140 mm (5" × 5.5") cross-section. The members arrived completely wrapped and were stored on a shelf until testing began in early September. As required, the 6.1 m long glulam members were removed from the racks, unwrapped, and cut into the 500 mm long members required for connection tests. When a piece of glulam was unwrapped, it was cut completely into the required lengths (500 mm), and these members were stored in airtight plastic contractor's bags until they were tested. Once a connection test was completed, all wood from the test was put back into the bag, air was removed from the bag as much as possible, and the bag was labelled, sealed, and stored on a shelf. This process ensured that the moisture content and properties of the wood used in connection tests remained mostly unchanged until it was no longer required for embedment tests, and moisture content and density determination by oven-drying.

The remainder of this chapter describes all experimental methods used in this study. The chapter is separated into two sections: the first describes methods for material testing and the determination of material properties, while the second section describes methods used in connection tests.

3.3 Material Testing

This section describes the methods used for the following tests: determination of density and moisture content by oven-drying, dowel bending tests, and embedment tests.

3.3.1 Density and Moisture Content

Following each connection and embedment test, two pieces of wood were cut from the wood specimens to determine the moisture content and density of the wood. To accurately determine the wood properties at the time of the test, oven-drying of the wood specimens was initiated on the same day as tests were conducted. When this was not possible, all pieces of wood were placed in airtight plastic bags to prevent moisture change between time of testing and oven-drying, as specified in Section 3.1.

The density and moisture content of all specimens were determined in accordance with ASTM D4442 (ASTM, 2016) and ASTM D2395 (ASTM, 2017a), respectively. First, the mass of each specimen was recorded using a digital scale, and each face of the prismatic specimen was measured. To account for human error and the imperfect shape of wood specimens, three measurement of each face was recorded, and the average was taken as the final dimension. Then, specimens were put in an oven at approximately 103°C for 24 hours before being weighed. Once the 24-hour weight was recorded, specimens were placed in the oven for an additional three hours to ensure specimens were dry, and that the weight did not change by more than 3 g (0.003 kg) since the 24-hour reading. Once the specimens were dry, the length of each face was recorded using the average of three measurements.

On average, the density of wood tested was measured as 475 kg/m^3, with a COV of 0.04, and the mean relative density (i.e., specific gravity) was determined to be 0.44, with a COV of 0.04. The average moisture content of wood was 14% with a COV of 0.04.

3.3.2 Dowel Bending Tests

Dowel bending tests were performed in accordance with ASTM F1575-17 (ASTM, 2017b) to determine the bending yield moment of SMA and steel bars. A clear span of 73 mm was chosen for the steel and SMA tests, thereby complying with the standard's requirement that the span must be 11.5 times the fastener diameter of 6.35 mm (¼"). The dowel diameters were chosen by first designing a steel connection with behaviour governed by a mode "g" failure in the EYM (see Table 2.1). For the SMA dowels and bolts, an identical diameter was selected in order to allow for a direct comparison to the steel dowels and bolts. At the time of ordering the SMA bars, the bending yield strength of the dowel was

36

unknown both to the author and the manufacturer, as SMA bars are traditionally not used in a bending applications. Loading was displacement-controlled and applied at a rate of 4 mm/min. Figure 3.1 illustrates the test setup used.
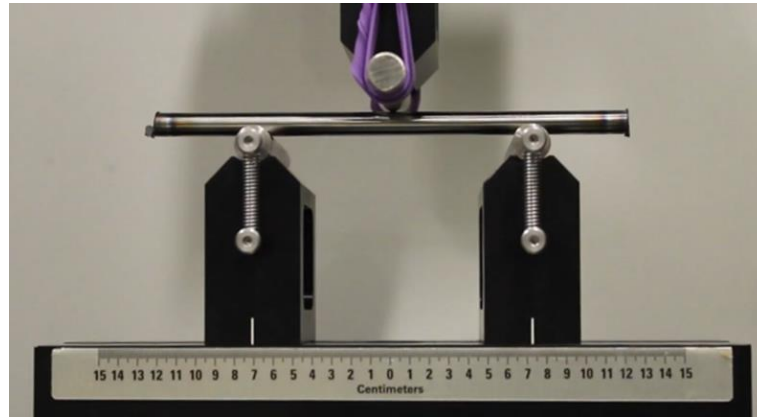
Figure 3.1: Three-Point Bending Test Setup

3.3.3 Glulam Embedment Tests

A total of ten embedment tests were conducted on glulam members in accordance with ASTM D5764 (ASTM, 1997). The ten samples were cut from the middle portion of glulam specimens used in single bar and four bolt connection tests. Half-hole specimens were prepared by drilling a 6.75mm (17/64") Ø hole through the specimen, then cutting off half of the hole using a bandsaw. The holes were oversized by 0.40 mm (1/64"), to ensure the 6.35 mm (¼") Ø bar would fit properly into the half-hole, as permitted in the standard which allows for oversizing of holes by up to 1.59 mm ($^1/_{16}$"). A 150 mm long SMA bar was used to provide the 6.35 mm (¼") Ø bearing. This ensured that a uniform pressure was applied over the length of the specimen as the bar was cut from centerless ground rod, leading to a much straighter product than the steel bolts.

  Each specimen was loaded using 1.5 mm/min displacement-controlled loading, and force and displacement readings were taken at a rate of 20 samples/second. Displacements were measured by a linear variable differential transformer (LVDT). At the start of each test, the LVDT was held in place upside down with its spring compressed by an aluminum angle screwed to the loading head. As the head moved down, the LVDT's spring was allowed to extend and capture the displacement of the head. Figure 3.2 shows pictures of the test setup and the instrumentation used in the embedment tests.

|a.) Test Setup|b.) Instrumentation|
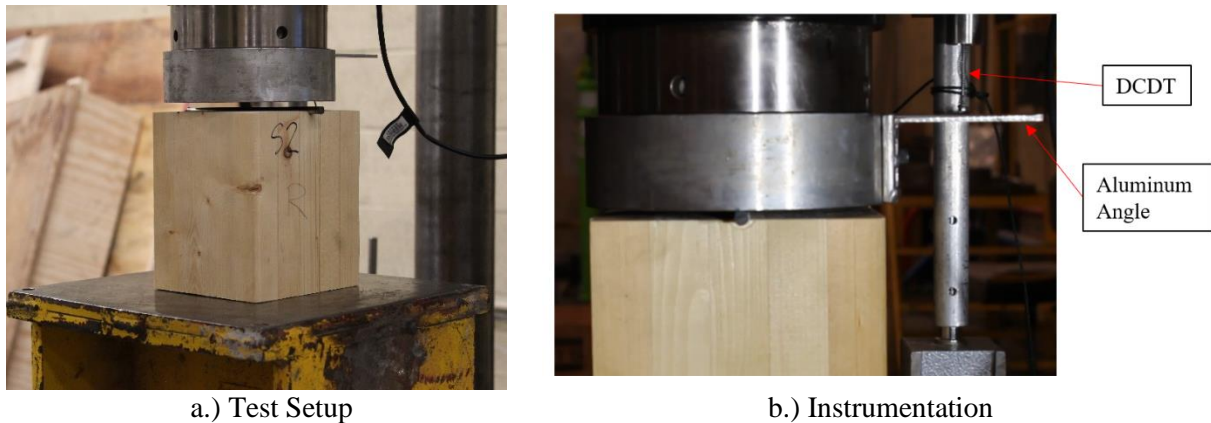
Figure 3.2: Embedment Test Setup and Instrumentation

3.4   Connection Tests

This section summarizes the methods used to test wood-steel-wood connection assemblies. This includes monotonic and cyclic tests on single dowel and four bolt connections. A description of the methods used to prepare wood specimens, steel plates, and dowels is also contained herein. For all connection tests, the nomenclature of specimens is such that the first number represents the number of fasteners (1 or 4), the first letter represents the material ("S" for steel and "N" for the nickel-titanium SMA), the second letter refers to the loading protocol (monotonic (M), or cyclic (C)), and the final number is the specimen number. For instance, 4NM2 is the second connection specimen tested with four SMA bolts in monotonic loading.

3.4.1   Test Setup and Specimen Preparation

Connections tests were performed on an MTS 322 load frame with a capacity of 500 kN. The wood-steel-wood connections being tested were loaded through a 6.35 mm (¼") thick steel plate, which was attached to the frame using a hydraulic grip. The bottom of each specimen was fastened to the frame's table using an overdesigned connection to ensure displacements were focused on the connection of interest. This rigid connection consisted of two 203 mm × 203 mm × 19 mm (8" × 8" × 0.75") hot-rolled steel angles on either side of the glulam specimen fastened to the wood using four 19 mm (¾") Ø ASTM A307 steel bolts. The load readings were taken by the load frame, while displacements were measured using two LVDTs screwed at the top of glulam members. An aluminum angle firmly clamped on the steel plate was used to push and release the LVDT springs as the plate moved up and down; displacement measurements were then taken as the average of the two LVDT readings. The test setup is pictured in Figure 3.3.
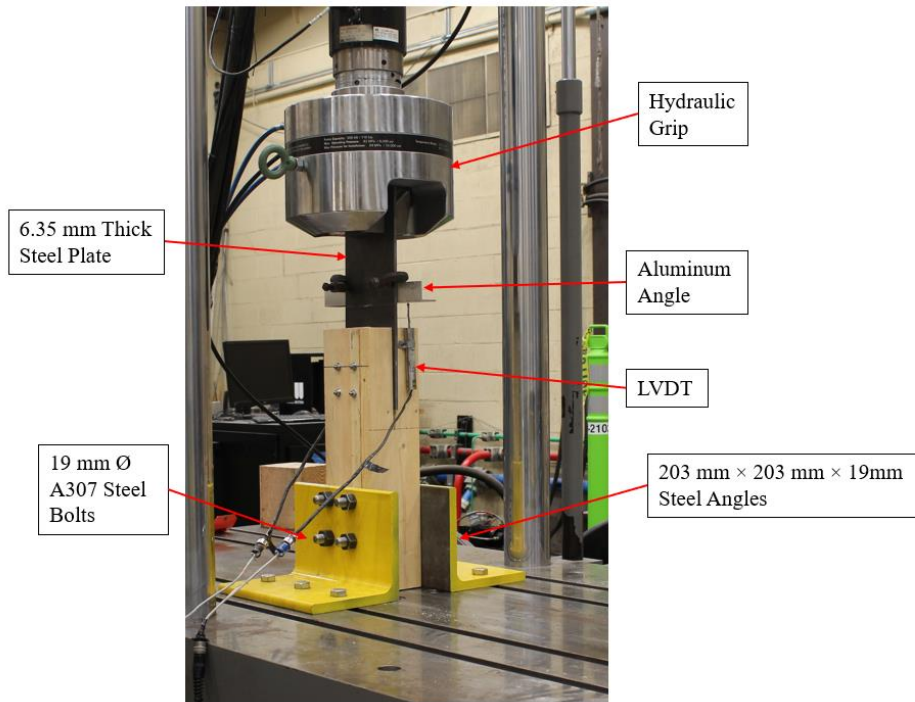
Figure 3.3: Connection Test Setup

The steel plates were 160 mm wide 44W hot-rolled steel plates. The plates were cut to the required lengths using a horizontal bandsaw, and holes were drilled in the plates using a drill press and brad-point drill bits. The drill bits used had diameters of 7.54 mm ($^{19}/_{64}$") for the single dowel tests, and 6.75 mm ($^{17}/_{64}$") for the four bolt connection tests, meaning the holes were oversized by 1.2 mm ($^{3}/_{64}$") and 0.4 mm ($^{1}/_{64}$") respectively. Following each test, the holes in the steel plates were inspected to determine whether they could be reused. In most cases, the steel plates could be reused, as they were specifically designed not to be a governing component of the connections. However, in some cases where displacements were large the plates showed excessive damage and needed to be replaced. Figure 3.4 shows examples of what was deemed an acceptable, or not acceptable level of damage on the plates.

| a) Reusable Plate Damage | b) Non-Reusable Steel Plate Damage |

Figure 3.4: Reusable vs. Non-Reusable Steel Plate

Glulam specimens were cut to 500 mm lengths using a mitre saw, and holes were made using a drill press and spade bits. The four holes at the bottom of the specimen were drilled to a diameter of 20.64 mm ($^{13}/_{16}$"), resulting in a hole 1.6 mm ($^{1}/_{16}$") larger than the 19 mm (¾") bolts used in the overdesigned connection. This tolerance allowed the specimens to be easily aligned while maintaining a tight-fit. Meanwhile, holes in the top part of the specimen were drilled with the same diameter as the steel plates for the single dowel (7.54 mm) and four bolt connection tests (6.75 mm). Finally, the slots in which steel plates were inserted were cut out of glulam specimens in a two-step process. First, a 6.35 mm (¼") diameter hole was drilled through the specimen using the drill press. Then, a bandsaw was used to cut from the top face of the specimen to both sides of the holes, allowing a 6.35 mm (¼") thick slice of wood to be removed from the glulam member. Then, to prevent friction between the steel plate and glulam specimen, a thickness of approximately half of the bandsaw blade was shaved off either side of the slot.

3.4.2   Single Dowel Connection Tests

Single dowel connections were tested using straight steel and SMA bars, thereby allowing for a direct comparison of the material behaviour of steel and nitinol when used as dowels in a wood-steel-wood connection. The steel dowels used in the single dowel tests consist of 152 mm (6") long, 6.35 mm (¼") Ø ASTM A307 steel bolts. The head of each bolt was cut off using a hacksaw to create the steel dowel, and edges were filed by hand to ensure the dowel could slide into the pre-drilled holes in the glulam and steel plate. Meanwhile, to prepare single SMA dowel tests, SMA bars were cut to 150 mm lengths using a chop saw with an abrasive blade, and a belt sander was used to remove sharp edges.

40

Monotonic tests were first conducted with both materials, then a cyclic loading protocol was developed based on the results of these tests using ASTM E2126 (ASTM, 2019) for guidance. The test matrix for single dowel tests is presented in Table 3.1.

Table 3.1: Single Dowel Connection Test Matrix

Steel		SMA	
Monotonic	*Cyclic*	*Monotonic*	*Cyclic*
3	3	3	3

3.4.2.1 Monotonic Single Dowel Tests

For monotonic tests, a loading rate of 4 mm/min was used for both materials, and load and displacement readings were taken at a rate of 10 samples/second. The specimens were loaded until displacements of 45 mm were reached, or until failure occurred. The standard (ASTM E2126) specifies a decrease in load to 80% of the peak force as the "failure" point at which monotonic tests should be stopped to develop the cyclic protocol, however, since the steel tests did not display a clear peak, it was decided that tests would be halted at a displacement of 45 mm, since cracks started to form at this point due to excessive deformations. The "ultimate displacement" needed to develop the cyclic protocol was then varied using the monotonic test results as guidance until meaningful results could be observed. More details on the cyclic loading tests and protocols are provided in the next section.

3.4.2.2 Cyclic Single Dowel Tests

The cyclic loading protocol used in the study was based on Test Method B from ASTM E2126 (ASTM, 2019). However, the standard specifies fractions of the ultimate displacement for each cycle's displacement, and since a "failure" state was not reached in most monotonic tests, this guideline could not be followed. As such, an ultimate (100%) displacement of 12 mm was selected since this displacement level was consistently beyond the linear portion of monotonic force-displacement curves, but still allowed for early cycles to remain within the linear portion. The protocol is presented in Table 3.2.

Table 3.2: Single Dowel Test 12 mm Cyclic Loading Protocol

Step	# of Cycles	Amplitude	Displacement (mm)	Loading Rate (mm/min)
1	1	1.25%	0.15	2
2	1	2.50%	0.30	2
3	1	5.00%	0.60	2
4	1	7.50%	0.90	2
5	1	10.0%	1.20	2
6	3	20.0%	2.40	20
7	3	40.0%	4.80	20
8	3	60.0%	7.20	20
9	3	80.0%	9.60	80
10	3	100%	12.0	80
11	3	120%	14.4	80
12	3	140%	16.8	80
13	3	160%	19.2	80

The sampling rate used for the cyclic test was 50 readings/second. This rate ensured that the minimum of 100 samples/cycle (ASTM, 2019) was reached, even in the shortest cycles.

3.4.3 Four Bolt Connection Tests

For the preparation of four bolt connection tests, the 152 mm (6") long x 6.35 mm (¼") Ø A307 bolts were kept intact (i.e., the bolt head was not cut off). Washers were used on both ends of the bolts and a nut was hand-tightened on the threaded end to complete the connection. Meanwhile, SMA bars were cut to 152 mm (6") lengths, and a 2A Class thread with 28 threads per inch was grinded on both sides of the bars to a length of 12.7 mm (½") on one side, and 15.9 mm ($^5/_8$") on the other. When fastening the SMA bolts onto the specimens, washers were used on both sides and nuts were hand-tightened to fasten the bolts in place.

Again, monotonic tests were first conducted, and the results were used to develop a loading protocol per ASTM E2126 (ASTM, 2019). Methods used to conduct the monotonic and cyclic tests are presented in sections 3.4.3.1 and 3.4.3.2 respectively, and Table 3.3 presents the test matrix for the four bolt connection tests.

Table 3.3: Four Bolt Connection Test Matrix

Steel		SMA	
Monotonic	*Cyclic*	*Monotonic*	*Cyclic*
3	3	3	3

3.4.3.1 Monotonic Four Bolt Tests

The monotonic four bolt connection tests were conducted using a loading rate of 4 mm/minute and a sampling rate of 10 readings/second as for the single dowel tests. Once again, while the standard specifies a failure displacement for the development of a cyclic protocol, tests were usually stopped before a failure could occur. In fact, most tests were stopped before a 20 mm displacement could be reached, as loading beyond this point lead to wood cracking, which is not representative of connections with slender bolts, but is inevitable when forcing high displacements.

3.4.3.2 Cyclic Four Bolt Tests

The cyclic loading protocol used for four bolt tests was, once again, based on Test Method B from ASTM E2126 (ASTM, 2019). Since monotonic tests were stopped before the standard's classification of "failure", the ultimate (100%) displacements were selected based on judgment from the monotonic results. Like in the single dowel cyclic tests, the 12 mm (100% displacement) protocol was used, so Table 3.2 of section 3.4.2.2 can be referenced for the loading protocol used in the four bolt cyclic tests.

Chapter 4 - Experimental Results

4.1   General

The experimental results from the testing described in Chapter 3 are presented in this chapter. The chapter
is separated into three main sections corresponding to the components tests on the wood and dowels,
single dowel wood-steel-wood connection tests, and bolt group connection tests, respectively.

4.2   Component Test Results

4.2.1   Dowel Bending Test Results

A total of five steel and five SMA dowel connections were tested in bending under a concentrated load to
characterize the material behaviour. Figure 4.1 b) and c), and Figure 4.1 b) and d) show representative
results for the steel and SMA dowels, respectively.
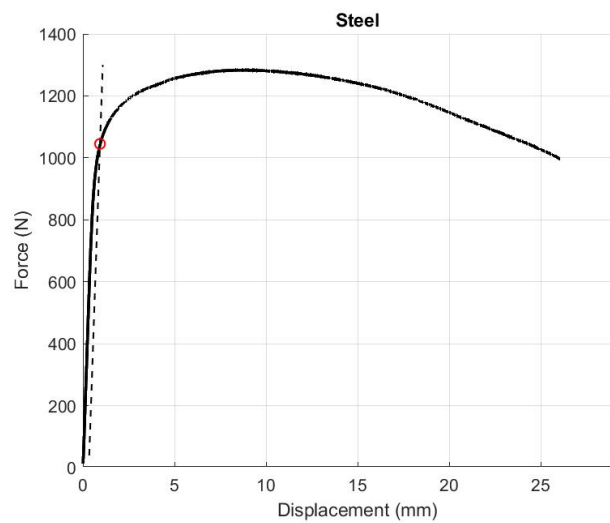
a) Force-Displacement Curve - Steel
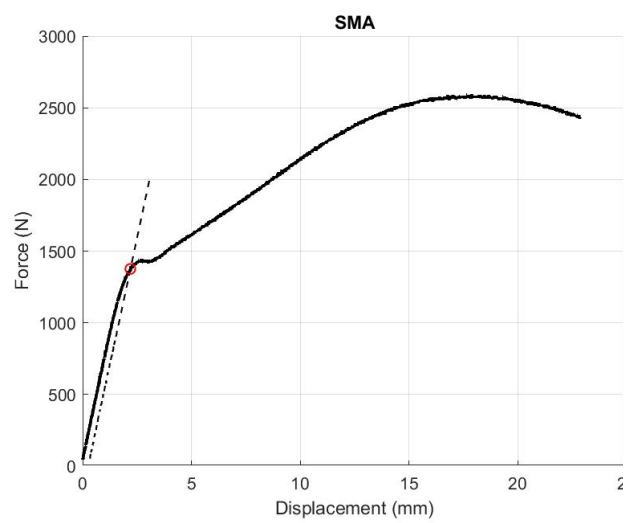
b) Force-Displacement Curve – SMA

c) Damage After Unloading - Steel

d) Damage After Unloading - SMA

Figure 4.1: Representative Bending Test Results – Steel vs SMA

Figure 4.1 shows a representative load-displacement graph for the steel (a) and SMA (b) bending tests. The steel bolts behavior is characterized by an initial linear behaviour followed by yielding and a gradual strength loss, whereas the SMA bar's behaviour demonstrates a yield point followed by a second stiffness until the force peaks around 17 mm of displacement. Figure 4.1c) and d) show typical permanent deformations experienced by both the steel and SMA, respectively. The complete results for all the steel and SMA dowels can be found in Appendix A.

The yield load of the steel and SMA dowels was determined using the 5% offset method, which consists of offsetting the linear portion of the load-displacement curve by 5% of the dowel diameter and taking the intersection of this line with the load-displacement curve as the yield load (ASTM, 2017b). This method is portrayed in Figure 4.1 a) and b). Table 4.1 lists the average bending yield stress obtained for each material along with their respective coefficient of variation (COV). Despite having similar diameters, the effects of the SMA having a higher yield strength compared to the steel on the behaviour of the connections is addressed in Chapter 6.

Table 4.1: Average Experimental Bending Yield Stress for Steel and SMA

Parameter	Steel	SMA
Average Bending Yield Stress (MPa)	439	571
COV	0.03	0.03

One of the main objectives of performing bending tests was to determine whether SMAs in bending could exhibit good self-centering abilities. Figure 4.1d) clearly shows the SMA's ability to recover large displacements; however, semi-cyclic three-point bending tests were also conducted to reinforce this observation. Figure 4.2 shows a representative force-displacement curve for a one-way semi-cyclic bending test on an SMA bar.
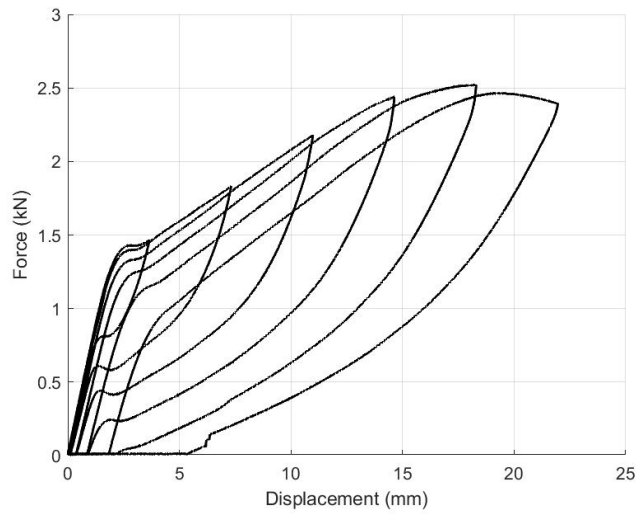
Figure 4.2: Representative Force-Displacement Relationship of SMA Dowel in Semi-Cyclic Bending

4.2.2 Glulam Embedment Test Results

A total of ten embedment tests were conducted on glulam members in accordance with ASTM D5764 (ASTM, 1997). The ten samples were cut from the undamaged middle portion of the glulam specimens used in single dowel connection tests. Figure 4.3a) illustrates the 5% offset method used to determine yield force using the force-displacement plots obtained from the test data, and Figure 4.3b) shows a representative damaged specimen. The average embedment yield stress was calculated as 28.6 MPa with a COV of 0.19. Appendix A can be referenced for a summary of the results obtained from individual tests.
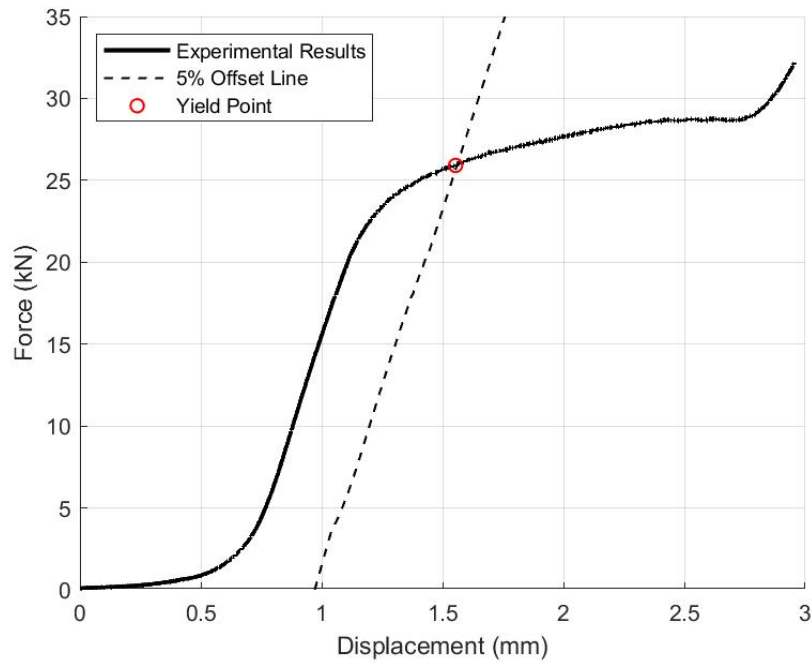
a) Determination of Embedment Strength of Wood

b) Embedment Failure

Figure 4.3: Representative Failure of Glulam Specimens from Embedment Tests

4.3 Single Dowel Connection Test Results

4.3.1 Steel Dowels

A total of three monotonic and three cyclic tests were conducted on single steel dowel wood-steel-wood parallel-to-grain connections.

The force-displacement relationship of all single steel bar tests indicated a ductile mode of failure in which the connection maintains its initial stiffness until the onset of plastic deformations through steel dowel yielding and wood crushing. A representative curve is shown in Figure 4.4.
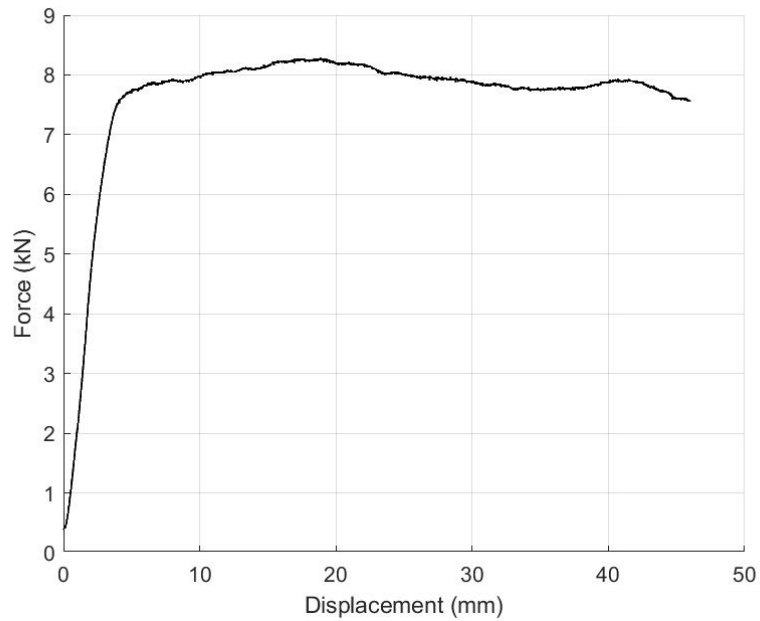
Figure 4.4: Representative Force-Displacement Relationship for Monotonic Steel Dowel Tests

The monotonic tests performed on connections with a single steel bar consistently led to the development of three plastic hinges in the bar; this was designed for using Johansen's yield equations (CSA, 2019). This is made clear by looking at the shape of one of the deformed bars and the resulting wood crushing (Figure 4.5). Appendix B can be referenced for pictures and force-displacement relationships of each specimen tested.

a.) Deformed Bar with 3 Plastic Hinges   b.) Wood Crushing

Figure 4.5: Representative Damage from Single Steel Dowel Monotonic Tests

Table 4.2 presents key parameters obtained from the experimental monotonic tests conducted on the single steel dowel connections.

Table 4.2: Monotonic Steel Dowel Connection Test Results

Test #	P_{max}[a] (kN)	Δ_{max}[b] (mm)	k_i[c] (N/mm)	P_y[d] (kN)	Δ_y[e] (mm)
1SM1	8.3	18.8	2247	7.3	3.7
1SM2	10.1	42.7	9550	5.3	1.1
1SM3	8.8	21.2	3882	5.5	1.6
Average	9.1	27.6	5226	6.0	2.1
COV	0.08	0.39	0.60	0.15	0.54

[a] Maximum load recorded during test.
[b] Displacement at the maximum load.
[c] Initial stiffness taken as the slope of force-displacement plot between 10% and 40% of P_{max}.
[d] Yield load determined using the 5% offset method.
[e] Displacement at yield load.

Three single steel dowel connections were then subjected to the cyclic protocol described in Table 3.2. Figure 4.6 shows a representative force-displacement relationship for the single steel dowel connections when subjected to cyclic loading alongside a representative monotonic test.
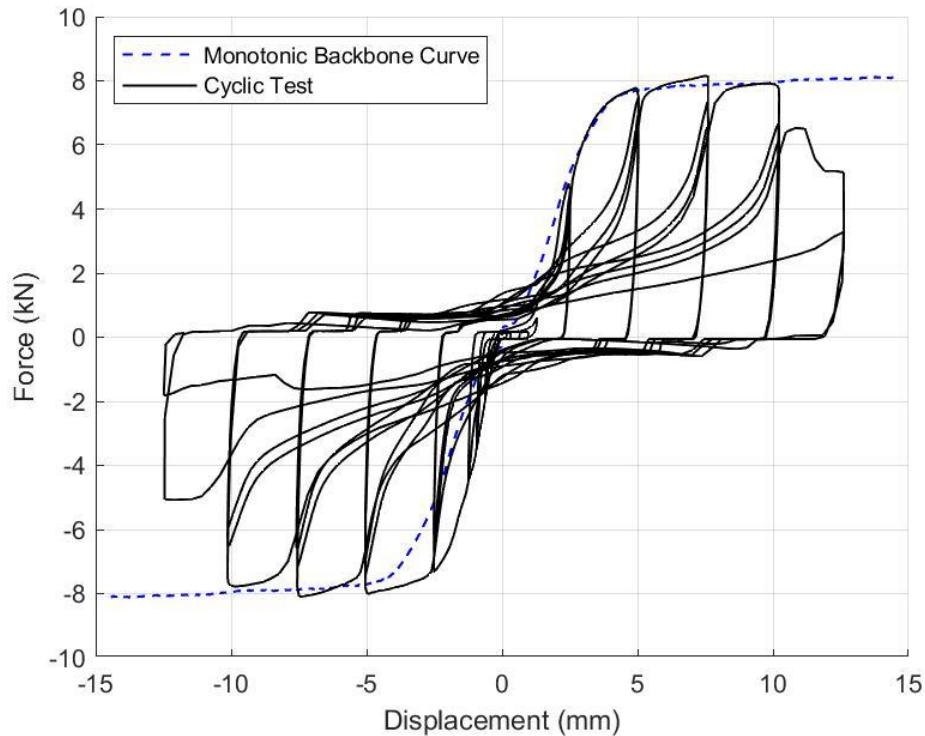
Figure 4.6: Representative Force-Displacement Relationship for Cyclic Steel Dowel Tests

Figure 4.7 shows representative damage and failure modes of the steel dowel connections under cyclic loading. The steel dowels were observed to form the three plastic hinges that are characteristic to a mode "(g)" failure in the EYM, as in the monotonic tests. An eventual failure occurred at the middle plastic hinge. Table 4.3 presents key parameters obtained from the experimental cyclic tests conducted on the single steel dowel connections. Force-displacement curves and pictures of damage to wood and dowels for all three cyclic tests can be found in Appendix B.

a.) Dowel Broken at Middle Plastic Hinge   b.) Wood Crushing from Cyclic Test

Figure 4.7: Typical Damage from Single Steel Dowel Cyclic Tests

Table 4.3: Cyclic Steel Dowel Connection Test Results

Test #	$P_{max\_c}{}^a$ (kN)	$\Delta_{max\_c}{}^b$ (mm)	$P_{max\_t}{}^c$ (kN)	$\Delta_{max\_t}{}^d$ (mm)	k^e (N/mm)
1SC1	8.1	7.6	8.2	7.6	2726
1SC2	8.8	6.7	8.4	7.6	2735
1SC3	8.8	6.7	8.2	7.7	2502
Average	8.6	7.0	8.3	7.6	2654
COV	0.04	0.06	0.01	0.004	0.04

[a] Maximum load reached in compression cycle.
[b] Displacement when lead reached P_{max_c}.
[c] Maximum load reached in tension cycle.
[d] Displacement when load reached P_{max_t}.
[e] Stiffness of connection as slope from 10% to 40% of P_{max_t}.

4.3.2 SMA Dowels

The force-displacement relationship of the SMA dowel tests indicated a less pronounced transition from elastic to plastic behaviour when compared to the steel bar tests. This is likely due to the higher bending yield load of these bars, as calculated from three-point bending tests (Table 2.1). Regardless, the single bar connections were mostly capable of withstanding high deformations without brittle failures except for one test in which the bolt sheared suddenly at a displacement of 35 mm. This could have been the result of an anomaly in the material, as all other tests reached displacements of 45 mm. However, this

observation also highlights potential issues with using nickel-titanium SMAs in regions of high shear stresses. A typical curve is shown in Figure 4.8.
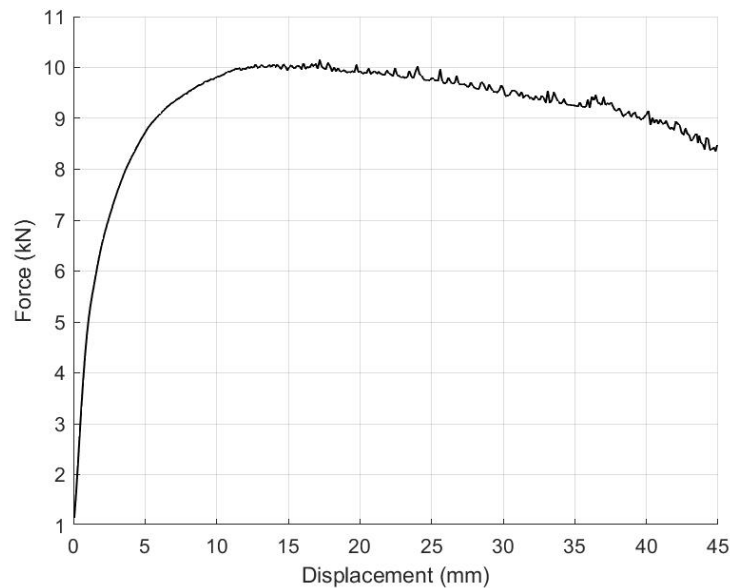
Figure 4.8: Typical Force-Displacement Relationship for Monotonic SMA Dowel Tests

It should be noted that one of the monotonic tests conducted shows a force-displacement relationship with a clear peak, followed by a gradually decreasing force. Upon inspection of the specimen where this was observed, it was found that a knot happened to intersect with the region of wood crushing (see Figure 4.9). The intersection of knots with the deformation plane can lead to the development of cracks. This behaviour should not be considered typical, as the chances of this happening are normally quite low and are accounted for in design equations of timber connections.
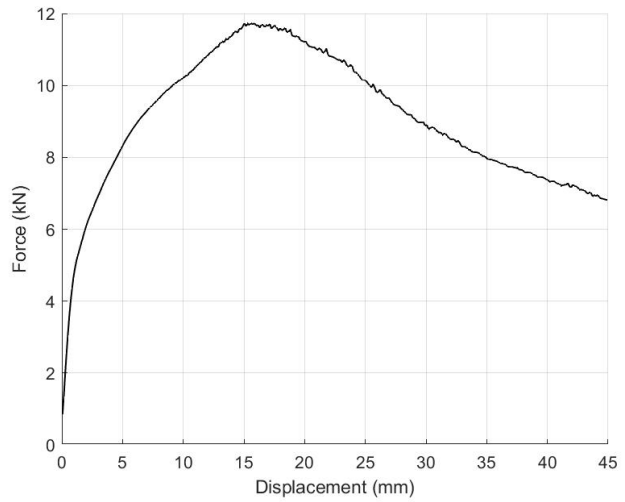
a.) Knot in Wood Crushing Region   b.) Resulting Force-Displacement Relationship

Figure 4.9: SMA Connection with Knot and Resulting Force-Displacement Relationship

Overall, the monotonic tests performed on connections with a single SMA bar yielded a similar deformation mode as what was observed during steel bar tests. In fact, while the picture of the deformed bar in Figure 4.10a) appears to show the development of only one hinge, it is clear by looking at the picture of the wood crushing Figure 4.10b) that three hinges formed indicating that the superelastic SMA was able to recover deformations in the two outermost hinges, while the middle hinge could not be fully recovered at high displacement levels. Table 4.4 summarizes connection parameters calculated from the experimental data.

a.) Deformed Bar with Permanent Hinge   b.) Wood Crushing

Figure 4.10: Typical Damage from Single SMA Dowel Monotonic Tests

Table 4.4: Monotonic SMA Dowel Connection Test Results

Test #	P_{max}[a] (kN)	Δ_{max}[b] (mm)	k_i[c] (N/mm)	P_y[d] (kN)	Δ_y[e] (mm)
1NM1	12.5	23.4	5214	5.8	1.4
1NM2	10.3	17.2	4460	5.7	1.4
1NM3	11.9	15.7	4193	5.3	1.4
Average	11.6	18.8	4622	5.6	1.4
COV	0.08	0.18	0.09	0.04	0.01

[a] Maximum load recorded during the test.
[b] Displacement at the maximum load.
[c] Initial stiffness taken as the slope of force-displacement plot between 10% and 40% of P_{max}.
[d] Yield load determined using the 5% offset method.
[e] Displacement at yield load.

When subjected to cyclic loading, SMA dowel connections maintained their ability to carry the load until a point where the dowel sheared abruptly. Beyond this point, the force did not drop to zero only because one half of the bar was still partially supporting the steel plate as it was displaced. This was able to happen since failure occurred at only one of two steel-wood interfaces, leaving part of bar to partially support the plate until it slipped out of the hole. Figure 4.11 shows a representative force-displacement behaviour of the single SMA dowel connections under cyclic loading to a representative monotonic test.
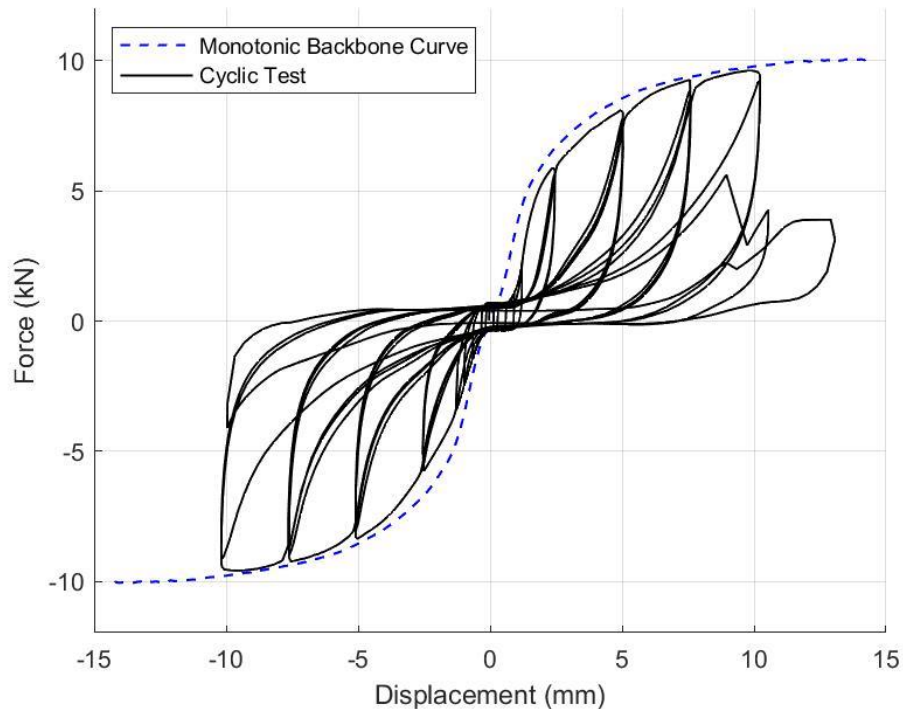
Figure 4.11: Typical Force-Displacement Relationship for Cyclic SMA Bar Tests

When subjected to cyclic loading, the single SMA dowel connections developed three hinges, which is typical of a Mode "g" failure in the CSA 086. While the initial deformations in the form of SMA dowel bending and wood crushing indicate ductile behaviour, the NiTi SMA's tendency to break suddenly at shear planes is not favorable. An example of a broken bar and the damage to wood specimens is shown in Figure 4.12, and Table 4.5 presents the connection parameters calculated from experimental data.

a.) Bar Broken at Middle Plastic Hinge   b.) Wood Crushing from Cyclic Test
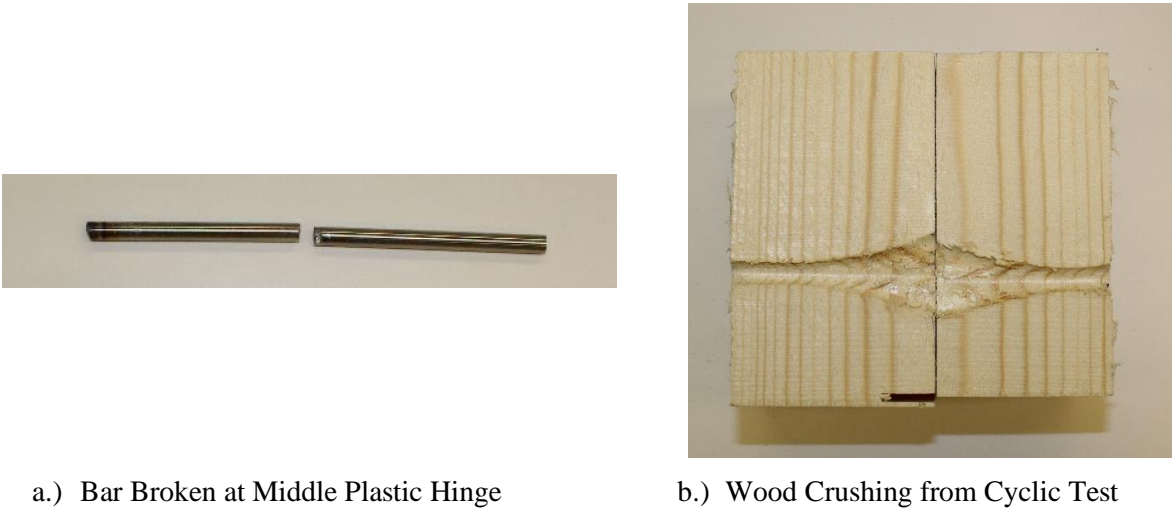
Figure 4.12: Typical Damage from Single SMA Dowel Cyclic Tests

Table 4.5: Cyclic SMA Dowel Connection Test Results

Test #	$P_{max\_c}{}^a$ (kN)	$\Delta_{max\_c}{}^b$ (mm)	$P_{max\_t}{}^c$ (kN)	$\Delta_{max\_t}{}^d$ (mm)	k^e (N/mm)
1NC1	9.8	9.8	9.6	9.9	4461
1NC2	9.6	9.6	9.6	9.8	4608
1NC3	11.0	7.6	10.9	7.6	7844
Average	10.1	9.00	10.0	9.1	5638
COV	0.06	0.11	0.06	0.12	0.28

[a] Maximum load reached in compression cycle.
[b] Displacement when lead reached P_{max_c}.
[c] Maximum load reached in tension cycle.
[d] Displacement when load reached P_{max_t}.
[e] Stiffness of connection as slope from 10% to 40% of P_{max_t}.

Force-displacement curves and pictures of damage to wood and dowels for individual SMA dowel connection tests can be found in Appendix B.

4.4   Bolt Group Connection Tests

4.4.1   Steel Bolts

A total of three monotonic and three cyclic tests were conducted on steel bolted wood-steel-wood connections. The force-displacement relationship of all steel bolted connection tests indicates a ductile mode of failure in which the connection maintains its initial stiffness until the onset of plastic

deformations through steel yielding and wood crushing, at which point the force continued to increase with a reduced stiffness. A representative curve is shown in Figure 4.13.
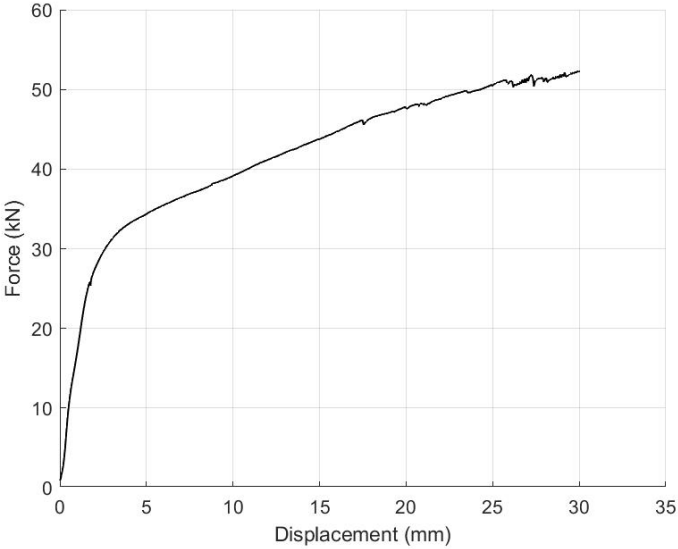
Figure 4.13: Typical Force-Displacement Relationship for Monotonic Steel Bolt Tests

The failure mode "g" that was designed for using Johansen's yield equations is clearly present in the steel bolted connections. In fact, all four bolts were able to develop three hinges, thereby limiting wood damage to the region closest to the wood-steel interface (Figure 4.14). Table 4.6 lists the steel bolted connection parameters calculated from the experimental results.

a.) Deformed Bolts

b.) Wood Crushing at 30 mm Displacement

Figure 4.14: Typical Damage from Steel Bolt Monotonic Tests

Table 4.6: Monotonic Steel Bolt Connection Test Results

Test #	P_{max}[a] (kN)	Δ_{max}[b] (mm)	k_i[c] (N/mm)	P_y[d] (kN)	Δ_y[e] (mm)
4SM1	52.8	30.0	14969	27.3	2.0
4SM2	60.7	31.7	14919	27.1	2.1
4SM3	46.7	14.2	16464	30.5	2.2
Average	53.4	25.3	15451	28.3	2.1
COV	0.11	0.31	0.05	0.06	0.04

[a] Maximum load recorded during the test.
[b] Displacement at the maximum load.
[c] Initial stiffness taken as the slope of force-displacement plot between 10% and 40% of P_{max}.
[d] Yield load determined using the 5% offset method.
[e] Displacement at yield load.

Cyclic tests of steel bolted connections demonstrated highly ductile behaviour, as expected. Figure 4.15 shows a slow decrease in strength as the hinges in the bolts softened and eventually broke, which is typical of steel bolted connections with yielding fasteners. A representative monotonic test is also shown in Figure 4.15.

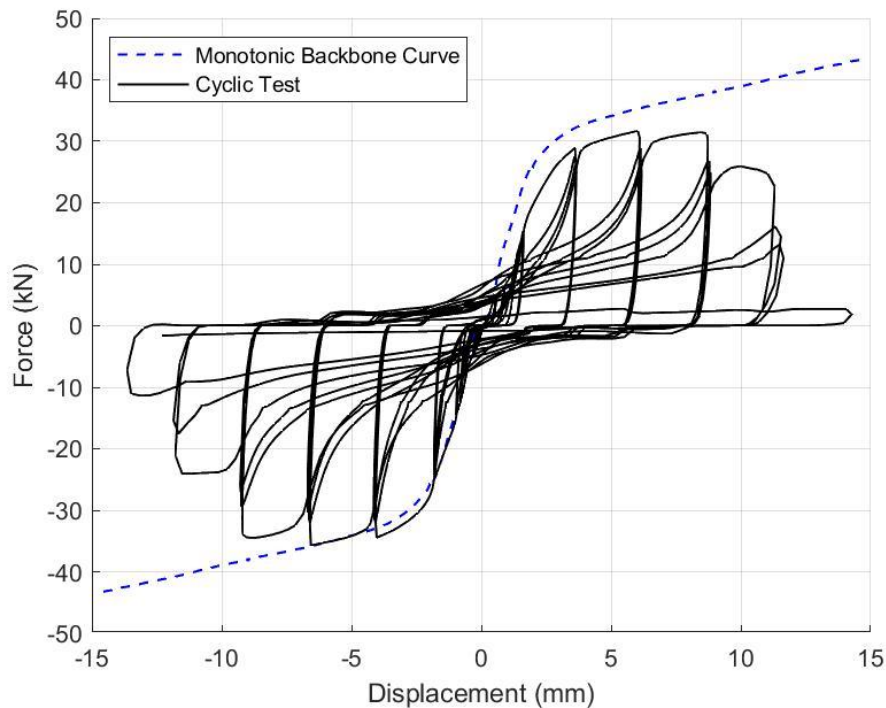**Figure 4.15:** Typical Force-Displacement Relationship for Cyclic Steel Bolt Tests

Figure 4.16 shows the damaged bolts and wood crushing profile for a steel bolted connection test under cyclic loading. Figure 4.16b) makes it clear that multiple hinges were able to form based on the wood crushing profile, and Figure 4.16a) shows that the middle hinge in the bolts is the one that eventually broke off.

c.) Deformed Bolts Broken at Center Hinge   d.) Wood Crushing

Figure 4.16: Typical Damage from Steel Bolt Cyclic Tests

Table 4.7 presents maximum loads in compression and tension cycles, the maximum displacement at these loads, and the stiffness for each steel bolted connection specimen tested.

Table 4.7: Cyclic Steel Bolt Connection Test Results

Test #	P_{max_c}[a] (kN)	Δ_{max_c}[b] (mm)	P_{max_t}[c] (kN)	Δ_{max_t}[d] (mm)	k[e] (N/mm)
4SC1	32.8	9.0	31.8	8.2	9898
4SC2	32.7	7.0	30.9	8.3	13350
4SC3	35.8	6.6	31.8	6.1	8378
Average	33.8	7.5	31.5	7.5	10542
COV	0.04	0.14	0.01	0.14	0.20

[a] Maximum load reached in compression cycle.
[b] Displacement when lead reached P_{max_c}.
[c] Maximum load reached in tension cycle.
[d] Displacement when load reached P_{max_t}.
[e] Stiffness of connection as slope from 10% to 40% of P_{max_t}.

Force-displacement curves and pictures of damage to wood and bolts for all steel bolted connection tests can be found in Appendix B.

4.4.2 SMA Bolts

A total of three monotonic and three cyclic tests were conducted on SMA bolted wood-steel-wood connections. The force-displacement relationship of all bolted SMA connection tests showed similar behaviour to the steel bolted connections when subjected to monotonic loads. A ductile failure mode was observed in which the connections maintained their initial stiffness until the onset of deformations through SMA bending and wood crushing, at which point the force continued to increase with a reduced stiffness. A representative curve is shown in Figure 4.17.
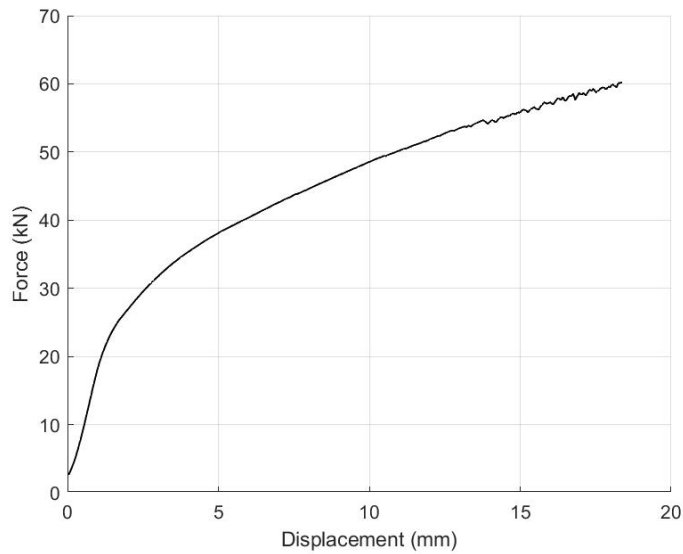
Figure 4.17: Typical Force-Displacement Relationship for Monotonic SMA Bolt Tests

Figure 4.18 shows that the SMA bolted connections experienced deformations corresponding to a mode "g" failure, per Johansen's yield model. Although only one hinge is visible when looking at the bolts after testing, the wood crushing profile suggests additional hinges formed in the bars but were not permanent due to the SMA's superelastic property.
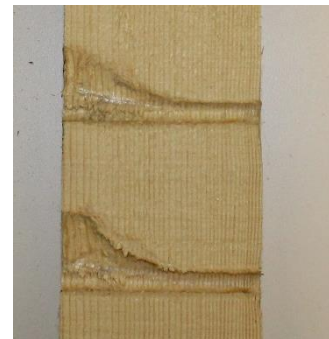
a.) Deformed Bolts with Permanent Deformation at Center

b.) Wood Crushing at 17 mm Displacement

Figure 4.18: Typical Damage from SMA Bolt Monotonic Tests

Table 4.8 presents the parameters calculated from experimental results for SMA bolted connections under monotonic loading.

Table 4.8: Monotonic SMA Bolt Connection Test Results

Test #	P_{max}[a] (kN)	Δ_{max}[b] (mm)	k_i[c] (N/mm)	P_y[d] (kN)	Δ_y[e] (mm)
4NM1	54.5	14.3	14655	28.7	2.2
4NM2	54.6	16.1	9706	29.4	2.8
4NM3	60.6	18.4	15630	26.3	1.9
Average	56.6	16.3	13330	28.1	2.3
COV	0.05	0.10	0.20	0.05	0.16

[a] Maximum load recorded during the test.
[b] Displacement at the maximum load.
[c] Initial stiffness taken as the slope of force-displacement plot between 10% and 40% of P_{max}.
[d] Yield load determined using the 5% offset method.
[e] Displacement at yield load.

Similar to the monotonic tests, the cyclic tests of SMA bolted connections led to deformations which resembled mode "g" in Johansen's yield model. While this is typically considered a ductile mode of failure, Figure 4.19 shows multiple sudden decreases in strength as SMA bolts sheared at the wood-steel interface during the cyclic tests. The force-displacement relationship of a representative monotonic test is also shown in Figure 4.19, and the sheared dowels are pictured in Figure 4.20 along with the wood crushing profile.
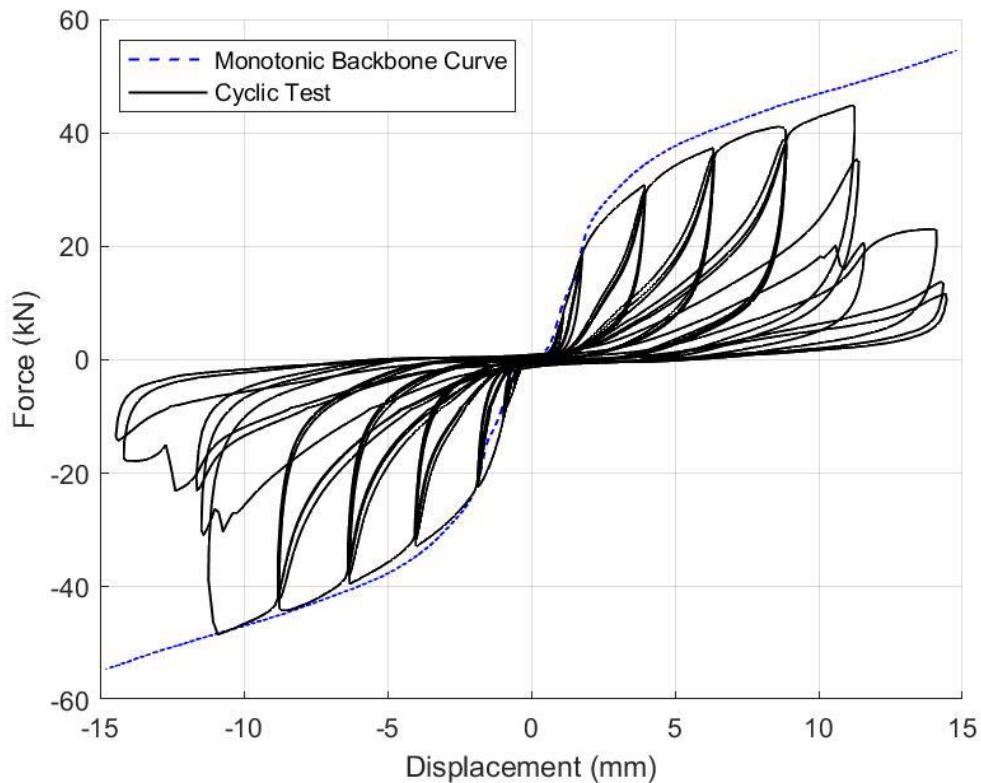
Figure 4.19: Typical Force-Displacement Relationship for Cyclic SMA Bolt Tests

| a.) Bolts Broken at Center | b.) Wood Crushing |
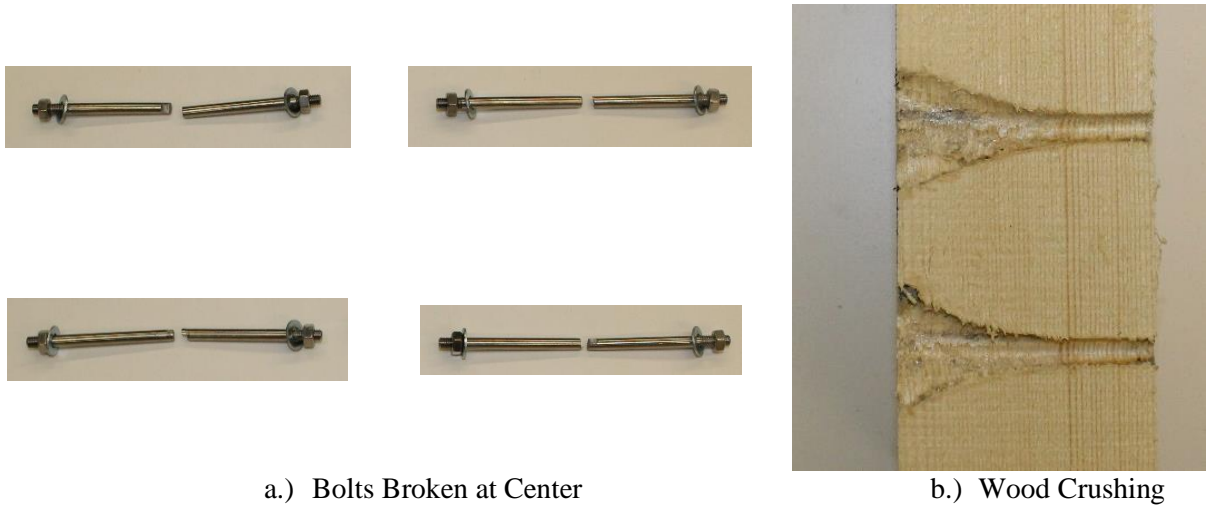
Figure 4.20: Typical Damage from SMA Bolt Cyclic Tests

Maximum loads in tension and compression cycles, displacements at maximum loads, and stiffness of each specimen tested were calculated and results are presented in Table 4.9.

Table 4.9: Cyclic SMA Bolt Connection Test Results

Test #	$P_{max\_c}{}^a$ (kN)	$\Delta_{max\_c}{}^b$ (mm)	$P_{max\_t}{}^c$ (kN)	$\Delta_{max\_t}{}^d$ (mm)	k^e (N/mm)
4NC1	43.2	11.5	41.0	9.50	11839
4NC2	41.1	9.1	42.7	8.37	13227
4NC3	47.2	12.0	43.6	10.5	10412
Average	43.8	10.9	42.4	9.5	11826
COV	0.06	0.12	0.03	0.09	0.10

[a] Maximum load reached in compression cycle.
[b] Displacement when lead reached P_{max_c}.
[c] Maximum load reached in tension cycle.
[d] Displacement when load reached P_{max_t}.
[e] Stiffness of connection as slope from 10% to 40% of P_{max_t}.

Force-displacement curves and pictures of damage to wood and bolts for all SMA bolted connection tests can be found in Appendix B.

Chapter 5 - Finite Element Modelling

5.1   Methodology

The analytical models developed included models of material tests performed (i.e., three-point bending tests, and glulam embedment tests), as well as a model of a single steel and SMA dowel connection. The goal of finite element modelling in this study is to develop a model capable of predicting the force-displacement behaviour of single dowel wood-steel-wood connections. Upon validation, this model could then be used to investigate the effects of dowel diameters, wood species, thickness of steel plate, etc. All models were made using Abaqus/CAE (Dassault Systemes, 2020).

Component tests included determining the embedment behaviour of the wood and the flexural behaviour of steel and SMA dowels. These load-displacement relationships were used to calibrate the finite element model material properties to be used as an input to the FEM of the connections. As discussed in the following sections, the initial properties (e.g., E_1) were selected from relevant studies that had similar materials as those investigated herein (Hong, 2007; Oliveira, 2021) and were modified until the analytical load-displacement curve reasonably captured the average of the experimental load-displacement curves. While material testing (i.e., coupon tension tests of bolts, and shear, tension, and compression tests of wood, etc.) would offer a better representation of the material used in experiments, time constraints prevented such tests from being completed. Future studies should seek to improve the models by including properties from appropriate material testing.

The upcoming section discusses the models used to calibrate material properties, and Section 5.3 explains the single dowel connection models with a single steel and SMA dowel.

5.2   Material Modelling

5.2.1 Wood Material Model

This model was developed to determine wood properties for the connection model. To do this, a finite element model of the embedment tests performed on wood was developed and results were compared to experimental tests. To limit computational time a half model of the test was made. The bottom of the wood member was fixed in the model, and symmetry boundary conditions were applied to the dowel and wood faces where the model was cut in half.

It has been found that the strength and stiffness of wood modelled analytically tends to be much higher than results obtained from experimental testing (Foschi, 1974; Hong, 2007; Karagiannis et al., 2016). Hong (2007) performed tests to obtain wood properties and used these properties to model the embedment behaviour of wood. Figure 5.1 shows that analytical results obtained from this study suggest that wood was much stronger and stiffer in an analytical model when compared to experiments.
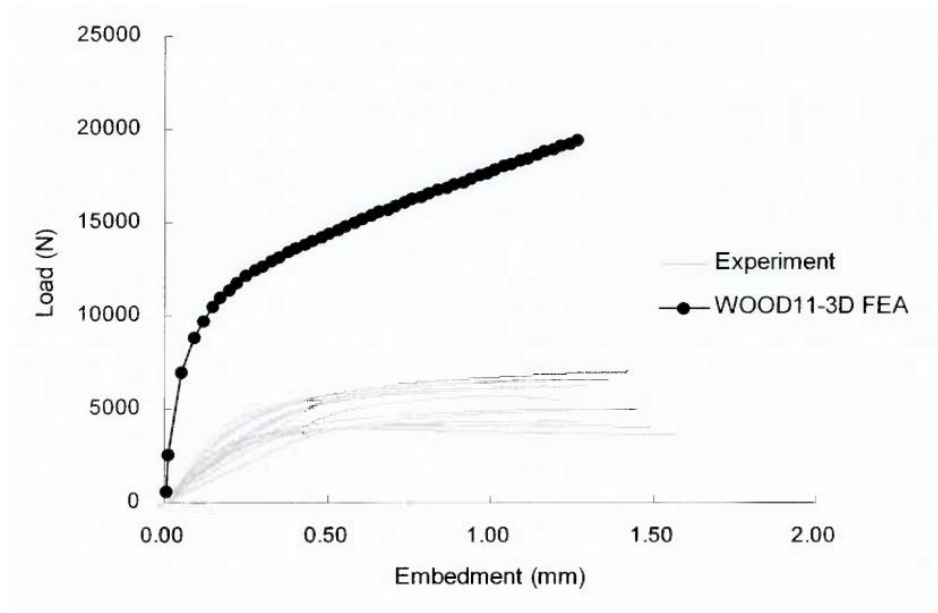
Figure 5.1: Wood Embedment Model Results Without a Foundation Zone (Hong, 2007)

Foschi (1974) proposed modelling wood with a softened foundation zone to capture the weakened behaviour of wood in crushing. This approach has since been adapted by Hong (2007) and Karagiannis et al. (2016) for various types of wood and fastener diameters. There currently exists no foundation zone property reduction factors for SPF glulam with ¼" (6.35 mm) diameter fasteners. However, Hong (2007) used reduced properties on Douglas-Fir for 6.4 mm diameter fasteners, and the modelling results showed good agreement with experimental tests. Since reduction factors are only available for SPF glulam with large diameter dowels, the factors from Hong (2007) are being used in this study.

Figure 5.2 shows the embedment test being modelled as well as the geometry of the half model. The model is made of three parts with different materials: the dowel, glulam, and the softened glulam foundation zone. A circular foundation zone with a diameter 4.5 times that of the dowel (28.6 mm) was chosen. This is the same size of foundation zone that was used by Hong (2007) for small diameter fasteners.

a) Embedment Test Setup
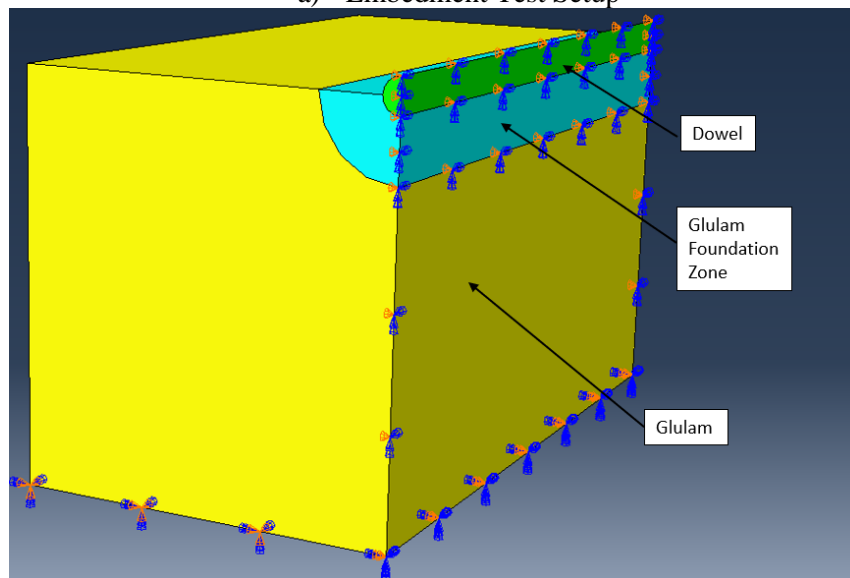
b) Half-Model Geometry

Figure 5.2: Embedment Test Model Parts and Boundary Conditions

To describe the behaviour of glulam, three different constituents must be prescribed: the elastic behaviour, inelastic behaviour, and the failure criteria that initiates the change from elastic to inelastic. Since wood is orthotropic, different strengths must be assigned in three directions relative to the wood grain. This was done in Abaqus (Dassault Systemes, 2020) by assigning "Engineering Constants" to an elastic material model (e.g., E_1, E_2, E_3, etc.), then prescribing the direction that corresponds to each strength assigned. The wood's strong direction (parallel to grain) is prescribed as being in the direction of loading, as was the case in the embedment tests. The material orientation is shown in Figure 5.3, while

Table 5.1 presents the material properties initially assigned to the wood. The modulus of elasticity of the wood in its strong direction (E_1) was taken from Oliveira (2021), who used SPF glulam of similar grade as to the current study, while other moduli were calculated from the equations below, which come from the CSA-086 standard (CSA, 2019):

$$E_2 = E_3 = \frac{E_1}{30} \tag{5.1}$$

$$G_{12} = G_{13} = \frac{E_1}{16} \tag{5.2}$$

$$G_{23} = \frac{G_{12}}{10} \tag{5.3}$$

Table 5.1: Regular Glulam Elastic Orthotropic Properties (Oliveira, 2021)

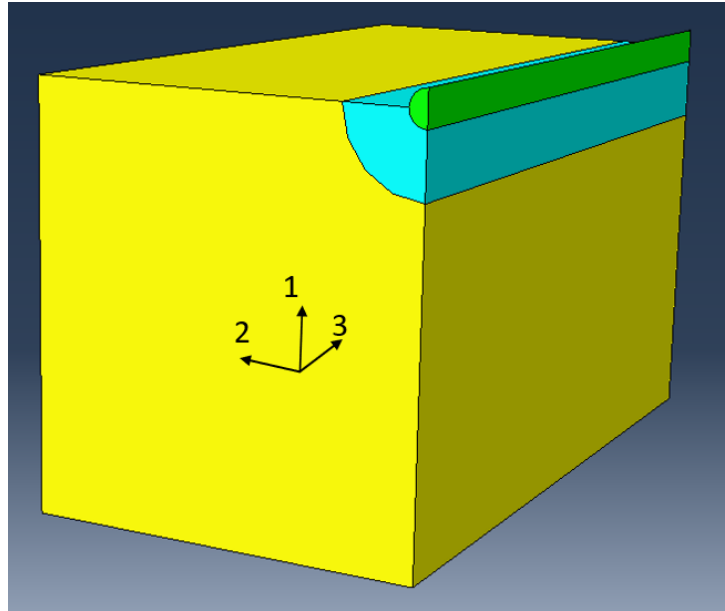| Property	Value
E_1 (parallel to grain)	12,400 MPa
E_2, E_3 (tangential and radial to grain)	413 MPa
v_{12}	0.47
v_{13}	0.37
v_{23}	0.44
G_{12}, G_{13}	775 MPa
G_{23}	78 MPa

Figure 5.3: Wood Material Orientation

The softened wood foundation zone's properties were determined using the same reduction factors as in Hong (2007) for 6.4 mm dowels in Douglas Fir. Table 5.2 presents the resulting properties of the foundation zone.

Table 5.2: Foundation Zone Glulam Elastic Orthotropic Properties

Property	Value
E1 (parallel to grain)	653 MPa
E2, E3 (tangential and radial to grain)	65 MPa
v_{12}	0.47
v_{13}	0.37
v_{23}	0.44
G_{12}, G_{13}	67 MPa
G_{23}	12 MPa

During the elastic phase, stresses and strains are computed in glulam elements using the following stress-strain relationship (ABAQUS, 2009):

$$\begin{bmatrix} \varepsilon_{11} \\ \varepsilon_{22} \\ \varepsilon_{33} \\ \gamma_{12} \\ \gamma_{13} \\ \gamma_{23} \end{bmatrix} = \begin{bmatrix} 1/E_1 & -v_{21}/E_2 & -v_{31}/E_3 & 0 & 0 & 0 \\ -v_{12}/E_1 & 1/E_2 & -v_{32}/E_3 & 0 & 0 & 0 \\ -v_{13}/E_1 & -v_{23}/E_2 & 1/E_3 & 0 & 0 & 0 \\ 0 & 0 & 0 & 1/G_{12} & 0 & 0 \\ 0 & 0 & 0 & 0 & 1/G_{13} & 0 \\ 0 & 0 & 0 & 0 & 0 & 1/G_{23} \end{bmatrix} \begin{bmatrix} \sigma_{11} \\ \sigma_{22} \\ \sigma_{33} \\ \sigma_{12} \\ \sigma_{13} \\ \sigma_{23} \end{bmatrix} \tag{5.4}$$

The strain is broken into elastic (ε_{el}), and plastic (ε_{pl}) components, and Equation (5.4) describes the elastic portion. To determine when the transition from elastic to plastic behaviour occurs, a failure surface was assigned using Hill's potential function for anisotropic yield (Abaqus, 2009):

$$f(\sigma) = \sqrt{F(\sigma_{22} - \sigma_{33})^2 + G(\sigma_{33} - \sigma_{11})^2 + H(\sigma_{11} - \sigma_{22})^2 + 2L\sigma_{23}^2 + 2M\sigma_{31}^2 + 2N\sigma_{12}^2} \tag{5.5}$$

When the function shown in Equation (5.5) equals unity, the wood transitions to the plastic phase (Janssen, 2017). The parameters F, G, H, L, M, and N are functions of the relations between stresses and yield stress in different directions (R_{11}, R_{22}, R_{33}, R_{12}, R_{13}, and R_{23}). These "R" values are the entries on Abaqus, and they were adopted from the study by Wang et al. (2014). The values are summarized in Table 5.3. For a more thorough analysis, experimental stress values should be used to compute these R-factors; however, these were sufficient to replicate connection behaviour.

Table 5.3: R-Value Entries for Hill's Criterion (Wang et al., 2014)

R-Value	Stress Relation (ABAQUS, 2009)	Value
R_{11}	σ_{11}/σ^0	1.000
R_{22}	σ_{22}/σ^0	0.836
R_{33}	σ_{33}/σ^0	0.777
R_{12}	σ_{12}/τ^0	0.986
R_{13}	σ_{13}/τ^0	0.816
R_{23}	σ_{23}/τ^0	0.816

σ^0 and τ^0 are yield stresses

In the model, a perfectly plastic state is assumed after the yield point, since the wood below the dowel is mainly being compressed parallel to grain, and wood in compression parallel to grain can be idealized as elastic-plastic. The plastic range of the wood is described using points to relate stresses and plastic strains (ε_{pl}). A yield stress of 47 MPa is chosen outside of the softened foundation zone, per Oliveira (2021). The yield stress is reduced to 19 MPa in the foundation zone when using the same reduction factor as Hong (2007). Strains start to become permanent when they reach a value of 0.02 or greater, per compression tests performed by Karagiannis et al. (2016).

In the model, contact was defined separately in the normal and tangential directions. For contact in the normal direction, a hard contact is assigned between the dowel and wood. For normal "hard contact", there is the following contact constraint on all surfaces that are assigned interactions (Abaqus, 2009):

$$p = 0 \ for \ h < 0 \tag{5.6}$$

$$h = 0 \ for \ p > 0 \tag{5.7}$$

In which p is the contact pressure between two surfaces, and h is the interpenetration of the surfaces. This means that when there is no interpenetration between surfaces ($h < 0$), there is no contact pressure ($p = 0$). And when the surfaces come into contact, a pressure (p) is computed to prevent penetration, thus ensuring the constraint of no interpenetration between parts (i.e., $h = 0$) (Abaqus, 2009).

Tangential contact is also assigned between the dowel and wood block using a penalty friction formulation with a friction coefficient of 0.7, as proposed by Smith (1983). The tangential contact constraint is enforced by the penalty method using the assigned friction coefficient. Tangential interaction between surfaces is described by a stick-slip mechanism, as shown in Equations (5.8) and (5.9):

$$stick: f = t_T - \mu|t_n| \leq 0 \tag{5.8}$$

$$slip: f = t_T - \mu|t_n| > 0 \tag{5.9}$$

In which t_n and t_T are described using penalty parameters. During slip and stick, the tangential stress vectors take the forms shown in Equations (5.10) and (5.11) respectively (Vulovic et. al, 2007)

$$t_{Ta}^{sl} = -\mu|t_n| \frac{g_{Ta}^{sl}}{g_T^{sl}} \tag{5.10}$$

$$t_{Ta}^{stick} = \varepsilon_T g_{Ta} \tag{5.11}$$

In which ε_T is the tangential penalty parameter. This penalty formulation allows Abaqus to compute the forces needed to push members back together when sliding or overlapping occurs (Vulovic et. al, 2007).

The final component of contact modelling in Abaqus consists of choosing which parts acts as "slave" and "master" surfaces. To get the best possible results when simulating contact, the slave surface should always be the more finely meshed surface. If mesh densities are similar between surfaces, then the softer material should act as the slave (Abaqus, 2017). For this reason, wood is modelled as the slave surface, while the dowel being pushed into the wood is the master surface.

For the embedment test model, the dowel and support were modelled as rigid and non-deformable parts. The dowel was loaded using a displacement-controlled line load up to a displacement of 3 mm along the line of symmetry where the model was cut. Rigid 4-node 3D elements (R34D) were used to mesh the dowel and support, and 8-node linear brick elements (C3D8R) were used to mesh the glulam. A variable mesh size was used to have a fine mesh (2 mm) in the dowel and foundation zone, and a coarse mesh (5 mm) in the remainder of the wood member where the behavior has a smaller influence on the global force-displacement relationship. The meshed model is shown in Figure 5.4.
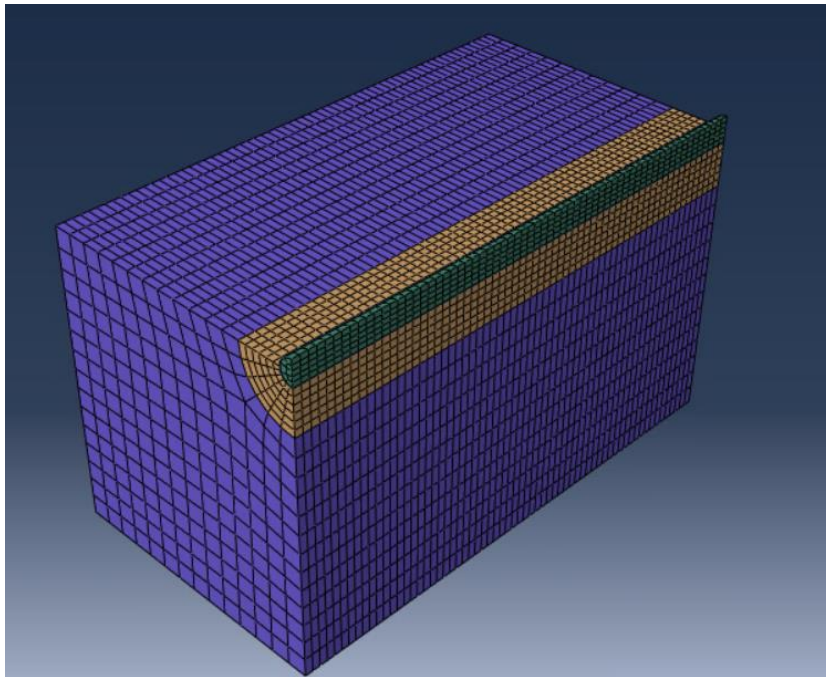

Figure 5.4: Meshed Embedment Test Model

The modelling force used to compare analytical and experimental results was the sum of all vertical reaction forces along the line on the dowel where the load was applied. This gives the total vertical force applied on the dowel. Then, displacement in the direction parallel to grain (vertical) at a single node on the line of symmetry was used as the displacement after confirming that all nodes along this line had the same displacement, thereby ensuring an even displacement of the dowel into the wood along the length of the specimen.

Using the properties provided in Table 5.1, force-displacement results were stiffer than the experimental results. The glulam material model was therefore switched to have an elastic modulus parallel to grain of 8500 MPa, and all other moduli were calculated accordingly. Table 5.4 and Table 5.5 present the new properties of glulam in and outside the softened foundation zone.

Table 5.4: Regular Glulam Elastic Orthotropic Properties - Modified

Property	Value
E_1 (parallel to grain)	8500 MPa
E_2, E_3 (tangential and radial to grain)	283 MPa
ν_{12}	0.47
ν_{13}	0.37
ν_{23}	0.41
G_{12}, G_{13}	531 MPa
G_{23}	53 MPa

Table 5.5: Foundation Zone Glulam Elastic Orthotropic Properties - Modified

Property	Value
E_1 (parallel to grain)	448 MPa
E_2, E_3 (tangential and radial to grain)	44 MPa
ν_{12}	0.47
ν_{13}	0.37
ν_{23}	0.41
G_{12}, G_{13}	46 MPa
G_{23}	8 MPa

Figure 5.4 shows all experimental force-displacement curves and results from the model with an E_1 of 12,400 MPa, and 8,500 MPa. Note that the modelling results were shifted to the right by 0.3 mm to make comparing experimental and modelling results easier. This was necessary since there was some initial slack in the experimental setup induced in the assembly of specimens before the load readings began going up, leading to zero force displacements at the beginning of each test.
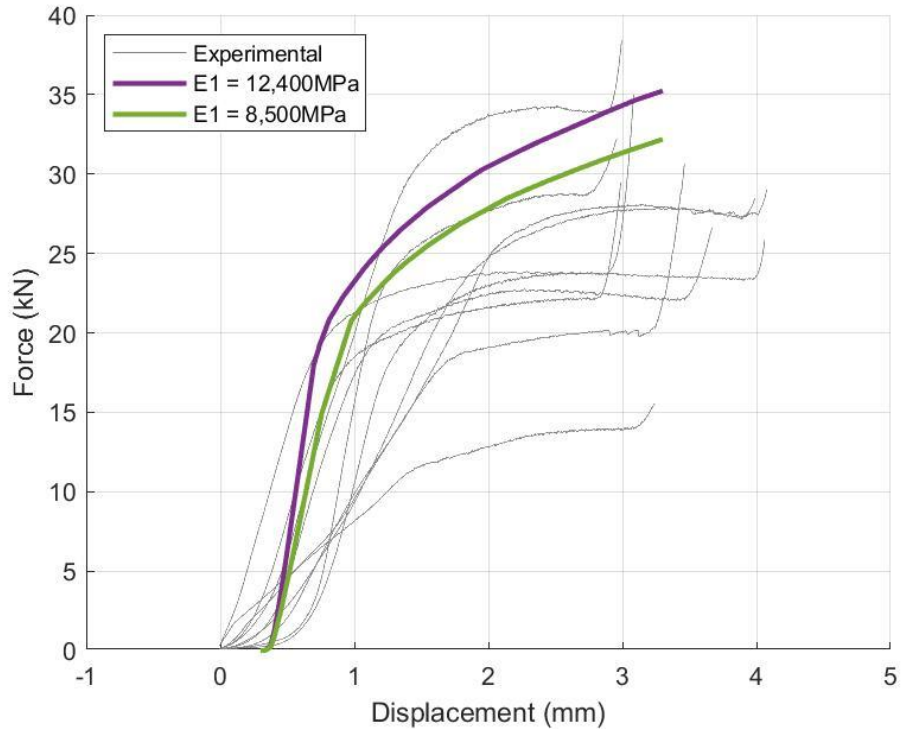
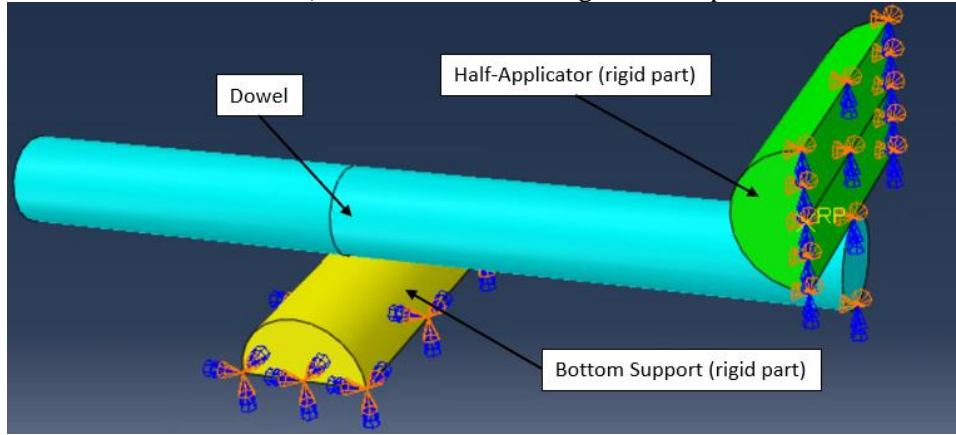**Figure 5.5:** Embedment Tests - Experimental and Modelling Results

Looking at Figure 5.4, it is clear that when E_1 is 8500 MPa, there is the best agreement with test results regarding both stiffness and strength of the wood model. The stiffness and yield point of the model show good agreement with experimental results. Post-yield behaviour in the model is slightly different than experimental, as the model's force-displacement behaviour fails to flatten at the onset of wood crushing. For the purposes of this study, this model is deemed sufficient. However, additional material testing should be completed to determine the yield stress ratios and improve the model's accuracy. In the connection model discussed in Section 5.3, wood properties presented in Table 5.4 and Table 5.5 are being used.

5.2.2 Dowel Material Models

A three-point bending test model was developed to determine the steel and SMA dowel properties for the connection model. The determination of the dowel properties was done in a similar manner as the wood properties in the previous section: by comparing experimental results to results from the test simulation in Abaqus. To limit computational time a half model of the test was made, and symmetry boundary conditions were applied on the cross-section of the cylindrical load applicator and the dowel at the line of symmetry, as shown in Figure 5.6.

69

a) Three-Point Bending Test Setup

b) Half Model Geometry and Boundary Conditions

Figure 5.6: Embedment Test Model Parts and Boundary Conditions

This model was used to verify the properties of the ASTM A307 steel bolts tested experimentally. These properties are well documented since this grade of bolts is commonly used in practice, so verifying that analytical and experimental results matched acted as confirmation that the model worked properly before using it to calibrate SMA properties.

In the model with the steel dowel, the stress-strain behaviour of the dowel first follows a simple linear elastic relationship, as described in Equation 5.12 (Abaqus, 2009).

$$\begin{bmatrix} \varepsilon_{11} \\ \varepsilon_{22} \\ \varepsilon_{33} \\ \gamma_{12} \\ \gamma_{13} \\ \gamma_{23} \end{bmatrix} = \begin{bmatrix} 1/E & -\nu/E & -\nu/E & 0 & 0 & 0 \\ -\nu/E & 1/E & -\nu/E & 0 & 0 & 0 \\ -\nu/E & -\nu/E & 1/E & 0 & 0 & 0 \\ 0 & 0 & 0 & 1/G & 0 & 0 \\ 0 & 0 & 0 & 0 & 1/G & 0 \\ 0 & 0 & 0 & 0 & 0 & 1/G \end{bmatrix} \begin{bmatrix} \sigma_{11} \\ \sigma_{22} \\ \sigma_{33} \\ \sigma_{12} \\ \sigma_{13} \\ \sigma_{23} \end{bmatrix} \quad (5.12)$$

A Young's modulus (E) of 210,000 MPa and a Poisson's ratio (v) of 0.3 are assigned, and Abaqus calculates the shear modulus (G) using Equation (5.13) (Abaqus, 2009):

$$G = \frac{E}{2(1+v)} \tag{5.13}$$

Following the linear-elastic phase, the steel dowel is assumed to transfer to a perfectly plastic state (i.e., no hardening). The plastic state has been set to begin at a stress of 439 MPa, which is the average yield stress obtained from experimental testing.

Similar to the embedment test model, normal and tangential contact properties were assigned between the dowel and both cylindrical bearing points. Again, hard contact was used in the normal direction, and the penalty method was used in the tangential direction with a friction coefficient of 0.5 (Wriggers, 2006) between the dowel and each bearing point. The dowel was assigned as the "slave" surface since the bearing points were modelled as rigid parts, making them much stronger than the dowels being bent.

Loading was assigned at a reference point on the half-applicator. Displacement-controlled loading up to 20 mm of displacement was applied, and force and displacement readings were taken directly from the reference point. The dowel was meshed using 8-node 3D stress (C3D8R) elements with a mesh size of 1 mm, and the support and load applicator were both modelled using rigid 4-node 3D elements (R34D). The meshed model is shown in Figure 5.7.
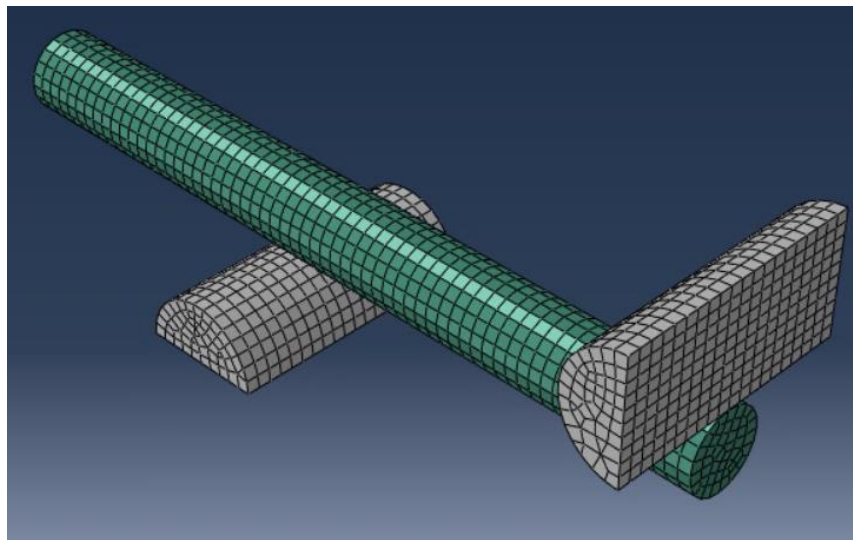

Figure 5.7: Meshed Three-Point Bending Model

Figure 5.7 shows an analytical and experimental force-displacement curve of three-point bending tests with steel dowels.
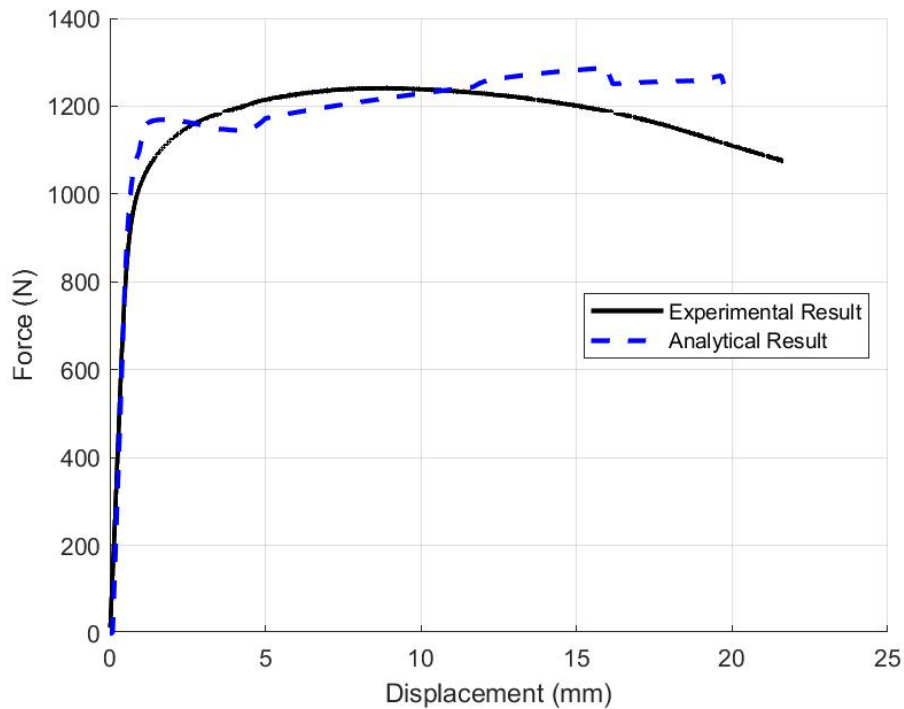
Figure 5.8: Experimental vs Analytical Results - Steel Dowels in Bending

Since the analytical model of steel in three-point bending shows good agreement with experimental results, a model with the same geometry, boundary conditions, contact properties, element type, and mesh size was used to replicate bending tests with SMA dowels.

To model self-centering SMAs, a superelastic material model based on Aurrichio et al. (1997) is available in Abaqus. The model requires inputs for elastic moduli and Poisson's ratios in the austenitic (E_a, v_a) and martensitic (E_m, v_m) phases, as well as stresses at which the transformation between both phases begin and end. Figure 5.7 illustrates the material model, and Table 5.6 presents typical Nickel-Titanium SMA properties, which were used as initial inputs in the model.
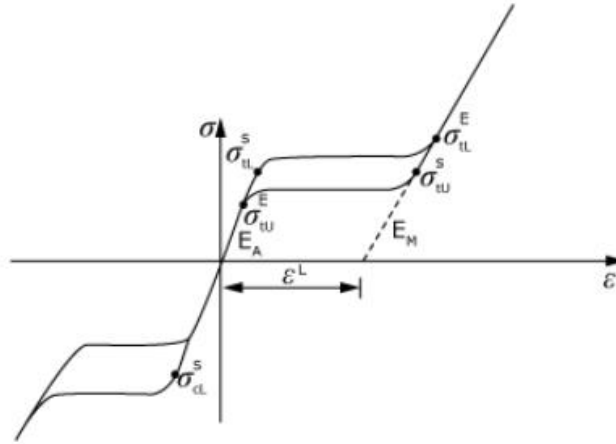
Figure 5.9: Superelastic Material Model in Abaqus (Abaqus, 2017)

Table 5.6: Nitinol Material Properties (Aurrichio et al., 1997)

Property	Value
E_a	60000 MPa
v_a, v_m	0.3
E_m	35000 MPa
ε_L	0.075
σ_{tL} (start)	520 MPa
σ_{tL} (end)	600 MPa
σ_{tU} (start)	300 MPa
σ_{tU} (end)	200 MPa

In which E and v are the elastic moduli and Poisson's ratios in the austenitic (subscript "a") and martensitic (subscript "m") phases, respectively. ε_L is a characteristic strain level, and σ_{tL} (start), σ_{tL} (end), σ_{tU} (start), and σ_{tU} (end) are transformation stresses. Note that, for instance, σ_{tL} (start) is the stress at which the transformation from austenite to martensite begins during loading (L).

As shown in Figure 5.9, the SMA behaviour is characterised by a linear portion, in which the material is in a fully austenitic state. There is then a transition phase from austenite to martensite in which a force plateau can be observed before the SMA becomes fully martensitic and regains a stiffness characterized by E_m. Thus, looking at Equation (5.12), before a stress of σ_{tL} (start) is reached, the elastic modulus and Poisson's ration used to compute stresses and strains are E_a and v_a. Then, there is a transition phase in which Abaqus computes the E and v using the relationships in Equations (5.14) and (5.15) (Abaqus, 2017):

$$E = E_a + \varphi(E_M - E_a) \tag{5.14}$$

$$v = v_a + \varphi(v_m - v_a) \tag{5.15}$$

In which φ is the fraction of martensite. Finally, when a stress of σ_{tL} (end) is reached, the elastic modulus and Poisson's ratio of the SMA becomes E_m and ν_m. The same principle applies during unloading, but with different transformation stresses denoted using the letter "U" (for unloading) in Table 5.6.

Properties listed in Table 5.6 were altered in the model until experimental and analytical results showed good agreement in force-displacement behaviour.

Table 5.7 presents the final SMA dowel properties being used in the connection model, and Figure 5.8 shows the analytical force-displacement behaviour of a dowel with these properties in the three-point bending model, along with the experimental results.

Table 5.7: Final SMA Dowel Properties for Modelling

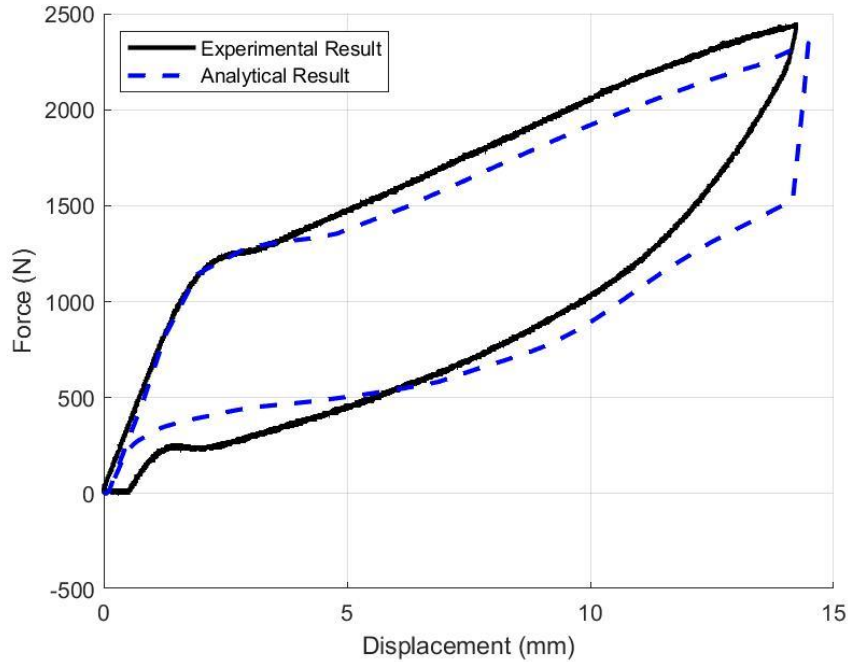| Property	Value
E_a	70000 MPa
ν_a, ν_m	0.33
E_m	25000 MPa
ε_L	0.03
σ_{tL} (start)	500 MPa
σ_{tL} (end)	550 MPa
σ_{tU} (start)	200 MPa
σ_{tU} (end)	100 MPa

Figure 5.10: Experimental vs Modelling Results of SMA Dowels in Three-Point Bending

74

While the peak strength and unloading path shown by the modelled SMA material model is not identical to the experimental results, the overall behaviour of an SMA bar in bending is captured quite well by the material model. Properties listed in Table 5.7 will therefore be used in the SMA dowel connection model.

5.3   Three-Dimensional Connection Model

The connection model discussed in this section introduces no new theory from what has been discussed in Sections 5.2.1 and 5.2.2. The materials used in this section follow the same stress-strain relationships as discussed in detail in previous sections, and contact properties between parts also follow the same mechanics as in previously discussed models. In this section, contact properties, material properties, and modelling results will be discussed without further explanation of the mechanics and theory that make the model functional. Readers can refer the previous sections for more theory.

The main goal of the analytical portion of this study is to develop a model capable of predicting the behavior of simple dowel connections using both steel and SMA dowels. Such connections were experimentally tested, and results from these tests are being used to verify analytical results. To limit computational time the model is focused on the connection rather than modelling the entire 500 mm piece of wood with a rigid bottom connection, as was tested in the laboratory. Additionally, only a quarter of the connection is modelled to take advantage of symmetry and further reduce computational time. This was done by cutting the model at the midspan of the dowel, and along the center of the cross-section of the dowel. Symmetry boundary conditions were employed on both faces of the dowels where cuts were made, as well as on the wood member and steel plates that were also cut in half. A full connection model is shown beside the quarter-model to help illustrate the use of symmetry in Figure 5.9. Boundary conditions are also shown on the quarter-model that was used to conduct the analytical study.
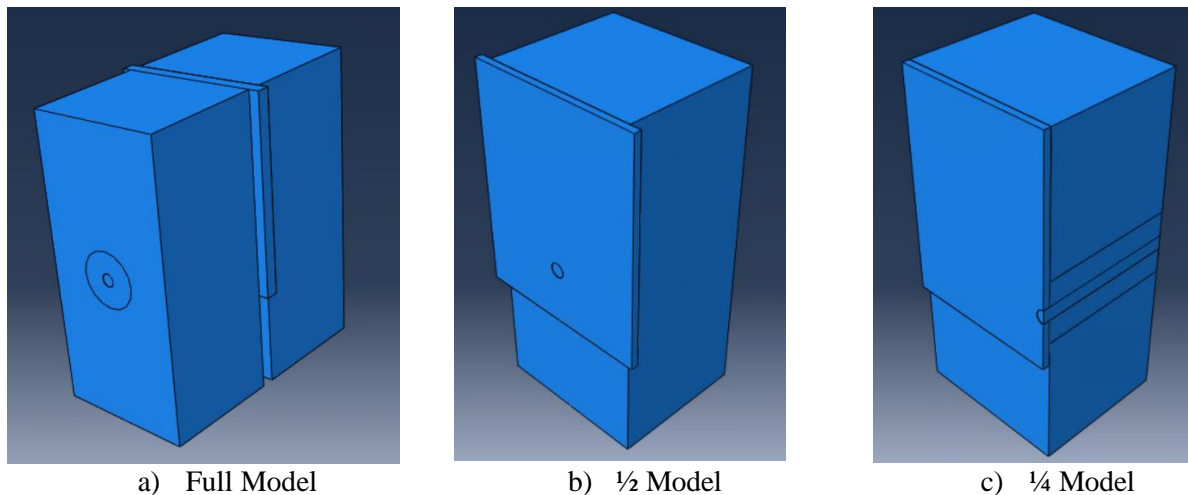

a)   Full Model   b)   ½ Model   c)   ¼ Model

Figure 5.11: Connection Model and Boundary Conditions

The steel plate was modelled as linear elastic with an elastic modulus of 210,000 MPa, and a Poisson's ratio of 0.3. The wood was modelled as elastic perfectly plastic using the properties found most adequate from the material model in Section 5.2.1. Table 5.4 presents these properties, and Table 5.5 presents the properties in the softened foundation zone. Yield ratios assigned in the model were the same ones used in the embedment model; these values are presented in Table 5.3.

The properties of the steel dowel are the same as the ones tested analytically in Section 5.2.2, since these properties led to three-point bending results which showed good agreement with experiments. Similarly, the SMA dowel properties used in the connection tests were the ones which best matched experimental tests when used in an analytical three-point bending model. These properties are presented in Table 5.7 in the previous section.

The contact formulation between parts used the same "hard" contact in the normal direction in all cases. The tangential contact between each component of the model is assigned the friction coefficients presented in Table 5.8.

Table 5.8: Tangential Contact Friction Coefficients

Contact Interaction	Master Surface	Friction Coefficient
Dowel - Steel Plate	Steel	0.5[1]
Wood - Dowel	SMA	0.7[2]
Wood – Steel Plate	Steel	0.7[2]

[1](Wriggers, 2006), [2](Smith, 1983)

The friction between the wood and steel plate uses the same coefficient that was used for metal-metal contact in Section 5.2.2, and the friction between wood and any metal is the same as the coefficient used between the dowel and wood in Section 5.2.1.

Results from the connection models with an SMA and steel dowel are presented and compared to experimental results in Chapter 6.

Chapter 6 - Discussion

This chapter is separated into five sections, each addressing one of the five main objectives of the thesis, as outlined in Section 1.2. The first three sections provide an interpretation of experimental results at various phases of the experimental program. The fourth section discusses the results of the finite element model; limitations of the model are also discussed. Finally, Section 6.5 looks at whether the strength of connections with SMA dowels or bolts can be predicted using the EYM, and other factors such as cost and availability of the material are briefly discussed to determine the feasibility of using SMAs as fasteners.

6.1   Self-Centering Abilities of SMAs in Bending

The first objective of this study was to establish the self-centering abilities of SMAs in bending to help gauge the feasibility of using SMA bars as slender dowels in wood-steel-wood connections. As mentioned in the literature review, SMAs are more often used in pure tension (Ma et al., 2008; Miller et al., 2012; Qiu & Zhu, 2017) as opposed to bending.

SMA bars were therefore tested in a semi-cyclic protocol and the force-displacement results were initially shown in Figure 4.2. In these semi-cyclic tests, cycles reaching displacements up to 7.5 mm showed no residual deformations upon unloading. The first cycle at which residual displacements could be observed was at the 11 mm cycle, at which point a residual displacement of less than 0.5 mm was measured. Additional damage was observed at every cycle beyond the 11 mm cycle, but even the highest displacement cycle (22 mm) led to permanent displacements of under 6 mm. The 11 mm and 22 mm cycles are shown in Figure 6.1 and Figure 6.2 respectively, along with pictures of the bars at maximum displacement (b) and upon unloading (c).
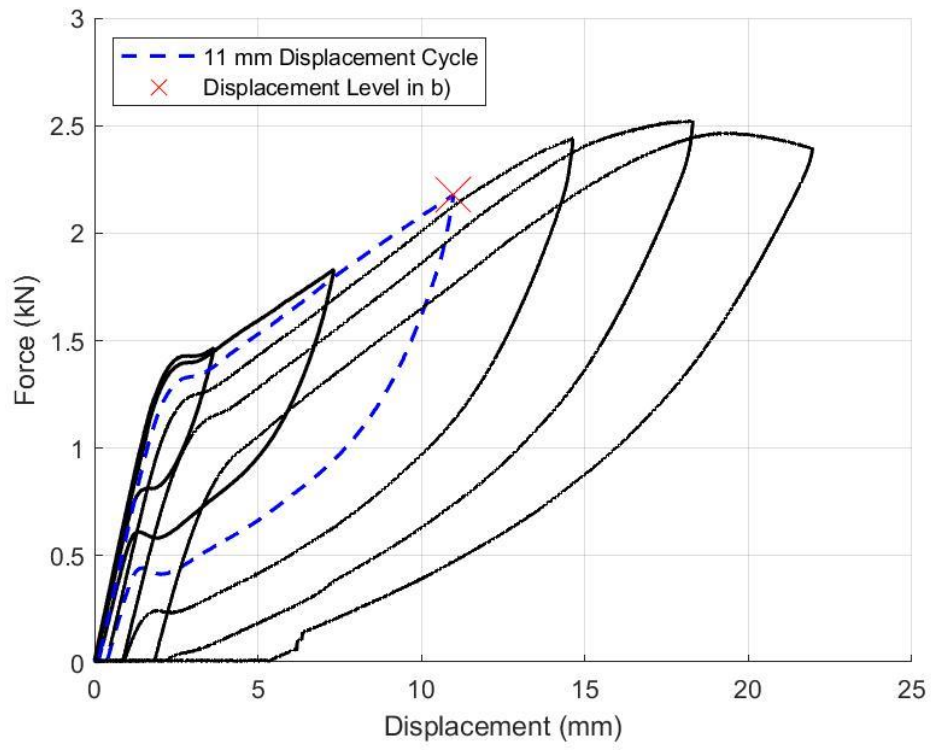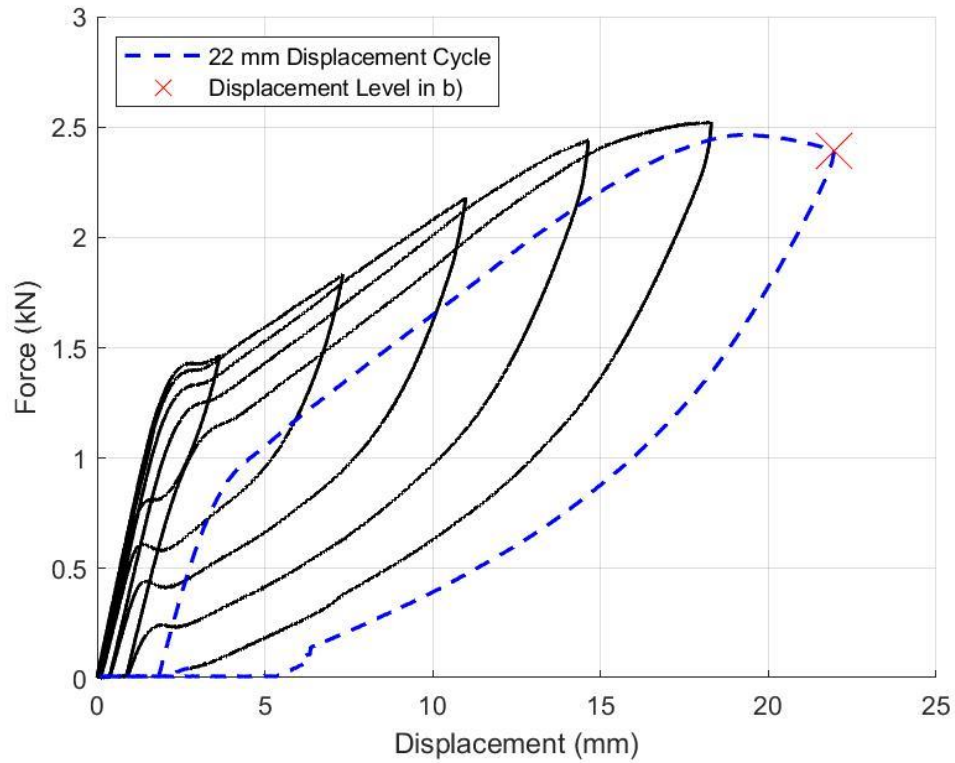
a) 11 mm Cycle
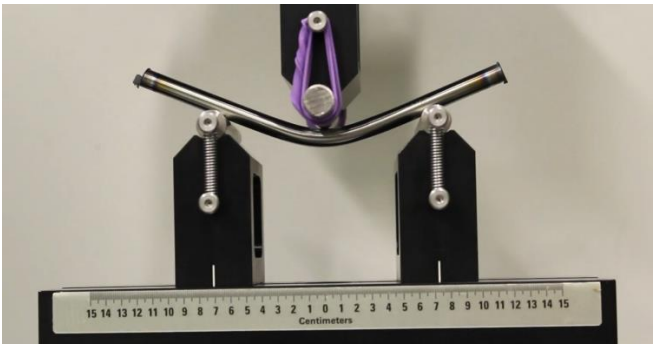
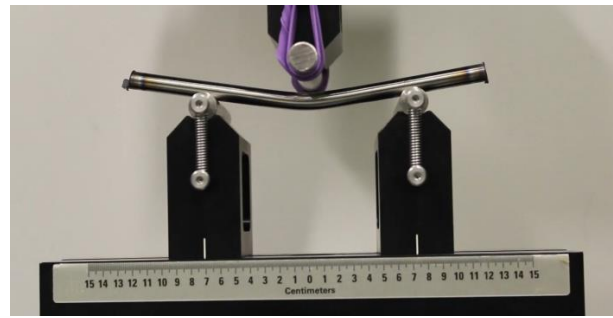**b)** Bent Bar at 11mm Displacement   **c)** Residual Damage After 11 mm Cycle
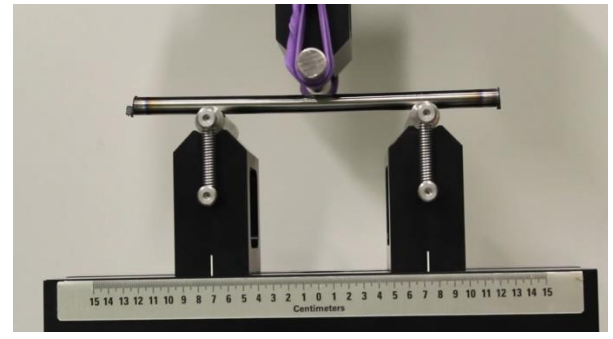
Figure 6.1: Self-Centering of SMAs in Bending at 11 mm Cycle

a) 22 mm Cycle

b) Bent Bar at 22 mm Displacement

c) Residual Damage After 22 mm Cycle

Figure 6.2: Self-Centering of SMAs in Bending at 22 mm Cycle

These results show that the superelastic SMA bars have excellent abilities to re-gain their shape, even after being subjected to large bending deformations. In comparison, the steel dowels with a similar diameter started experiencing permanent damage after approximately 2 mm (i.e., at the yield point). This suggests that SMAs could potentially be used as resilient slender fasteners in timber connections, since slender fasteners in wood connections are specifically designed to bend to prevent high stresses in wood members.

6.2   Comparison of Single Steel and SMA Dowel Connections

Once the self-centering ability of SMA bars in bending was established, the next objective was to compare the behaviour of straight steel and SMA bars in wood-steel-wood connections. Single plain bars were used for these tests to simply compare steel and SMA material as dowels, irrespective of clamping effects from bolt heads, or group effects from having multiple fasteners.

   Monotonic tests were first performed on the single bar connections. Figure 6.3 shows a representative force-displacement curve of a connection with both materials, while Table 6.1 presents the average values calculated for parameters used to evaluate connection performance.
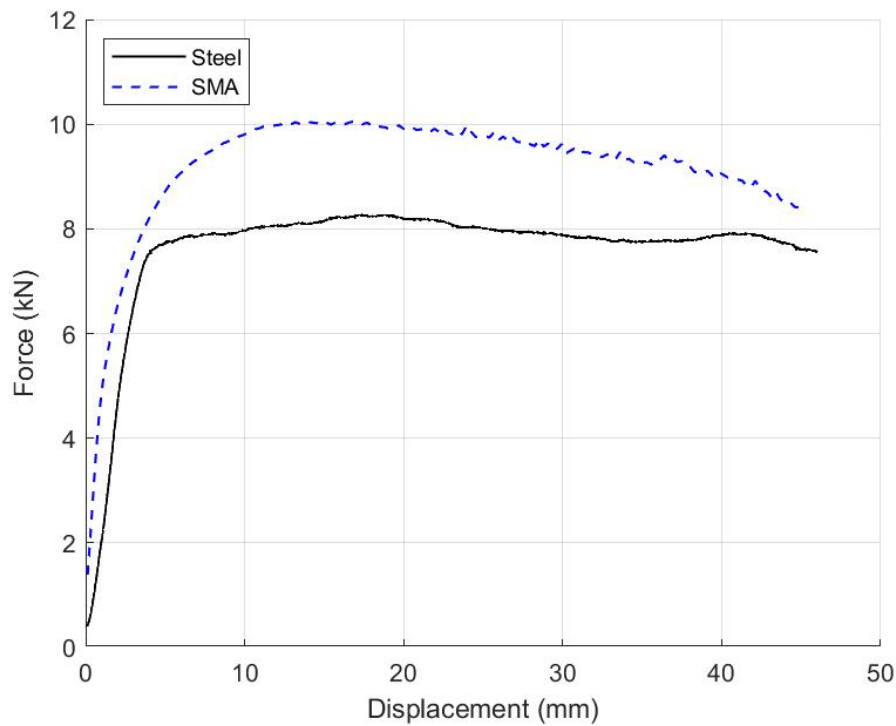
Figure 6.3: Representative Single Steel and SMA Dowel Connection Curves

Table 6.1: Summary of Data - Single Dowel Monotonic Tests

Test Description	P_{max}[a] (kN)	Δ_{max}[b] (mm)	k_i[c] (N/mm)	P_y[d] (kN)	Δ_y[e] (mm)
Steel - Average	9.1	27.6	5226	6.0	2.1
Steel - COV	0.08	0.39	0.60	0.15	0.54
SMA - Average	11.6	18.8	4622	5.6	1.4
SMA - COV	0.08	0.18	0.09	0.04	0.01

[a] Maximum load recorded during the test.
[b] Displacement at the maximum load.
[c] Initial stiffness taken as the slope of force-displacement plot between 10% and 40% of P_{max}.
[d] Yield load determined using the 5% offset method.
[e] Displacement at yield load.

The force-displacement data shows that the steel and SMA dowel wood-steel-wood connections can withstand significant deformations following the onset of a yield point in the connection. A yield point in the steel connections is characterized by wood crushing and dowel yielding, which leads to elastic-perfectly plastic behaviour as a plastic hinge forms in the dowel. This behaviour is typical of wood dowel-type connections with slender steel dowels. Meanwhile, a yield point in the SMA connections is caused by wood crushing and a reduced stiffness in the dowel due to the transformation from austenite to martensite. The force-displacement behaviour therefore does not become perfectly-plastic, but instead experiences a slowly decreasing stiffness until a peak load is reached and the load-carrying capacity begins to drop. Consequently, the average connection yield load recorded in the steel tests was slightly higher than that recorded in the SMA connections. The less pronounced elastic to plastic transition of the SMA bolts lead to a more rounded force-displacement curve leading up to the peak, causing the 5% offset line used to determine the yield load to intersect the force-displacement plot at a lower load level. This is illustrated in Figure 6.4, where the steel force-displacement curve has been shifted by 5 mm to better show the difference between the two curves.
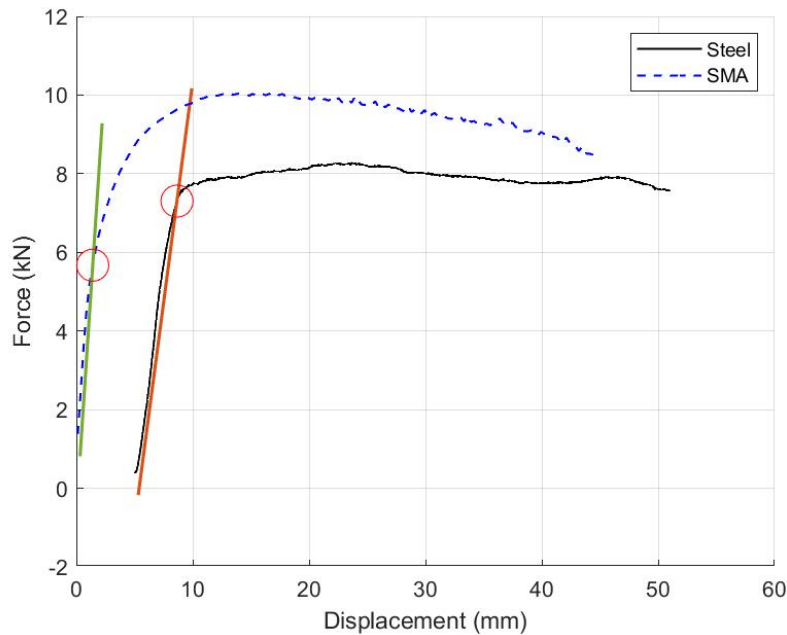

Figure 6.4: Yield Determination for Steel vs SMA Dowel Connection

Other observations from Table 6.1, are that the SMAs increase the strength of the connection due to their higher bending strength, and while the average stiffness of steel connections is slightly higher, this is mainly due to a single outlier that had a recorded stiffness of 9550 N/mm. All other single dowel steel tests had stiffnesses below the average recorded during SMA tests (4622 N/mm). The reason behind the

81

specimen with a high stiffness is unclear based on observations made after cutting open the wood specimen and is attributed to the inherent variability in wood.

Another note to make regarding the monotonic tests is that one of the SMA dowels sheared suddenly at a displacement of approximately 35 mm. All other specimens were able to reach the chosen maximum displacement of 45 mm without failure, which suggests that consistency and predictability of the SMAs were not as good as that of the steel bars, which were cut from A307 steel bolts.

After the monotonic tests, three cyclic tests were conducted on single steel and SMA dowel connections. As expected, once steel dowels yielded, they offered little resistance during a reverse loading cycle. This is clear by looking at cyclic force-displacement curves provided in Figure 6.5, where the force drops to zero and the force-displacement curve travels along the x-axis during reverse loading. In contrast, the force-displacement curves of SMA dowel connections moved back towards the origin during reverse loading, thereby showing that the dowels were able to re-center even at high displacements.
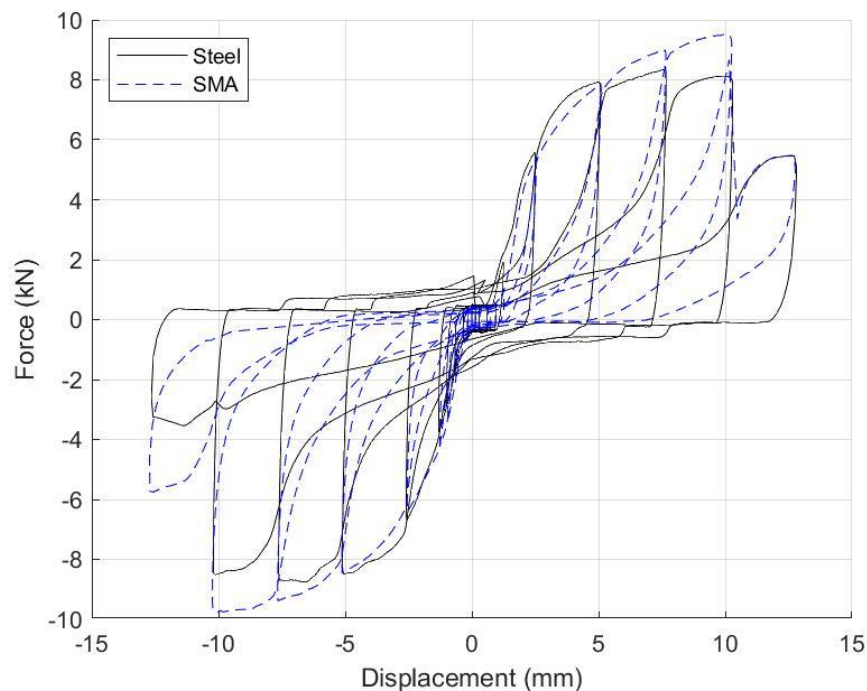
Figure 6.5: Steel vs SMA Representative Force-Displacement Curves (1ˢᵗ Cycles, Single Dowel)

The steel dowel connection tests behaved in a highly ductile manner, in which a plastic hinge formed at the center of the bolt and slowly lost capacity as it was cycled. Meanwhile, SMA dowels sheared in a sudden manner at the wood-steel interface after being cycled many times, without showing any signs of upcoming failure before the break. The steel dowels were consistent in when they broke, failing at the 18ᵗʰ

cycle each time, while SMA dowels failed at the 18th, 17th, and 14th cycles during the three tests performed. This provides further evidence that the SMA bars are less consistent and reliable when compared to A307 grade steel in bending in a wood-steel-wood connection. Parameters used to evaluate the connection behaviour are provided in Table 6.2, and Figure 6.6 shows representative envelope curves for a steel and SMA dowel connection test. The envelope curves consist of points at the maximum load attained at each cycle.
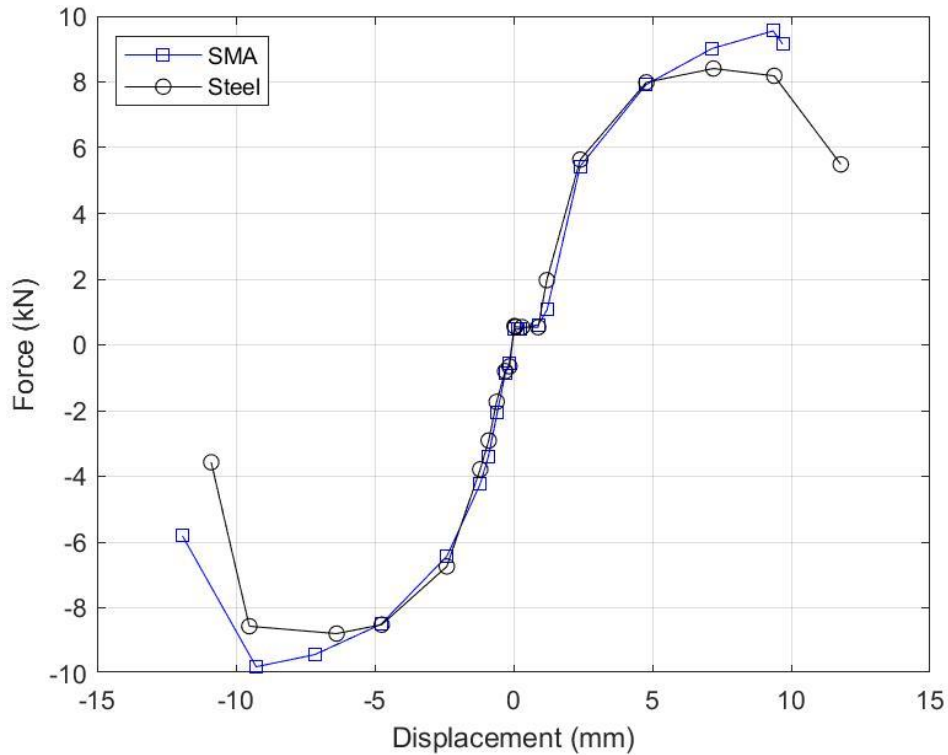
Figure 6.6: Typical Envelope Curves for Single Dowel Cyclic Tests

Table 6.2: Summary of Data - Single Dowel Cyclic Tests

Test Description	P_{max_c} [a] (kN)	Δ_{max_c} [b] (mm)	P_{max_t} [c] (kN)	Δ_{max_t} [d] (mm)	k [e] (N/mm)
Steel – Average	8.6	7.0	8.3	7.6	2654
Steel - COV	0.04	0.06	0.01	0.004	0.04
SMA – Average	10.1	9.0	10.0	9.1	5638
SMA - COV	0.06	0.11	0.06	0.12	0.28

[a] Maximum load reached in compression cycle.
[b] Displacement when lead reached P_{max_c}.
[c] Maximum load reached in tension cycle.
[d] Displacement when load reached P_{max_t}.
[e] Stiffness of connection as slope from 10% to 40% of P_{max_t}.

Table 6.2 and Figure 6.6 indicate that the connection with an SMA dowel reaches a higher peak load and has a higher initial stiffness. The increased capacity attained when using a single SMA dowel instead of steel did not cause the failure mode of the connection to change, as the wood damage shown in Appendix B shows that three hinges formed in both steel and SMA dowels during testing. However, the increased bending strength of the SMA caused slightly more wood crushing.

The final metric used to evaluate the connections is the area enclosed within the force-displacement curves, which was calculated at each cycle as a measure of energy dissipation. Table 6.3 summarizes the results for cyclic steel and SMA dowel tests. It should be noted that areas are only shown for cycles with displacement levels of 1.2 mm and above, since lower displacements were too sensitive to the slack caused by oversizing the holes. The areas shown are those of the first cycle for each given displacement level, and therefore account for the energy dissipated by wood crushing. Area enclosed by the curves at cycles repeated at a given displacement level were not calculated, but they are expected to follow the same trend as the first cycle.

Table 6.3: Average Area Below Force-Displacement Curves for Single Dowel Connection Tests

Cycle Displacement (mm)	Cycle Areas by Test Specimen		Ratio of SMA/Steel
	Steel	SMA	
1.2	2.6	2.8	1.1
2.4	16.4	11.8	0.7
4.8	55.3	38.4	0.7
7.2	77.7	56.6	0.7
9.6	90.6	46.9	0.6
12	61.6	20.1	0.3

Table 6.3 indicates that steel dowel connections dissipate more energy, even if SMA dowel connections reached a higher peak load. This is because of the self-centering abilities of SMAs, which helps the connection push back towards zero displacement during reverse cycles. This self-centering effect reduces the area enclosed by the force-displacement curve, thereby reducing the energy-dissipation capabilities of the connection.

In short, single SMA dowel connections showed good self-centering and increased strength and stiffness when compared to steel dowel connections. However, steel dowel connections were more consistent, dissipated more energy, and failed in a more ductile and predictable manner.

6.3   Comparison of Steel and SMA Bolted Connections

This section discusses results from connections with four SMA and steel bolts. Like in the previous section, connections using both steel and SMA dowels are evaluated based on various criteria such as self-centering abilities, peak load, stiffness, ductility, and energy dissipation.

Monotonic tests were first performed on the connections. Figure 6.7 shows a representative force-displacement curve of a connection with each material, while Table 6.4 presents the average values calculated for parameters used to evaluate connection performance. Values in Table 6.4 are calculated for data up to 15 mm of displacement, since not all tests were stopped at the same displacement level, and a comparison of connections loaded to different levels would not be meaningful. Full force-displacement relationships for each test can found in Appendix B.
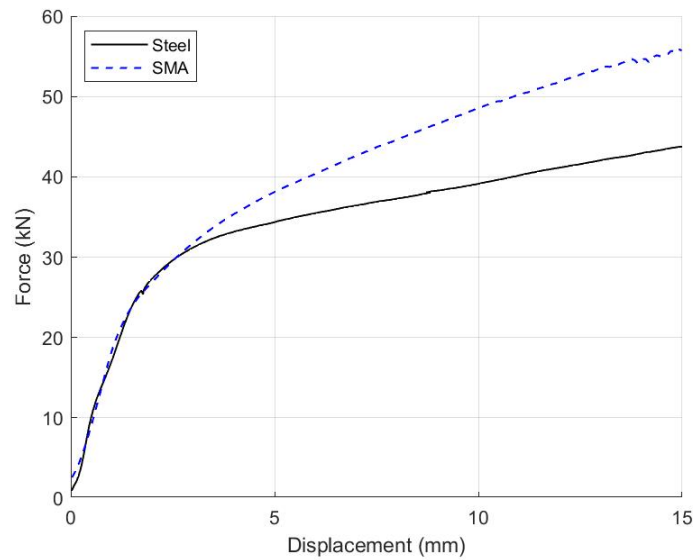
Figure 6.7: Representative Monotonic Bolted Connection Curves - Steel vs SMA

Table 6.4: Summary of Data - Bolted Monotonic Tests

Test Description	P_{max}[a] (kN)	Δ_{max}[b] (mm)	k_i[c] (N/mm)	P_y[d] (kN)	Δ_y[e] (mm)
Steel - Average	44.8	15.0	15451	28.3	2.1
Steel - COV	0.03	0.00	0.05	0.06	0.04
SMA - Average	54.5	15.0	13330	28.1	2.3
SMA - COV	0.02	0.00	0.20	0.05	0.16

[a] Maximum load recorded.
[b] Displacement at the maximum load.
[c] Initial stiffness taken as the slope of force-displacement plot between 10% and 40% of P_{max}.
[d] Yield load determined using the 5% offset method.
[e] Displacement at yield load.

Similar to the single dowel connections, the force-displacement data shows that the steel and SMA bolted connections can withstand significant deformations following the onset of plastic deformations. Again, SMAs increase the strength of the connection due to their higher bending strength, and the average stiffness of steel connections is higher. It should be noted that an outlier in the SMA connection tests significantly lowered the average stiffness. It is believed that this was due to the intersection of fasteners with an imperfection in the wood grain, since the wood began cracking at low displacements compared to all other tests. Besides this discrepancy, steel and SMA bolted connections under monotonic loading had very similar initial stiffnesses. Besides differences in peak load and initial stiffness, monotonic test results for connections with steel and SMA bolts showed similar force-displacement behaviour. Large deformations could be reached once the connections had been considered "yielded", which indicates high connection ductility using both materials.

Cyclic tests were then performed on the steel and SMA bolted connections. Representative force-displacement curves for each material are shown in Figure 6.8; only the first cycle at each displacement level is shown to provide a clearer picture. Representative envelope curves for each material are shown in Figure 6.9, and Table 6.5 presents average data calculated from connection tests with each type of bolt.
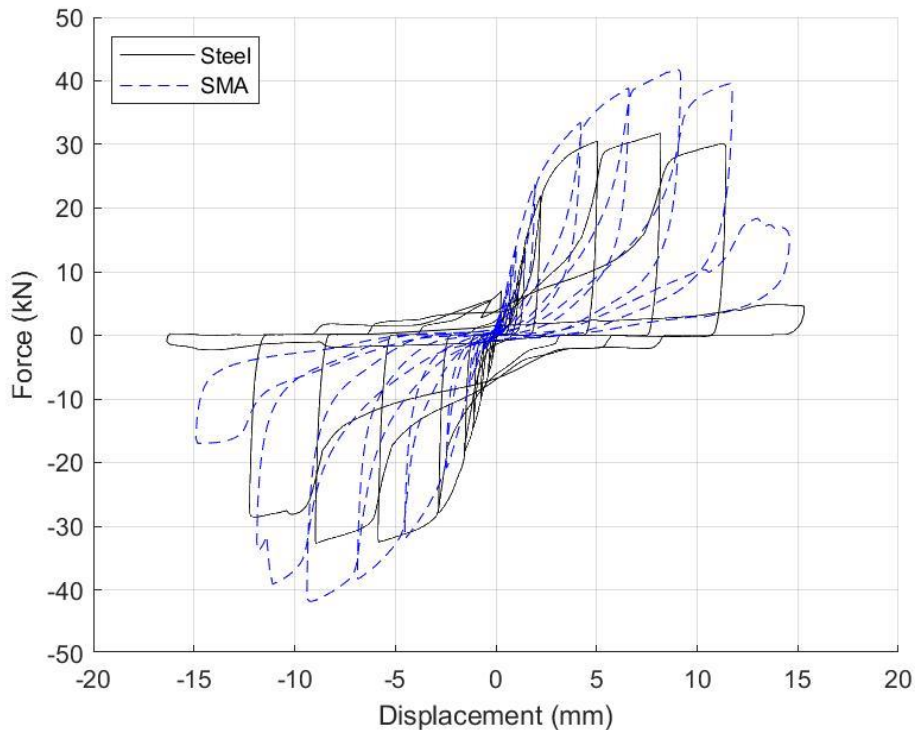
Figure 6.8: Steel vs SMA Representative Force-Displacement Curves (1st Cycles, Four Bolts)
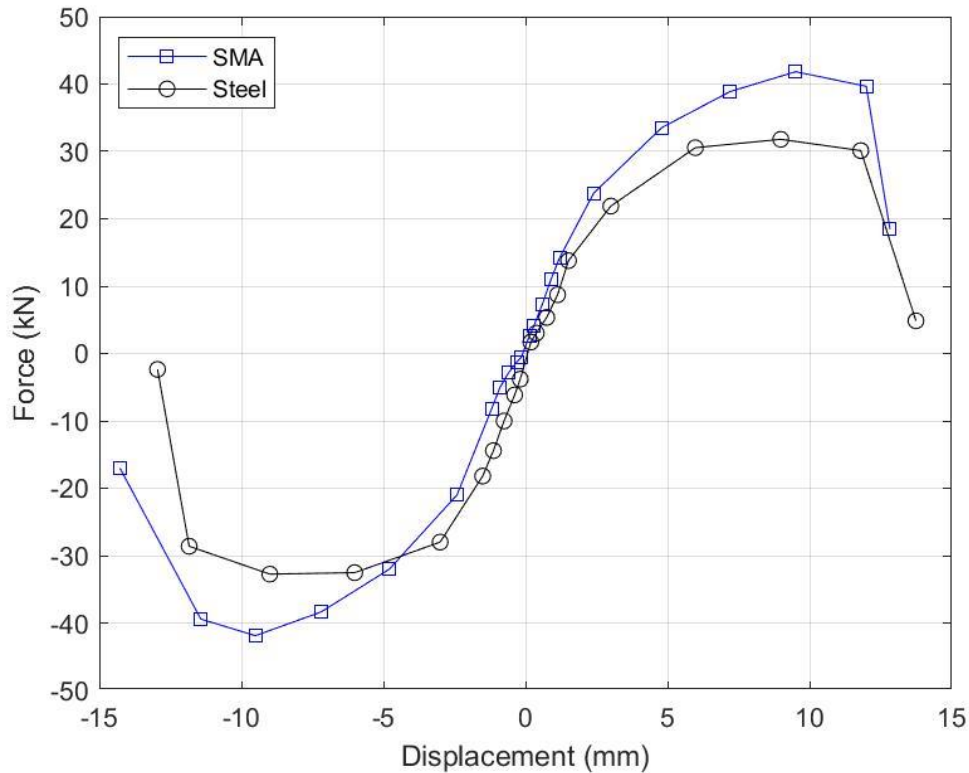
Figure 6.9: Steel vs SMA Envelope Curves – Bolted Connection Tests

Table 6.5: Summary of Data - Bolted Cyclic Tests

Test Description	$P_{max\_c}^{a}$ (kN)	$\Delta_{max\_c}^{b}$ (mm)	$P_{max\_t}^{c}$ (kN)	$\Delta_{max\_t}^{d}$ (mm)	k^{e} (N/mm)
Steel - Average	33.8	7.5	31.5	7.5	10542
Steel - COV	0.04	0.14	0.01	0.136	0.20
SMA - Average	43.8	10.9	42.4	9.5	11826
SMA - COV	0.06	0.12	0.03	0.09	0.10

[a] Maximum load reached in compression cycle.

[b] Displacement when lead reached P_{max_c}.

[c] Maximum load reached in tension cycle.

[d] Displacement when load reached P_{max_t}.

[e] Stiffness of connection as slope from 10% to 40% of P_{max_t}.

Self-centering of the SMA bolts is effective, as suggested by the force-displacement curves that return towards the origin during reverse loading (Figure 6.8).

The envelope curve and test data show similar trends between steel and SMAs used as bolts as the trends that were observed in the single dowel tests. SMA bolts allow connections to reach a higher peak load, and consistently give the connection a higher stiffness. Bolted steel connection tests were stopped when all four bolts yielded and broke in half, leading to load readings near zero. This happened on the 18th cycle during one test, and the 21st cycle for the two others. Meanwhile, SMA bolted connection tests

87

were stopped when all four bolts were snapped, which was evident since the bolts fractured at the steel-wood interface causing a loud cracking noise. Prior to the first SMA bolt failing, there was no indication of softening in the connection behaviour. Once the first one failed, the other three bolts were able to take a reduced load for some time before the next one broke, until none were left. All bolts were broken at the 21st cycle twice, and the 23rd cycle once.

Area enclosed within the force-displacement curve was calculated at each cycle beyond 1.2 mm of displacement. Results are presented in Table 6.6.

Table 6.6: Area Below Force-Displacement Curves by Cycle for Bolted Steel Connection Tests

Cycle Displacement (mm)	Cycle Areas by Test Specimen		Ratio of SMA/Steel
	Steel	SMA	
1.2	9.3	8.0	0.9
2.4	36.8	28.5	0.8
4.8	178.5	119.4	0.7
7.2	286.3	197.1	0.7
9.6	357.3	282.8	0.8
12	224.8	205.1	0.9
14	34.9	62.2	1.8

Once again, due to the SMA's self-centering ability, energy dissipated by the connections with SMA bolts is lower than steel bolted connections at nearly every displacement level.

In summary, similar trends were observed in bolt group connections as in the single dowel connections. SMA bolted connections showed excellent self-centering abilities and increased strength when compared to steel dowel connections. The ability of the bolted connections to continue to withstand the load with its remaining bolts after a bolt failed also gives the illusion of increased ductility of connections if only looking at the envelope curves. However, the lack of a warning sign before the failure of individual SMA bolts is unfavorable, and results in sudden large drops in load-carrying capacity when looking at the full force-displacement relationships. Additionally, steel dowel connections dissipated more energy than connections with SMA bolts.

6.4   Modelling Results

Force-displacement relationships obtained from steel and SMA 3D models under monotonic loading are shown in Figure 6.10, along with the experimental curves from the single dowel tests with each material.
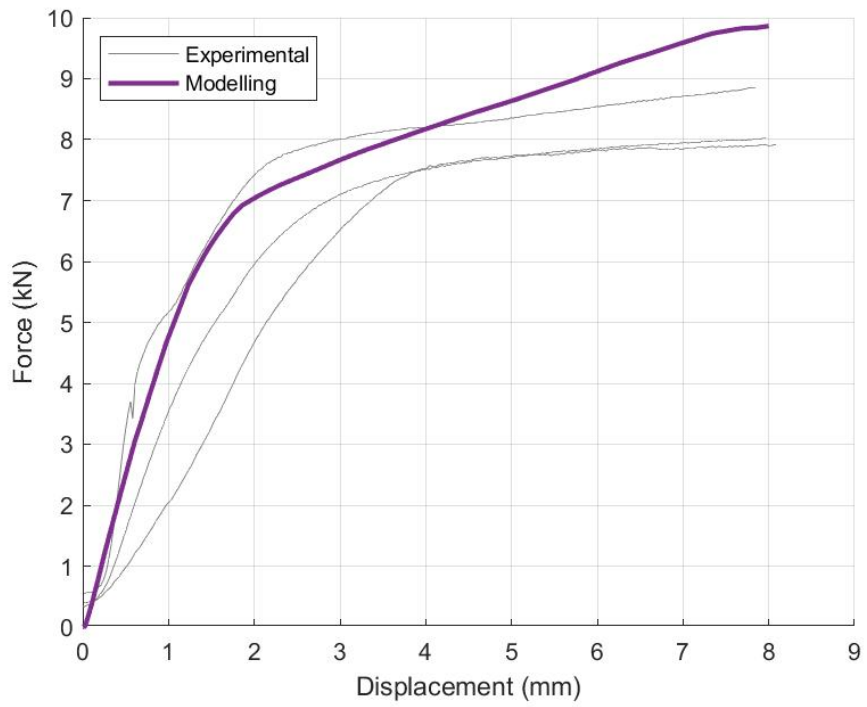
a) Steel
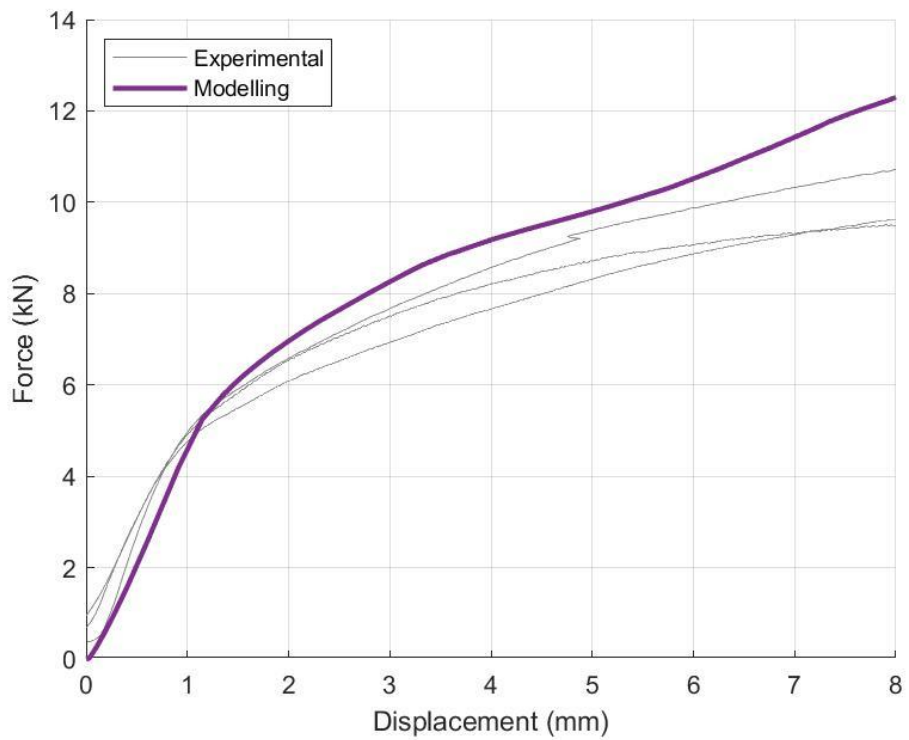
b) SMA

Figure 6.10: Monotonic Force-Displacement Curves - Modelling vs Experimental

Figure 6.10 shows that the model was able to replicate quite closely the behaviour of SMA and steel dowels in a single dowel wood-steel-wood connection. The behaviour before the connection yield point, and the initiation of yield are represented quite closely by the model. However, the post-yield stiffness of the model is higher than what was seen in experimental tests for both steel and SMA dowel connections. This is likely due to the wood model which displayed a post-crushing stiffness, as shown in Figure 5.5.

Looking at the deformations in the model, I can also see that the deformation mechanism looks similar to the Mode "g" failure that was seen in experiments. This failure mode is characterized by wood crushing and two hinges in the fastener. An example for the steel dowel is shown below, but the SMA model showed similar crushing.
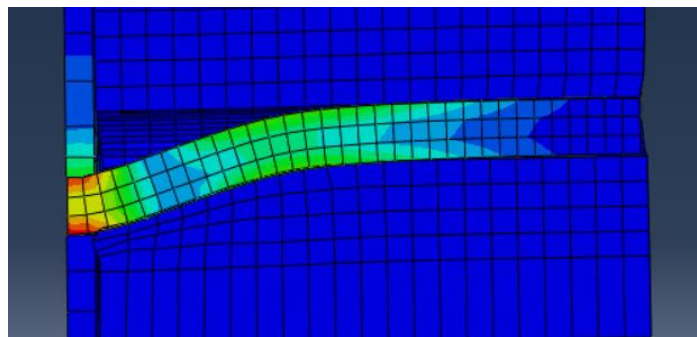
Figure 6.11: Wood Crushing in Model

Based on the similarity between monotonic force-displacement relationships of the model and experiments, it can be concluded that the model can accurately predict the stiffness of SMA and steel single dowel connections, and at which load level such connections will fail. Further material testing would need to be conducted to accurately predict the behaviour of connections at high displacements, beyond their point of failure.

6.5   Feasibility of SMA Dowels

The final objective of this study is the evaluate the feasibility of using SMAs as fasteners to create resilient timber connections. Results from the experimental and analytical investigations should be considered when gauging the feasibility of SMAs as fasteners, but these factors have already been discussed in sections 6.1 to 6.4. This section focuses on factors that are not performance-based: ease of design and implementation, cost, and availability.

One of the advantages of using SMA dowels to create a self-centering system is that designers can already easily design timber dowel-type connections, and the self-centering ability of the connection would come directly from the dowels rather than a new form of connector. As discussed in Chapter 2, Johansen's Yield Equations are used to design traditional timber dowel-type connections with slender

fasteners. The applicability of Johansen's Yield Model (EYM) to predict the strength of SMA dowel and bolted connections is evaluated by comparing experimental results to resistances calculated using the equations. Seven different failure modes are possible based on the EYM (see Table 2.1), so the calculated governing failure mode is also compared to the mode observed during experiments. Brittle failure modes not covered by the EYM were also checked and did not govern the design of any connections tested. Results of this analysis are presented in Table 6.7.

Table 6.7: Experimental vs Calculated Connection Strength and Failure Mode (5% Offset Method)

Test Series	Expected Failure Mode	Observed Failure Mode	Calculated Strength (kN)	Average Experimental Strength (kN)	% Difference
Single Dowel – Steel	g	g	7.3	6.0	- 17.8
Single Dowel – SMA	g	g	8.3	5.6	- 32.5
Four Bolt – Steel	g	g	29.2	28.3	- 3.08
Four Bolt – SMA	g	g	33.3	28.1	- 15.6

Comparing experimental and calculated strengths in the single dowel connections does not provide great insight into the effectiveness of the equations. In fact, both the steel and SMA single dowel connection strengths were not predicted with good accuracy. This is likely because wood is highly variable and when relying on the crushing below only one dowel, the resistance obtained in experiments would have been highly sensitive to the area directly below this fastener. An important takeaway from the comparison of single dowel tests results with EYM calculations is that all specimens failed in the expected failure mode (mode "g").

Looking at the four bolt connection results, the EYM can predict the strength and failure mode of steel bolted connections with great accuracy. However, when using the SMA's bending yield strength to compute connection capacity, the calculated strength of the connection increases while keeping the same expected mode of failure (mode "g"). While the mode of failure is accurately predicted, the connection yield strength from experimental results decreased. The experimental strength of the connections was taken as the yield load using the 5% offset method. This may not be a good representation of the true connection strength when SMA dowels are used since the SMAs re-gain a stiffness once the stress-induced transformation from austenite to martensite is complete. In contrast, when steel yields it loses nearly all its load carrying capacity.

Since the 5% offset method did not seem to accurately calculate connection strength from experimental tests on connections with SMA fasteners, the EEEP method (ASTM, 2019) was then used to compute the yield strength of connections. A comparison of yield strength from the EEEP method and theoretical strength calculated using Johansen's Yield Equations is provided in Table 6.8.

Table 6.8: Experimental vs Calculated Connection Strength and Failure Mode (EEEP Method)

Test Series	Expected Failure Mode	Observed Failure Mode	Calculated Strength (kN)	Average Experimental Strength (kN)	% Difference
Single Dowel – Steel	g	g	7.3	7.0	- 4.1
Single Dowel – SMA	g	g	8.3	8.5	+ 2.4
Four Bolt – Steel	g	g	29.2	26.8	- 8.2
Four Bolt – SMA	g	g	33.3	37.0	+ 11.1

While the difference between experimental strength calculated from the EEEP and the theoretical strength from the EYM is less than when the 5% offset method was used, results remain too far to be able to rely on this method. The next two figures illustrate the differences between experimental strengths using the two methods (5% offset and EEEP), and the calculated strengths for both single dowel and four bolt tests. Note that steel curves are offset by 5 mm for better illustration.
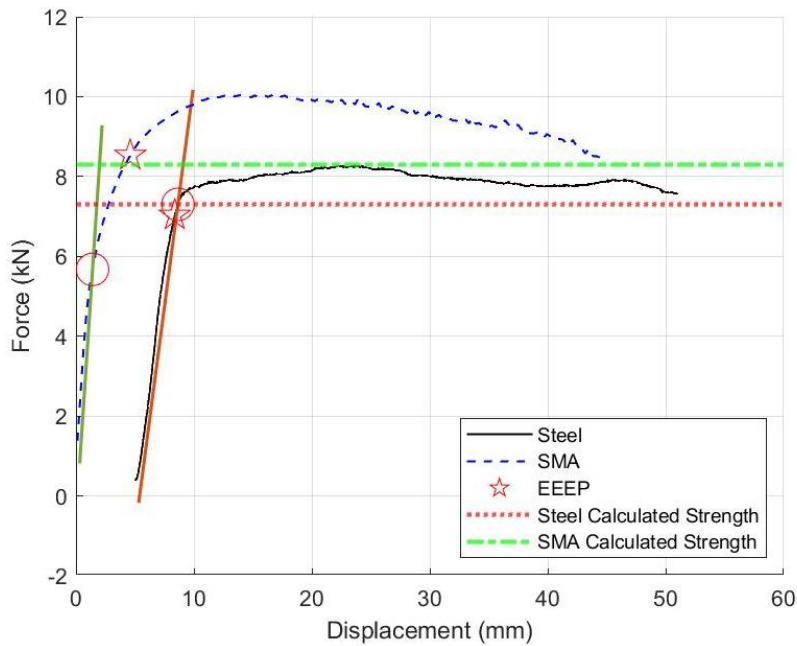
Figure 6.12: Experimental vs Calculated Strengths – Representative Single Dowel Tests
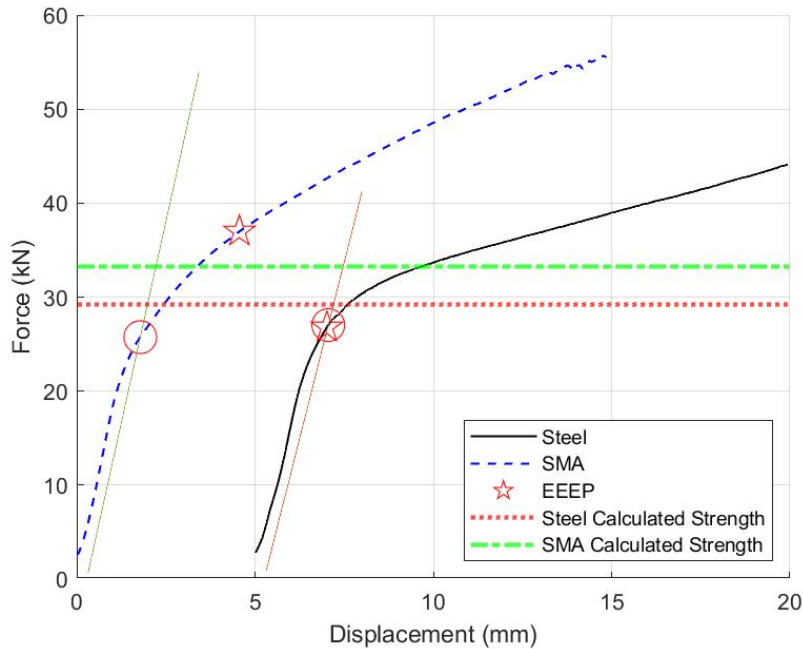
Figure 6.13: Experimental vs Calculated Strengths – Representative Four Bolt Tests

In short, if SMAs are to be designed using the EYM, it is suggested that a resistance modification factor be introduced to the Johansen's Yield Equations with deformation modes where dowels experience bending (i.e., modes "d", "e", and "g", per Table 2.1). This would ensure that designers can take advantage of the strength increase from using SMAs instead of steel, which is evident by looking at the peak loads attained by connections with each material (see P_{max} in Table 6.1, Table 6.2, Table 6.4, and Table 6.5), but not well-represented when connection strength is calculated using the 5% offset method (see Table 6.7).

A second factor not relating to the performance of SMA dowels that should be considered is the cost of the material. The nickel-titanium alloys used in this study are the most widespread superelastic material available on the market, but the price of both minerals used to create the alloy makes this SMA an expensive option. As discussed in Chapter 2, researchers have been looking to develop superelastic copper- and iron-based SMAs, but the superelastic effect has yet to reach the same level of effectiveness as NiTi SMAs. Results of studies seeking to improve the self-centering abilities of these alternative alloys are promising, however. As cheaper and more effective alloys using less expensive minerals are developed, the cost of superelastic SMAs should become lower. When effective superelastic copper- and iron-based SMAs become available to the market, they should be tested in cyclic bending and shear to determine whether they are better suited as dowels than the NiTi bars tested in this study.

Chapter 7 - Conclusions

7.1   General Remarks

Based on the experimental and analytical results presented and analyzed in this thesis, the following conclusions were drawn about the use of nickel-titanium SMA bars as fasteners in timber connections:

- The substitution of traditional steel dowels and bolts for superelastic SMA dowels and bolts in wood-steel-wood connections successfully provided the connections with a self-centering ability. This shows great promise for the use of SMAs as fasteners to develop resilient timber based SFRSs.

- The overall strength of connections was increased when using SMA fasteners instead of steel. However, steel fasteners showed higher energy-dissipation and more predictable force-displacement behaviour, free of sudden drops in load carrying capacity.

- The sudden nature of the SMA bar failures in cyclic shear is cause for concern. The cyclic shear failures of bolts led to large and sudden drops in load-carrying capacity. In contrast, the steel fasteners softened as a plastic hinge formed, thereby leading to a slow and gradual decrease in load carrying capacity after a peak load was reached.

- Permanent damage in the form of wood crushing remained present and seemed slightly higher when using SMA fasteners due to their increased bending strength. Future studies should seek to minimize wood crushing by using smaller diameter bars, a different connection detail or using SMAs with a lower transformation stress to martensite, which effectively acts as the "yielding" stress.

- The model developed using Abaqus/CAE (Dassault Systemes, 2020) could predict the monotonic behaviour of wood-steel-wood connections with steel and SMA dowels with good accuracy. The model is limited to predicting failure modes described by the EYM, which includes deformations in the form of dowel bending, and wood crushing. Brittle failure modes such as row shear and perpendicular-to-grain splitting are not captured in the model. These failure modes are not expected to govern in connections examined in this study, and this was proven to be true during experimental tests.

- The Johansen's Yield Equations used to predict yielding failure modes in wood connections would need to be modified to be capable of predicting the strength of connections with SMA dowels or bolts. This is due to the different bending force-displacement relationship displayed by

SMAs when compared to the nearly perfect elastic-plastic transition in traditional steel dowel-type fasteners.

In summary, while the nickel-titanium SMA dowels and bolts show promising results in terms of self-centering abilities when used in wood-steel-wood connections, their tendency to suddenly break in shear under cyclic loading introduces new considerations for designing dowel-type connections with this material. More tests would need to be conducted on NiTi SMAs in cyclic shear to determine whether the cyclic failures can be avoided in design, or if the use of this material in dowels should be avoided altogether. Iron-based SMAs are superelastic alloys currently in the research phase; as this novel material becomes more widespread, it could become a cheaper and more ductile replacement for the NiTi bars used in this study. Different connection details should also be looked at to take advantage of the NiTi SMAs' self-centering ability without subjecting them to cyclic shear loads.

7.2 Recommendations for Future Work

It is recommended that future studies seeking to use SMAs to create self-centering timber connections consider the following observations from this study: 1.) NiTi SMAs used as dowels can provide connections with a self-centering ability, and 2.) NiTi SMA dowels and bolts experienced sudden shear failures at the wood-steel interface when subjected to cyclic loading.

Prospects of future work on the topic discussed in this thesis have been identified while considering the main takeaways of the study. Recommendations for future work are outlined below:

- Explore the cyclic bending and shear behaviour of other superelastic alloys (e.g., copper- or iron-based SMAs) as they become more readily available in order to determine whether they are better suited as dowels than the nickel-titanium alloys used in this study. An investigation into the cyclic bending and shear behaviour of copper- or iron-based SMAs could offer valuable insights into the feasibility of these alternatives to develop resilient connections.

- If a different superelastic alloy (e.g., copper- or iron-based SMA) is found to be suitable as a dowel, adjustment factors for the EYM should be calculated for this material. The study should consist of an empirical study where many tests are performed with different bolt group arrangements and different connection details (e.g., wood-steel-wood, steel-wood-steel, etc.). This would allow the average designer to be able to design a resilient dowel-type connection with equations currently available in Canadian design standards.

- Analytical and experimental study on the global force-displacement behaviour of a braced frame equipped with the self-centering SMA dowel connections. The analytical study should use experimental force-displacement relationships from this study to model the behaviour of a full-

scale BTF subjected to ground motions. These results could be verified by subjecting a full scale or scaled down BTF with SMA dowel connections to ground motions on a shake table.

- Development and experimental testing of a connection detail that minimizes shear forces in the SMA. The use of SMAs in tension would be highly favorable to fully utilize the self-centering ability of the material and limit the possibility of sudden shear failures.

Bibliography

Abaqus. (2009). *Abaqus Theory Manual.* Version 6.6. Retrieved from: https://classes.engineering.wustl.edu/2009/spring/mase5513/abaqus/docs/v6.6/books/usb/default.htm

Abaqus. (2017). *Abaqus Documentation.* Retrieved from: https://abaqus-docs.mit.edu/2017/English/SIMACAEEXCRefMap/simaexc-c-docproc.htm

Alam, M.S., Youssef, M.A., & Nehdi, M.L. (2010). Exploratory investigation on mechanical anchors for connecting SMA bars to steel or FRP bars. *Materials and Structures 43*: 91-107. https://doi-org.proxy.lib.uwaterloo.ca/10.1617/s11527-010-9601-0

ASTM. (1997). Standard Test Method for Evaluating Dowel-Bearing Strength of Wood and Wood-Based Products. ASTMD5764-97a (Reapproved 2018), West Conshohocken, PA: ASTM.

ASTM. (2016). Standard Test Method for Direct Moisture Content Measurement of Wood and Wood-Based Materials. ASTMD4442-16, West Conshohocken, PA: ASTM.

ASTM. (2017a). Standard Test Method for Density and Specific Gravity (Relative Density) of Wood and Wood-Based Materials. ASTMD2395-17, West Conshohocken, PA: ASTM.

ASTM. (2017b). Standard Test Method for Determining Bending Yield Moment of Nails. ASTMF1575-17, West Conshohocken, PA: ASTM.

ASTM. (2019). Standard Test Methods for Cyclic (Reversed) Load Test for Shear Resistance of Vertical Elements of the Lateral Force Resisting Systems for Buildings. ASTME2126-19, West Conshohocken, PA: ASTM.

Auricchio, F., Taylor, R.L., and Lubliner, J. (1997). Shape-Memory Alloys: macromodelling and numerical simulations of the superelastic behaviour. Computer Methods in Applied Mechanics and Engineering, vol. 146, pp. 281–312.

Blomgren, H.E., Koppits, J-P., Valdes, A.D., & Ko, E. (2016). *The Heavy Timber Buckling-Restrained Braced Frame as a Solution for Commercial Buildings in Regions of High Seismicity.* World Conference Timber Engineering, Vienna, Austria.

Bruneau, M., Chang, S.E., Eguchi, R.T., Lee, G.C., O'Rourke, T.D., Reinhorn, A.M., Shinozuka, M., Tierney, K., Wallace, W.A., & von Winterfeldt, D. (2003). A Framework to Quantitatively Assess and Enhance the Seismic Resilience of Communities. *Earthquake Spectra, 19(4):* 733-752. https://doi.org/10.1193%2F1.1623497

Bruneau, M., & Reinhorn, A. (2007). Exploring the Concept of Seismic Resilience for Acute Care Facilities. *Earthquake Spectra, 23(1):* 41-62. http://dx.doi.org/10.1193/1.2431396

Canadian Commission on Building and Fire Codes, & National Research Council of Canada. (2015). *National Building Code of Canada.* Ottawa, ON: The Council.

Canadian Standards Association. (2019). *Engineering Design in Wood* (CSA Standard No. 086:19). Mississauga, ON: CSA Group.

Canadian Wood Council, & Canadian Standards Association. (2017). *Wood Design Manual*. Ottawa, ON: Canadian Wood Council.

Chan, N., Hashemi, A., Zamani, P., & Quenneville, P. (2021). Pinching-Free Connector for Timber Structures. *J. Struct. Eng., 147(5):* 04021036. https://doi.org/10.1061/(ASCE)ST.1943-541X.0002982

Chancellor, N.B., Eatherton, M.R., Roke, D.A., & Akbas, T. (2014). Self-Centering Seismic Lateral Force Resisting Systems: High Performance Structures for the City of Tomorrow. *Buildings, 4*: 520-548. doi:10.3390/buildings4030520

Chen, Z., & Popovski, M. (2020). *Expanding Wood Use Towards 2025: Seismic Performance of Braced Mass Timber Frames – Year 2.* Project No. 301013618. Vancouver, BC: FPInnovations.

Christopoulos, C., Tremblay, R., Kim, H-J., & Lacerte, M. (2008). Self-Centering Energy Dissipative Bracing System for the Seismic Resistance of Structures: Development and Validation. *Journal of Structural Engineering, 134(1): 96-107.* DOI: 10.1061/(ASCE)0733-9445(2008)134:1(96)

Croci, G. (2001). Strengthening the basilica of St Francis of Assisi after the September 1997 Earthquake. *Struct Eng Int. 11(3)*: 207-210. https://doi-org.proxy.lib.uwaterloo.ca/10.2749/101686601780346869

Dassault Systemes. (2020). Abaqus\CAE. Retrieved from: https://www.3ds.com/products-services/simulia/products/abaqus/abaquscae/

Di Cesare, A., Ponzo, F.C., Lamarucciola, N., & Nigro, D. (2020). Experimental seismic response of a resilient 3-storey post-tensioned timber framed building with dissipative braces. *Bulletin of Earthquake Engineering, 18:* 6825-6848. https://doi.org/10.1007/s10518-020-00969-y

Earthquake Engineering Research Institute. (2010, June). Learning from Earthquakes: The Mw 8.8 Chile Earthquake of February 27, 2010. *EERI Special Earthquake Report.* Retrieved from https://www.eeri.org/site/images/eeri_newsletter/2010_pdf/Chile10_insert.pdf

Equilibrium Consulting. (2013). *University of British Columbia Earth Sciences Building Chevron BTF* [Photograph]. Construction Canada. https://www.constructioncanada.net/building-the-earth-sciences-building-at-the-university-of-british-columbia/

Fang, C., Yam, C-M., Ma, H., & Chung, K-F. (2015). Tests on superelastic Ni-Ti SMA bars under cyclic tension and direct shear: towards practical recentring connections. *Materials and Structures, 48*: 1013-1030. https://doi.org/10.1617/s11527-013-0212-4

Farsangi, E.N., Yang, T.Y., Gardoni, P., Takewaki, I, & Astaneh-Asl, A (Ed.). (2019). *Resilient Structures and Infrastructure.* Springer Nature Singapore Pte Ltd. https://doi.org/10.1007/978-981-13-7446-3

Ganey, R., Berman, J., Akbas, T., Loftus, S., Dolan, J.D., Sause, R., Ricles, J., Pei, S., van de Lindt, J., & Blomgren, H-E. (2017). Experimental investigation of self-centering cross-laminated timber walls. *J. Struct. Eng., 143(10):* 04017135. https://doi.org/10.1061/(ASCE)ST.1943-541X.0001877

Gao, N., Jeon, J-S., Hodgson, D.E., & DesRoches, R. (2016). An innovative seismic bracing system based on a superelastic shape memory alloy ring. *Smart Mater. Struct., 25(5),* 055030. doi:10.1088/0964-1726/25/5/055030

Granello, G., Palermo, A., Pampanin, S., Pei, S., & van de Lindt, J. (2020). Pres-Lam Buildings: State-of-the-Art. *J.Struct.Eng., 146(6):* 04020085. https://doi.org/10.1061/(ASCE)ST.1943-541X.0002603

Hashemi, A., Zarnani, P., Masoudnia, R., & Quenneville, P. (2017a). Seismic resistant rocking coupled walls with innovative Resilient Slip Friction (RSF) joints. *Journal of Constructional Steel Research, 129,* 215-226. http://dx.doi.org/10.1016/j.jcsr.2016.11.016

Hashemi, A., Zarnani, P., Masoudnia, R., & Quenneville, P. (2017b). Experimental testing of rocking Cross Laminated Timber (CLT) walls with Resilient Slip Friction (RSF) joints. *J. Struct. Eng., 144(1),* 04017180. https://doi.org/10.1061/(ASCE)ST.1943-541X.0001931

Hashemi, A., Zarnani, P., Darani, M., Valadbeigi, A., Clifton, C., & Quenneville, P. (2018). Damage Avoidance Self-Centering Steel Moment Resisting Frames (MRFs) Using Innovative Resilient Slip Friction Joints (RSFJs). *Key Engineering Materials, 763,* 726-734.

Hashemi, A., Yousef-Beik, S.M.M., Bagheri, H., Darani, F.M., Zarnani, P., & Quenneville, P. (2019). *Resilient Slip Friction Joint (RSFJ): A damage avoidance technology for seismic-proofing new and existing buildings.* 12th Canadian Conference on Earthquake Engineering, Quebec City, Canada. https://www.caee.ca/12CCEEpdf/192-ZJx1-278.pdf

Himes, A., & Busby, G. (2020). Wood buildings as a climate solution. *Developments in the Built Environment, 4(2020),* 100030. https://doi.org/10.1016/j.dibe.2020.100030

Ho, T.X., Dao, T.N., Aaleti, S., van de Lindt, J.W., & Rammer, D.R. (2016). Hybrid system of unbonded post-tensioned CLT panels and light-frame wood shear walls. *J. Struct. Eng. 143(2):* 04016171. https://doi.org/10.1061/(ASCE)ST.1943-541X.0001665

Hong, J.P. (2007). *Three-Dimensional Nonlinear Finite Element Model for Single and Multiple Dowel-Type Wood Connections*. [PhD Thesis, University of British Columbia]. DSpace. https://dx.doi.org/10.14288/1.0066597

Huang, H., & Chang, H-S. (2017). Seismic resilience timber connection – adoption of shape memory alloy tubes as dowels. *Struct Control Health Monit., 24(10).* https://doi.org/10.1002/stc.1980

Huang, H., Chang, H-S., & Chen, K. (2019). *Study of SMA-dowelled timber connection reinforced by densified veneer wood under cyclic loading*. International Conference on Advances in Civil Engineering and Materials and World Symposium on Sustainable Bio-Composite Materials and Structures, Nanjing, China. https://doi.org/10.1051/matecconf/201927501015

Huang, H., Zhu, Y-Z., & Chang, W-S. (2020). Comparison of Bending Fatigue of NiTi and CuAlMn Shape Memory Alloy Bars. *Advances in Materials Science and Engineering, 2020,* 8024803. https://doi.org/10.1155/2020/8024803

Indirli, M., Castellano, M., Clemente, P., & Martelli, A. (2001). *Demo-application of shape memory alloy devices: the rehabilitation of the S. Giorgio Church bell tower*. 8th International Symposium on Smart Structures and Materials, Newport Beach, USA. https://doi-org.proxy.lib.uwaterloo.ca/10.1117/12.434126

Iqbal, A., Fragiacomo, M., Pampanin, S., & Buchanan, H. (2017). Seismic resilience of plywood-coupled LVL wall panels. *Eng. Struct., 167:* 750-759. https://doi.org/10.1016/j.engstruct.2017.09.053

Iqbal, A., Pampanin, S., Palermo, A., Buchanan, H. (2015). Performance and design of LVL walls coupled with UFP dissipaters. *J. Earthquake Eng., 19(3):* 383-409. https://doi.org/10.1080/13632469.2014.987406

Johansen, K.W. (1949). Theory of Timber Connections. Publications *of the International Association of Bridge and Structural Engineering.* No.9: 249-262. Bern, General Secretariat.

Jorissen, A. (1998). *Double Shear Timber Connections With Dowel Type Fasteners* [Doctoral dissertation, Delft University of Technology]. Delft University Institutional Repository. http://resolver.tudelft.nl/uuid:acadc994-803a-4ab3-85ff-32ea1947837b

Karacabeyli, E., and Gagnon, S. (Ed.). (2019). *Canadian CLT Handbook – Volume 1*. Pointe Claire, QC: FPInnovations.

Karagiannis, V., Malaga-Chuquitaype, C., & Elghazouli, A.Y. (2016). Modified foundation modelling of dowel embedment in glulam connections. *Construction and Building Materials, 102:* 1168-1179. http://dx.doi.org/10.1016/j.conbuildmat.2015.09.021

Kim, H-J., and Christopoulos, C. (2008). Seismic design procedure and seismic response of post-tensioned self-centering steel frames. *Earthquake Engng Struct. Dyn., 38:* 355-376. DOI: 10.1002/eqe.859

Kurdyumov, G.V., & Khandros, L.G. (1949). First reports of the thermoelastic behaviour of the martensitic phase of Au-Cd alloys. *Dokl. Akad. Nauk SSSR 66*, No.2: 211-214.

Lagoudas, D.C (Ed.). (2008). *Shape Memory Alloys – Modelling and Engineering Applications*. Springer Science+Business Media, LLC.

Lecce, L., & Concilio, A (Ed.). (2015). *Shape Memory Alloy Engineering*. Elsevier Ltd.

Ma, H., Wilkinson, T., & Cho, C. (2007). Feasibility study on a self-centering beam-to-column connection by using the superelastic behavior of SMAs. *Smart Mater. Struct., 16(2007):* 1555-1563. doi:10.1088/0964-1726/16/5/008

Miller, D.J., Fahnestock, L.A., & Eatherton, M.R. (2012). Development and experimental validation of nickel-titanium shape memory alloy self-centering buckling restrained brace. *Eng Struct, 40(2012):* 288-298. https://doi.org/10.1016/j.engstruct.2012.02.037

Miller, S., Woods, J.E., Erochko, J., Lau, D.T., & Gilbert, C.F. (2020). Experimental and analytical fragility assessment of a combined heavy timber-steel-braced frame through hybrid simulation. *Earthquake Engng Struct Dyn.,* 2021;50:270-289. https://doi.org/10.1002/eqe.3329

Newcombe, M.P., Pampanin, S., & Buchanan, A.H. (2010). *Global Response of a Two Storey Pres-Lam Timber Building.* New Zealand Society for Earthquake Engineering Conference, Wellington, New Zealand. https://www.nzsee.org.nz/db/2010/Paper28.pdf

Nikoukalam, M.T., & Dolatshahi, K.M. (2015). Development of structural shear fuse in moment resisting frames. *Journal of Constructional Steel Research, 114(2015)*: 349-361. http://dx.doi.org/10.1016/j.jcsr.2015.08.008

O'Callaghan, R. (2021). *Effects of GFRP Reinforcement on the Compressive Behaviour of Square SPF Timber Columns.* [Master's Thesis, University of Waterloo]. UWSpace. http://hdl.handle.net/10012/17479

Oliveira, D. (2021). *Modeling of Mass Timber Components Subjected to Blast Loads.* [Master's Thesis, University of Ottawa. uO Research. http://dx.doi.org/10.20381/ruor-26843

Omori, T., Ando, K., Okano, M., Xu, X., Tanaka, Y., Ohnuma, I., Kainuma, R., & Ishida, K. (2011, July 1). Superelastic Effect in Polycrystalline Ferrous Alloys. *Science Magazine, 333*(6038), 68-71.

Omori, T., Kusama, T., Kawata, S., Ohnuma, I., Sutou, Y., Araki, Y., Ishida, K., & Kainuma, R. (2013, September 27). Abnormal Grain Growth Induced by Cyclic Heat Treatment. *Science Magazine, 341*(6153), 1500-1502.

Oudjene, M., & Khelifa, M. (2010). *Experimental and Numerical Analyses of Single Double Shear Dowel-Type Timber Joints*. World Conference Timber Engineering, Trentino, Italy. http://www.scopus.com/inward/record.url?eid=2-s2.0-84870620015&partnerID=MN8TOARS

Palermo, A., Pampanin, S., Buchanan, A., & Newcombe, M. (2005). *Seismic Design of Multi-Storey Buildings using Laminated Veneer Lumber (LVL).* New Zealand society for earthquake engineering conference, Wairakei, New Zealand.

Paret, T.F., Freeman, S.A., Searer, G.R., Hachem, M., & Gilmartin, U.M. (2008). Using traditional and innovative approaches in the seismic evaluation and strengthening of a historic unreinforced masonry synagogue. *Eng Struct, 30(8)*: 325-332. http://dx.doi.org/10.1016/j.engstruct.2007.03.023

Pei, S., van de Lindt, J.W., Barbosa, A.R., Berman, J.W., McDonnell, E., Dolan, J.D., Blomgren, H-E., Zimmerman, R.B., Huang, D., & Wichman, S. (2019). Experimental Seismic Response of a Resilient 2-Story Mass-Timber Building with Post-Tensioned Rocking Walls. *J. Struct. Eng., 145(11):* 04019120. https://doi.org/10.1061/(ASCE)ST.1943-541X.0002382

Plesnik, T., Erochko, J., & Doudak, G. (2016). Nailed Connection Behavior in Light-Frame Wood Shear Walls with an Intermediate Later of Insulation. *Journal of Structural Engineering*, *142(7),* 04016045. http://dx.doi.org/10.1061/(ASCE)ST.1943-541X.0001506

Popovski, M., & Karacabeyli, E. (2008). *Force Modification Factors and Capacity Design Procedures for Braced Timber Frames.* 14th World Conference on Earthquake Engineering, Beijing, China. http://www.iitk.ac.in/nicee/wcee/article/14_S12-003.PDF

Qiu, C., & Zhu, S. (2017). Shake table test and numerical study of self-centering steel frame with SMA braces. *Earthquake Engng Struct. Dyn., 46(1):* 117-137. https://doi.org/10.1002/eqe.2777

Sarti, F., Palermo, A., & Pampanin, S. (2015). Development and testing of an alternative dissipative posttensioned rocking timber wall with boundary columns. *J. Struct. Eng. 142(4):* 4015005. https://doi.org/10.1061/(ASCE)ST.1943-541X.0001291

Schreyer, A.C. (2002). *Monotonic and Cyclic Behaviour of Slender Dowel-Type Fasteners in Wood-Steel-Wood Connections.* [Master's Thesis, University of British Columbia]. DSpace. https://open.library.ubc.ca/cIRcle/collections/ubctheses/831/items/1.0103844

Schreyer, A.C. (2017). *University of Massachusetts Olver Design Building* [Photograph]. Alex Schreyer. https://alexschreyer.net/photography/john-w-olver-design-building-2017/

Schwarze, R., Braun, M., Seim, W., Krooß, P., Vollmer, M., & Niendorf, T. (2021). Application and potential of shape memory alloys for dowel-type connections in timber structures. *Wood Material Science & Engineering.* https://doi.org/10.1080/17480272.2021.1920625

Smith, I. (1983). Coefficient of friction values applicable to contact surfaces between mild steel connectors such as bolts and dry European white wood. *J. Inst. Wood Sci., 9(1983):* 229-234.

Seo, J., Kim, Y.C., & Hu, J.W. (2015). Pilot Study for Investigating the Cyclic Behavior of Slit Damper Systems with Recentering SMA Bending Bars Used for Seismic Restrainers. *Appl. Sci., 5,* 187-208. https://doi.org/10.3390/app5030187

Vargas, R.E., Bruneau, M. (2006). *Analytical investigation of the structural fuse concept*. Technical Report MCEER-06-0004. Buffalo, New York: University at Buffalo, State University of New York.

Vargas, R.E., Bruneau, M. (2009). Analytical Response and Design of Buildings with Metallic Structural Fuses I. *Journal of Structural Engineering, 135(4)*: 386-393. https://doi.org/10.1061/(ASCE)0733-9445(2009)135:4(386)

Vollmer, M., Arold, T., Kriegel, M.J., Klemm, V., Degener, S., Freudenberger, J., & Niendorf, T. (2019). Promoting abnormal grain growth in Fe-based shape memory alloys through compositional adjustments. *Nature Communications, 10:2337.* https://doi.org/10.1038/s41467-019-10308-8

Vulovic, S., Zivkovic, M., Grujovic, N., & Slavkovic, R. (2007). A Comparative Study of Contact Problems Based on the Penalty and Lagrange Approaches. *Serbian Society for Computational Mechanics, 1(1):* 174-183.

Wang, B., Zhu, S., Chen, K., & Huang, J. (2020). Development of superelastic SMA angles as seismic-resistant self-centering devices. *Eng Struct, 218(2020),* 110836. https://doi.org/10.1016/j.engstruct.2020.110836

Wang, B., Zhu, S., & Casciati, F. (2020). Experimental Study of Novel Self-Centering Seismic Base Isolators Incorporating Superelastic Shape Memory Alloys. *Struct. Eng., 146(7).* https://doi-org.proxy.lib.uwaterloo.ca/10.1061/(ASCE)ST.1943-541X.0002679

Wriggers, P. (2006). *Computational Contact Mechanics.* Springer.

Yousef-Beik, S.M.M., Bagheri Mehdi Abadi, H., Zarnani, P., Hashemi, A., & Quenneville, P. (2019). *Damage-avoidance Timber Brace using a Self-centering Friction Damper.* Pacific Conference on Earthquake Engineering, Auckland, New Zealand. http://db.nzsee.org.nz/2019/Oral/4B.06%20Yousef-beik.pdf

Appendix A
Material Test Results

Bending Tests: Steel Specimens
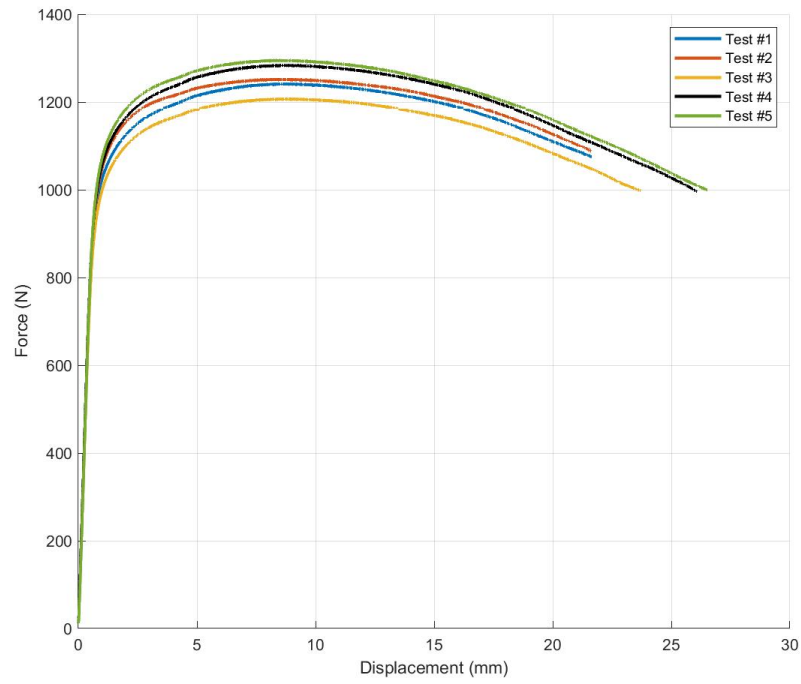
Figure A.1: Force-Displacement Relationship for all Steel Bolt Bending Tests

Bending Tests: SMA Specimens
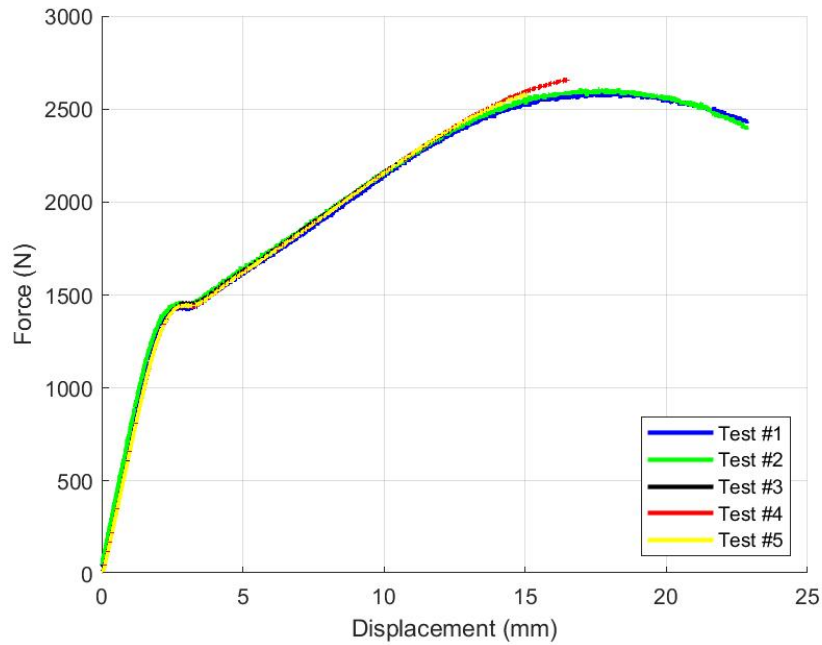
Figure A.2: Force-Displacement Relationship for all SMA Bar Bending Tests

Embedment Tests: Results and Specimen Information
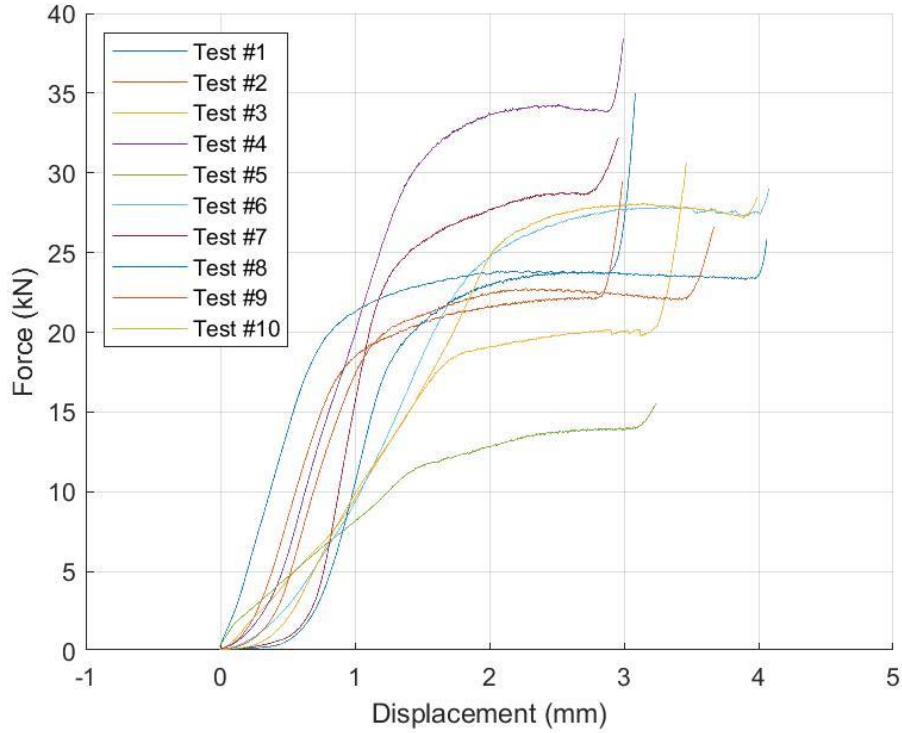
Figure A.3: Force-Displacement Relationships for all Embedment Tests

Table A.1: Specimen Details and Results for all Embedment Tests

Sample ID	Bearing Length (mm)	Yield Load (kN)	Yield Stress (MPa)
S1	128	21.7	26.7
S2	128	19.6	24.2
S3	127	19.1	23.7
S4	127.5	32.8	40.5
S5	93	12.7	21.6
S6	128	26.2	32.3
S7	128	25.1	30.9
S8	128	21.6	26.6
S9	127.5	20.8	25.7
S10	127	27.5	34.1

Appendix B

Connection Test Results

1SM1 [1 bolt, Steel, Monotonic, Test #1]: Used average of every 5 data points to smooth data.
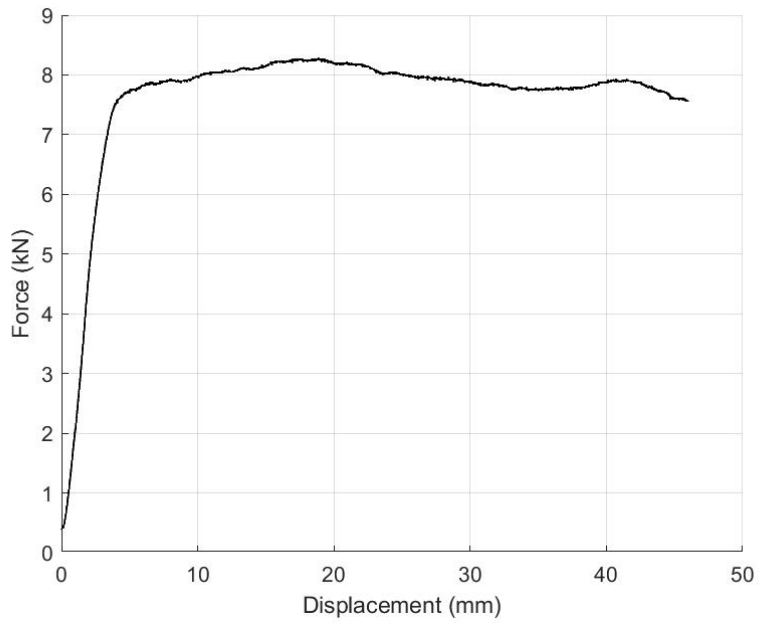
Figure B.1: Force-Displacement Relationship for Specimen 1SM1
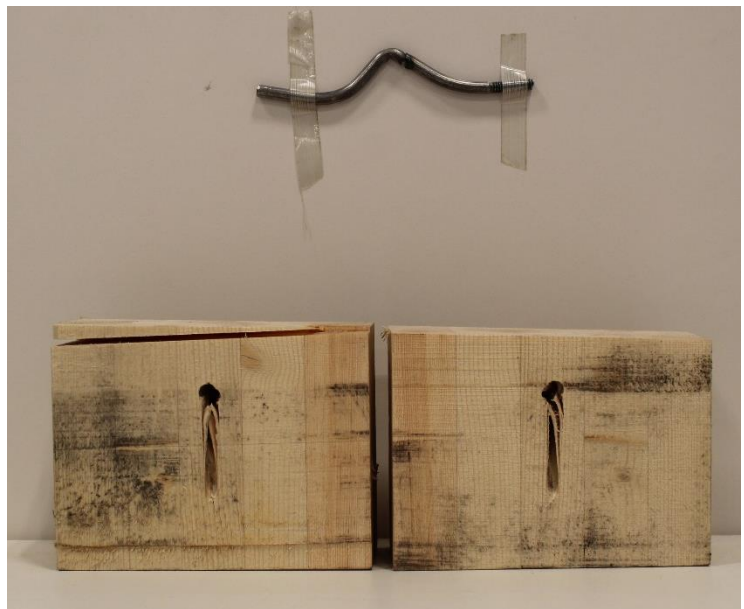
n/a	
a.) Wood Crushing	b.) Embedment and Bent Bar

Figure B.2: Pictures of Damage on Specimen 1SM1

1SM2 [1 bolt, Steel, Monotonic, Test #2]: Used average of every 25 data points to smooth data.
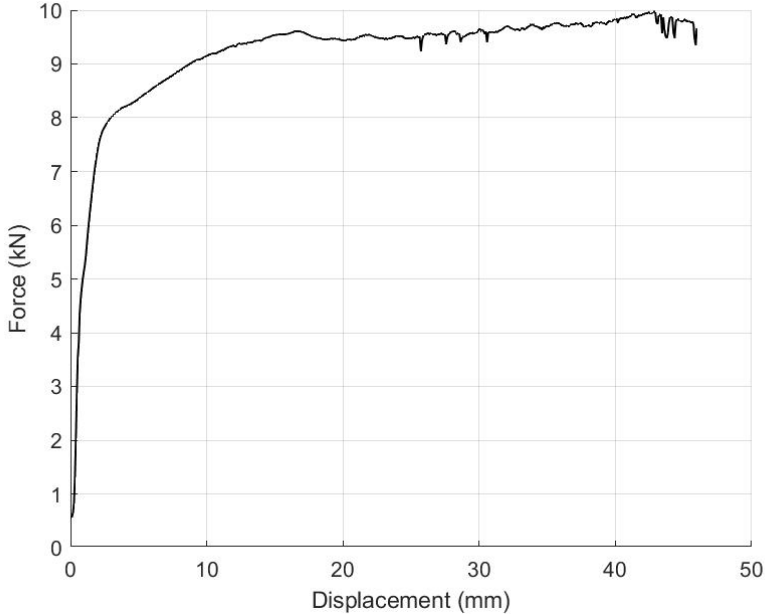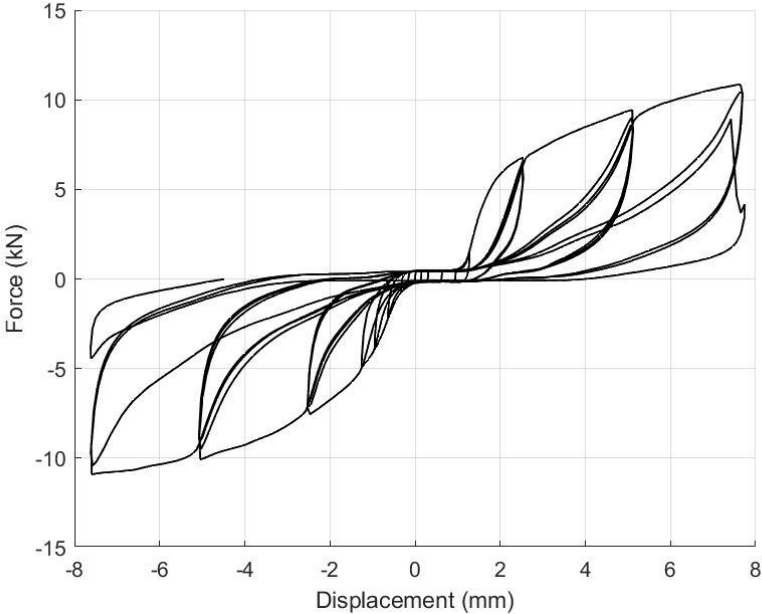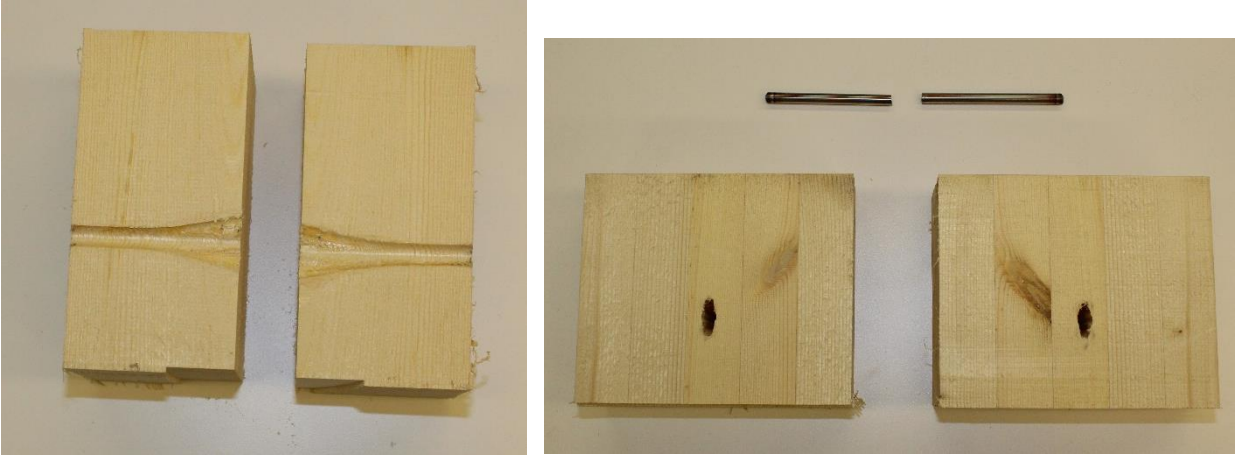

Figure B.3: Force-Displacement Relationship for Specimen 1SM2
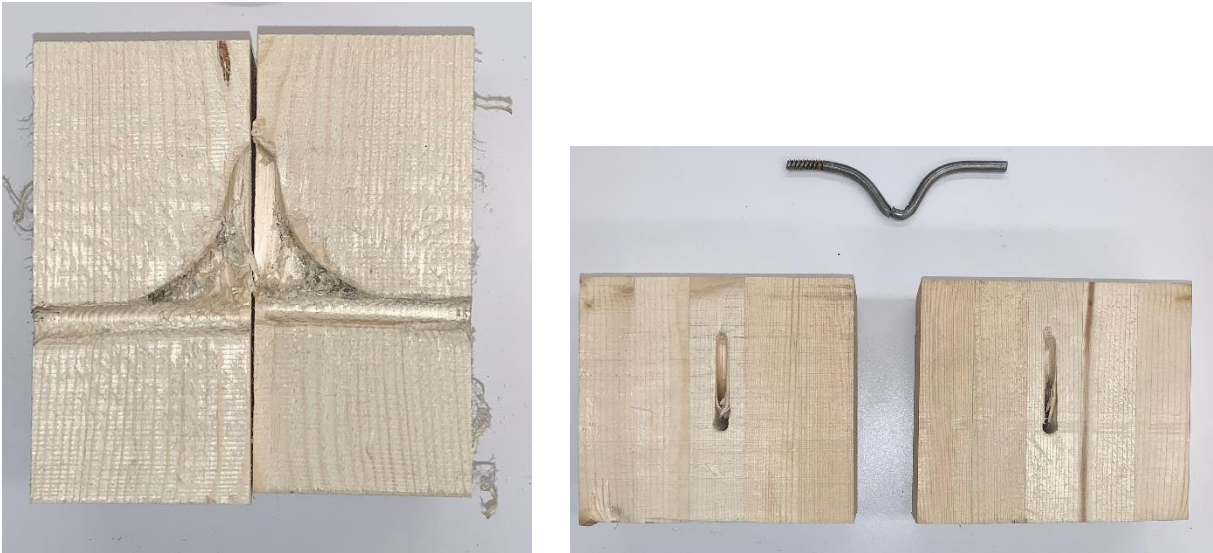
a.) Wood Crushing   b.) Embedment and Bent Bar

Figure B.4: Pictures of Damage on Specimen 1SM2

1SM3 [1 bolt, Steel, Monotonic, Test #3]: Used average of every 100 data points.
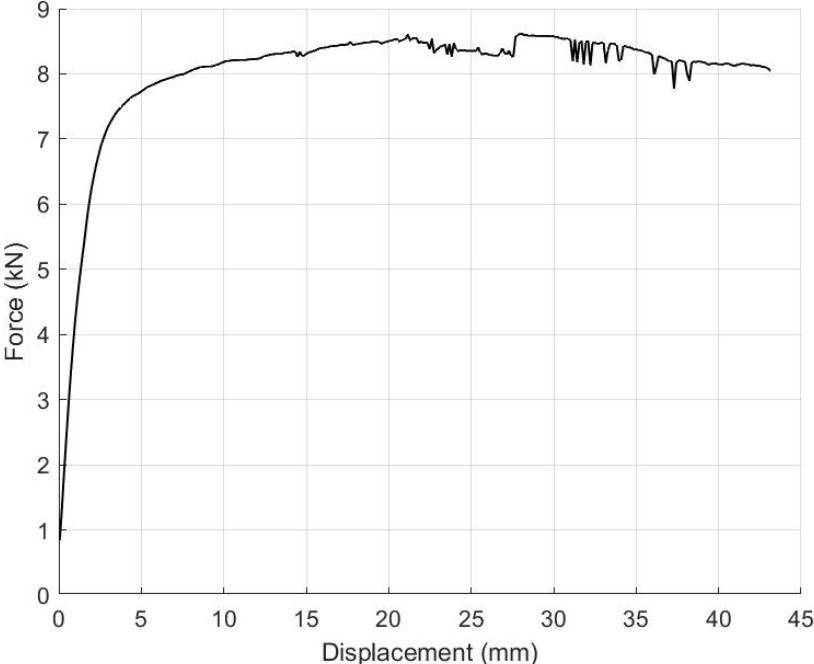
Figure B.5: Force-Displacement Relationship for Specimen 1SM3

n/a

a.) Wood Crushing and Bent Bar   b.) Embedment

Figure B.6: Pictures of Damage on Specimen 1SM3

1SC1 [1 bolt, Steel, Cyclic, Test #1]: Average of every 25 data points. Protocol: 12 mm max.
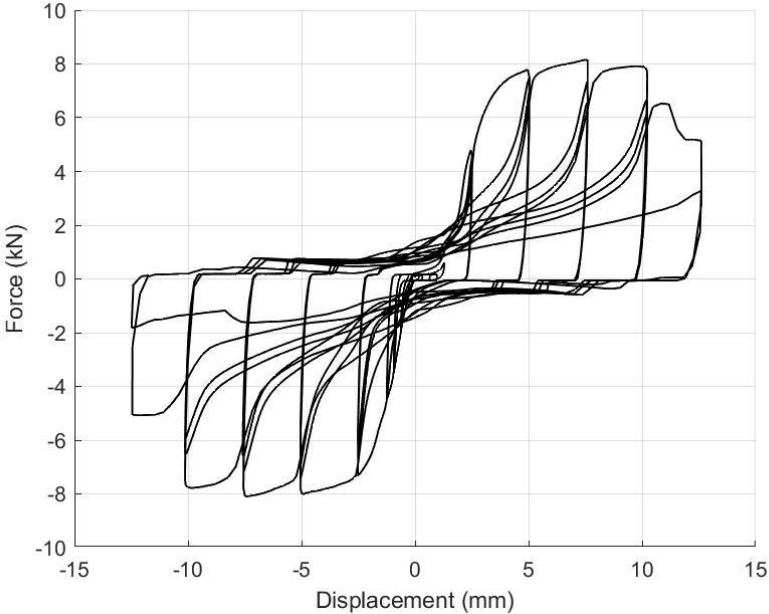
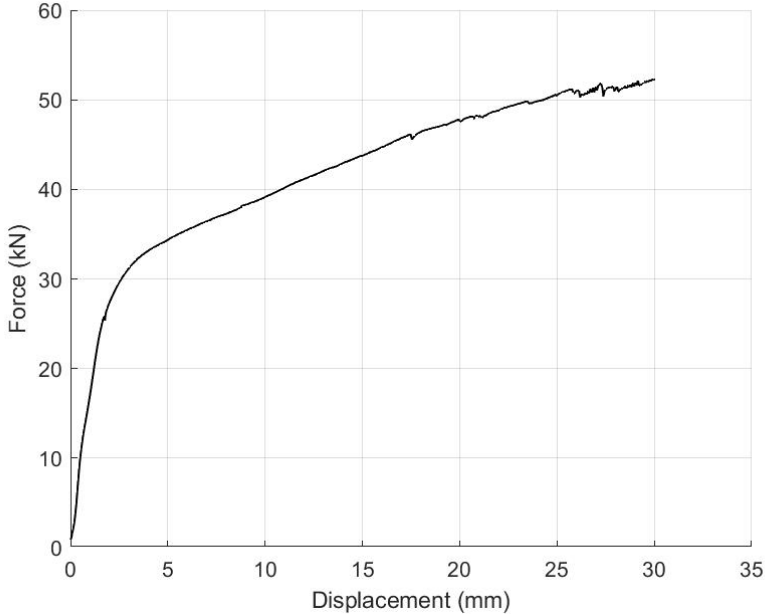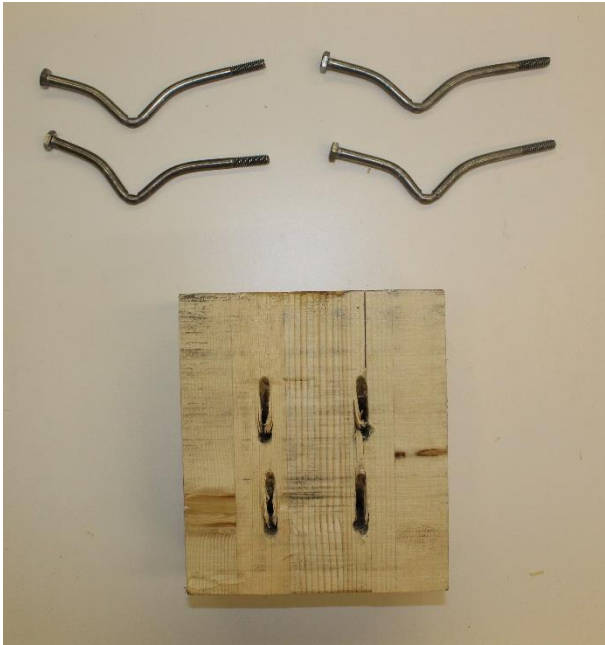**Figure B.7:** Force-Displacement Relationship for Specimen 1SC1
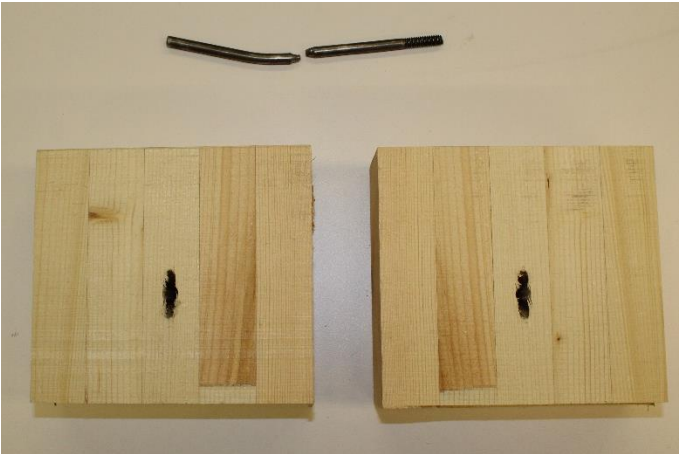
a.) Wood Crushing   b.) Embedment and Damaged Bar

Figure B.8: Pictures of Damage on Specimen 1SC1

1SC2 [1 bolt, Steel, Cyclic, Test #2]: Average of every 25 data points. Protocol: 12 mm max.
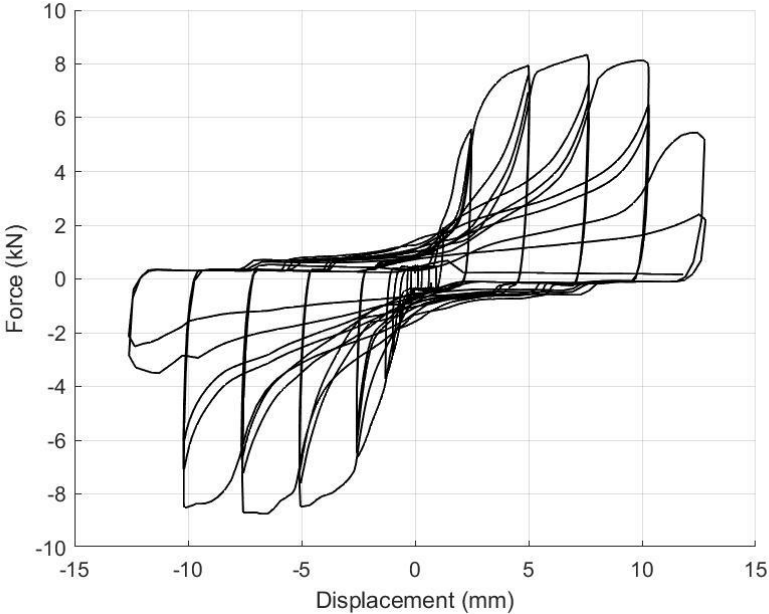
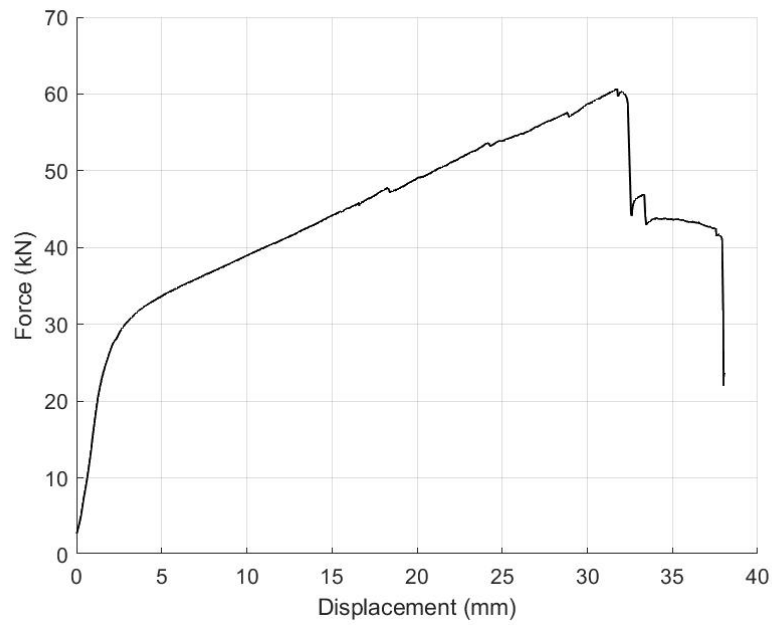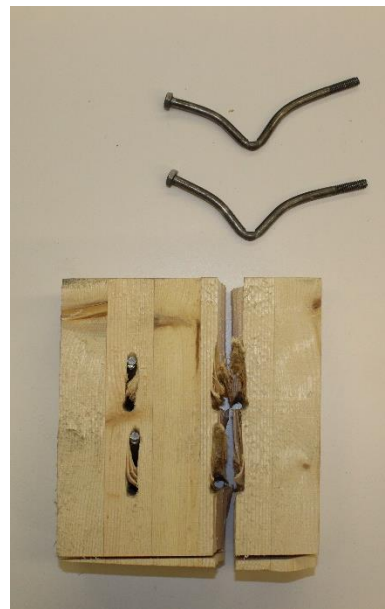**Figure B.9:** Force-Displacement Relationship for Specimen 1SC2
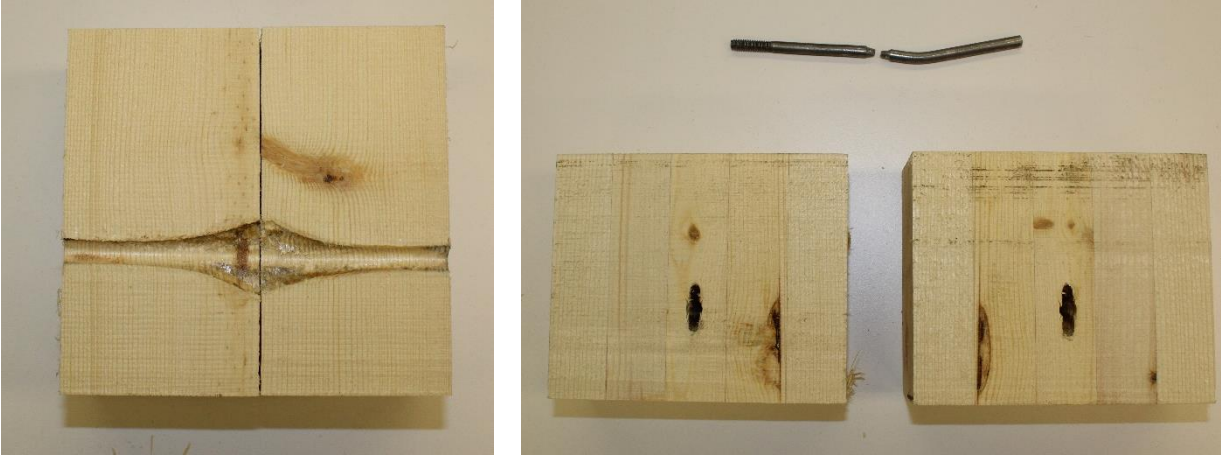
a.) Wood Crushing   b.) Embedment and Damaged Bar

Figure B.10: Pictures of Damage on Specimen 1SC2

1SC3 [1 bolt, Steel, Cyclic, Test #3]: Average of every 25 data points. Protocol: 12 mm max.

Figure B.11: Force-Displacement Relationship for Specimen 1SC3
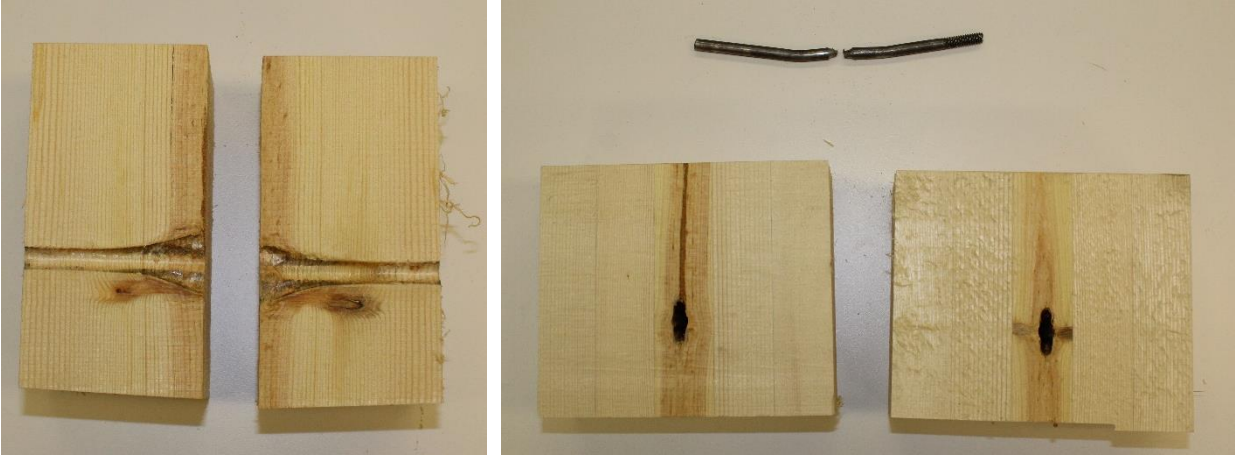
a.) Wood Crushing   b.) Embedment and Damaged Bar

Figure B.12: Pictures of Damage on Specimen 1SC3

1NM1 [1 bolt, Nitinol, Monotonic, Test #1]: Used average of every 50 data points.
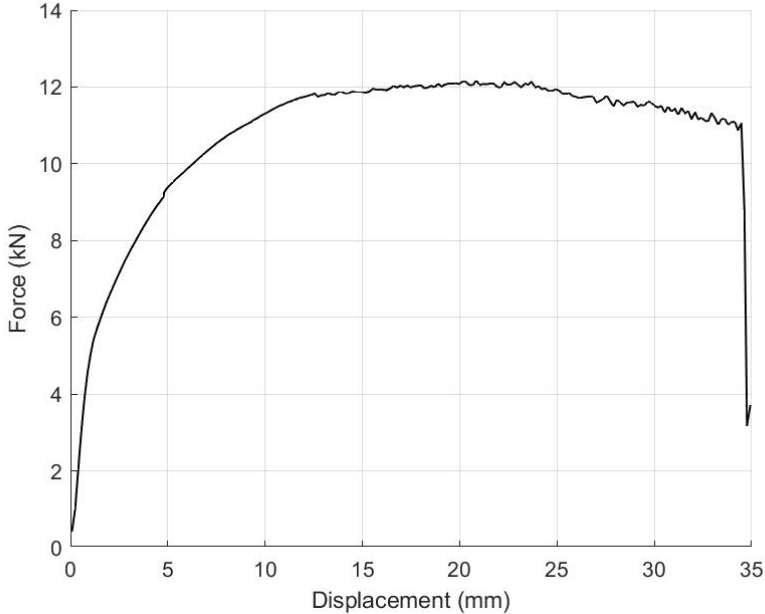
Figure B.13: Force-Displacement Relationship for Specimen 1NM1

a.) Wood Crushing   b.) Embedment and Damaged Bar

Figure B.14: Pictures of Damage on Specimen 1NM1

1NM2 [1 bolt, Nitinol, Monotonic, Test #2]: Used average of every 100 data points.
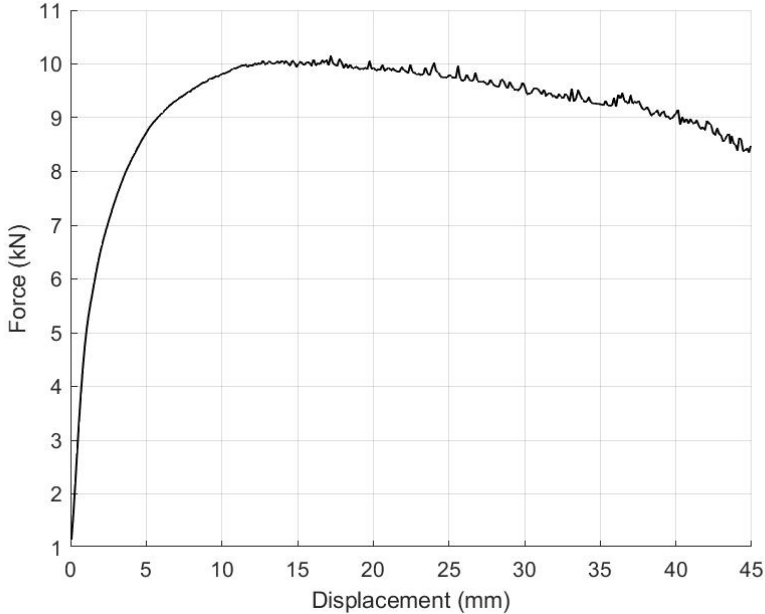
Figure B.15: Force-Displacement Relationship for Specimen 1NM2

                    n/a
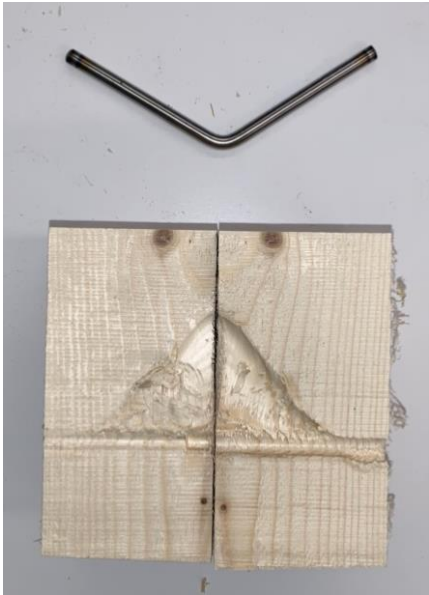
a.) Wood Crushing and Damaged Bar   b.) Embedment and Damaged Bar

Figure B.16: Pictures of Damage on Specimen 1NM2

1NM3 [1 bolt, Nitinol, Monotonic, Test #3]: Used average of every 100 data points.
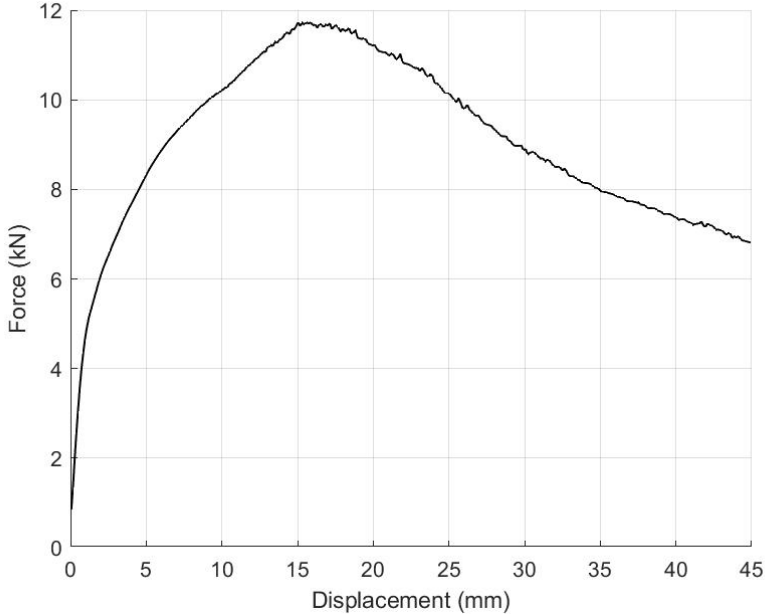
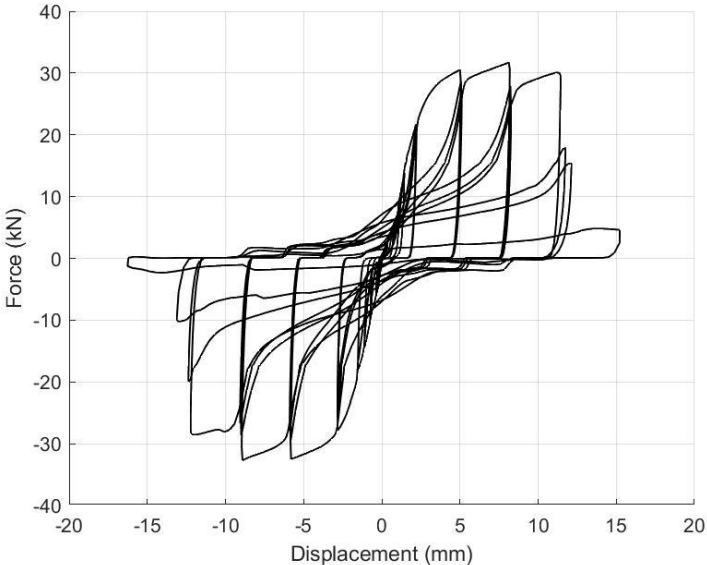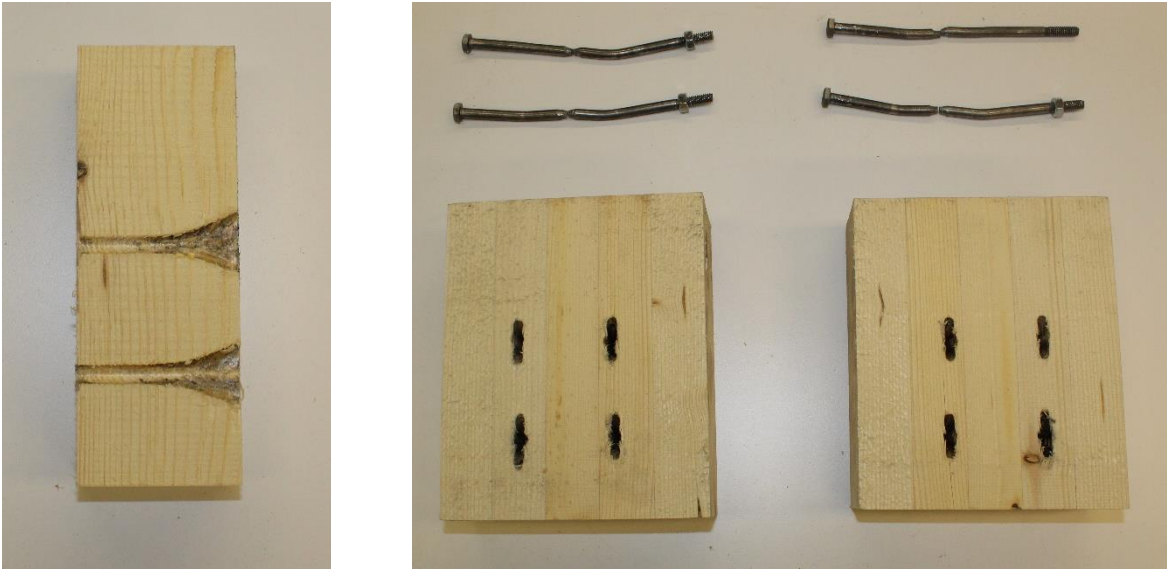**Figure B.17:** Force-Displacement Relationship for Specimen 1NM3
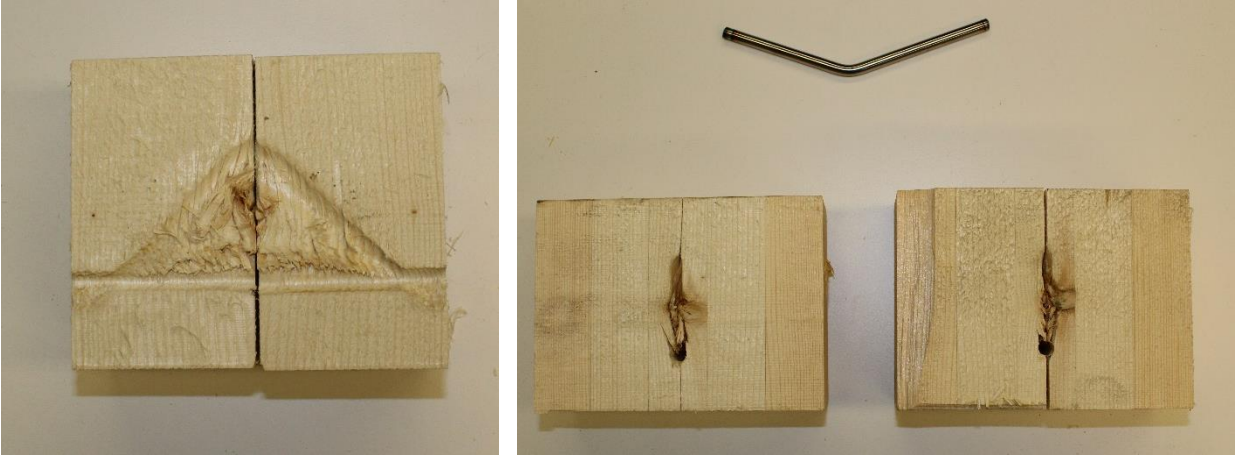
a.) Wood Crushing   b.) Embedment and Damaged Bar

Figure B.18: Pictures of Damage on Specimen 1NM3

1NC1 [1 bolt, Nitinol, Cyclic, Test #1]: Average of every 25 data points. Protocol: 12 mm max.
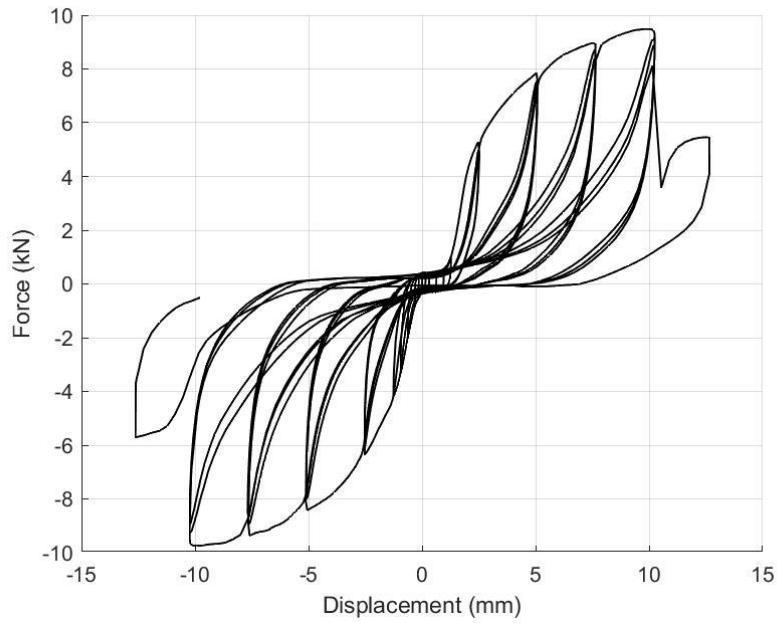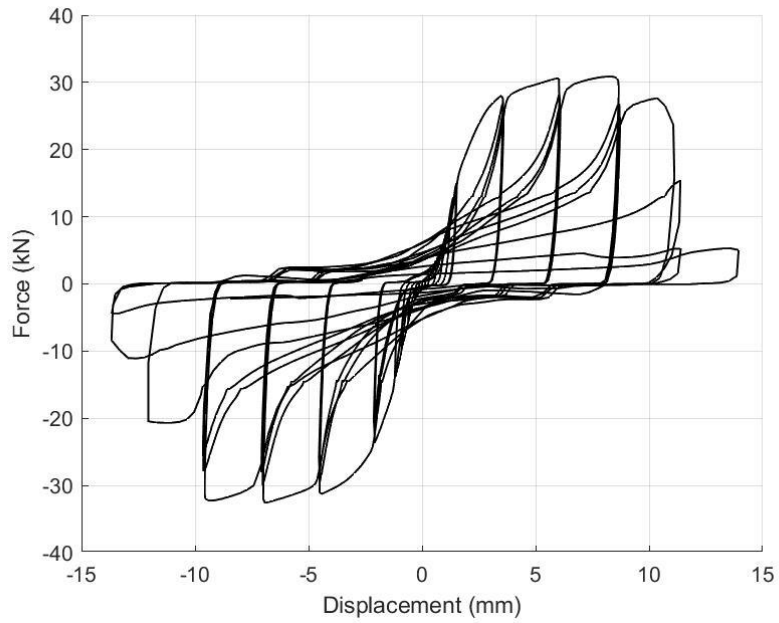

Figure B.19: Force-Displacement Relationship for Specimen 1NC1
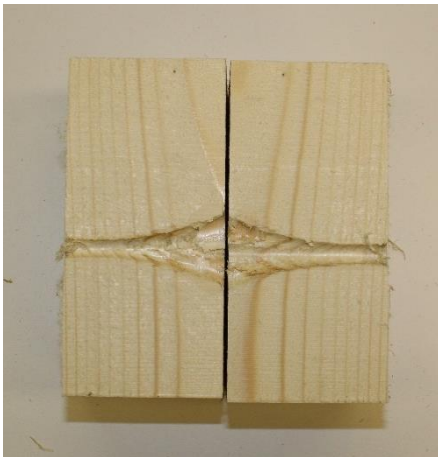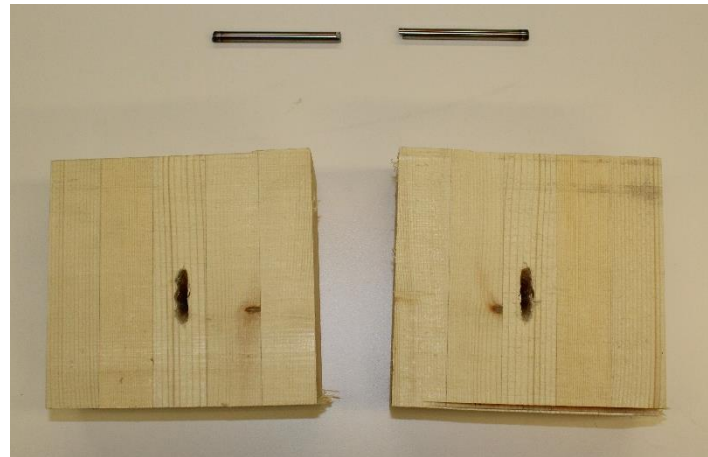
a.) Wood Crushing   b.) Embedment and Damaged Bar

Figure B.20: Pictures of Damage on Specimen 1NC1

1NC2 [1 bolt, Nitinol, Cyclic, Test #2]: Average of every 25 data points. Protocol: 12 mm max.
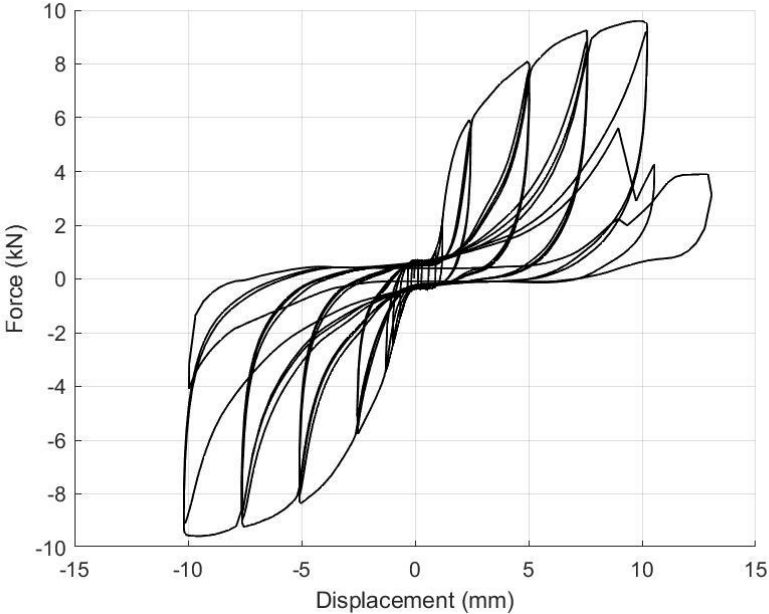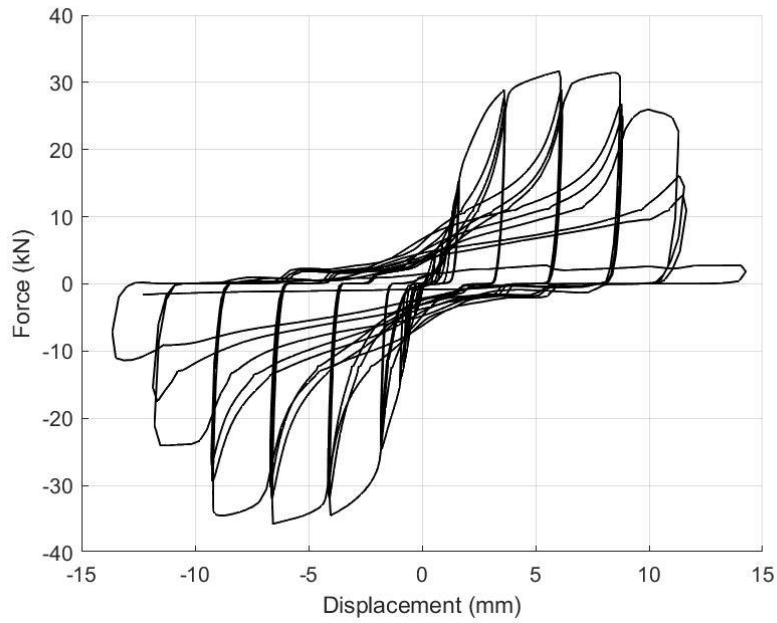

Figure B.21: Force-Displacement Relationship for Specimen 1NC2
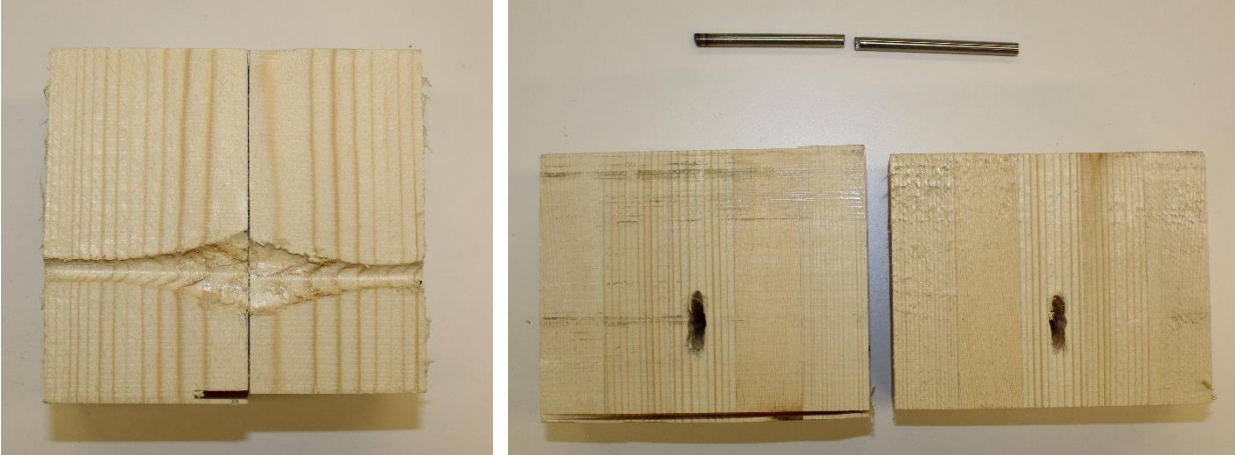
a.) Wood Crushing   b.) Embedment and Damaged Bar

Figure B.22: Pictures of Damage on Specimen 1NC2

1NC3 [1 bolt, Nitinol, Cyclic, Test #3]: Average of every 25 data points. Protocol: 12 mm max.
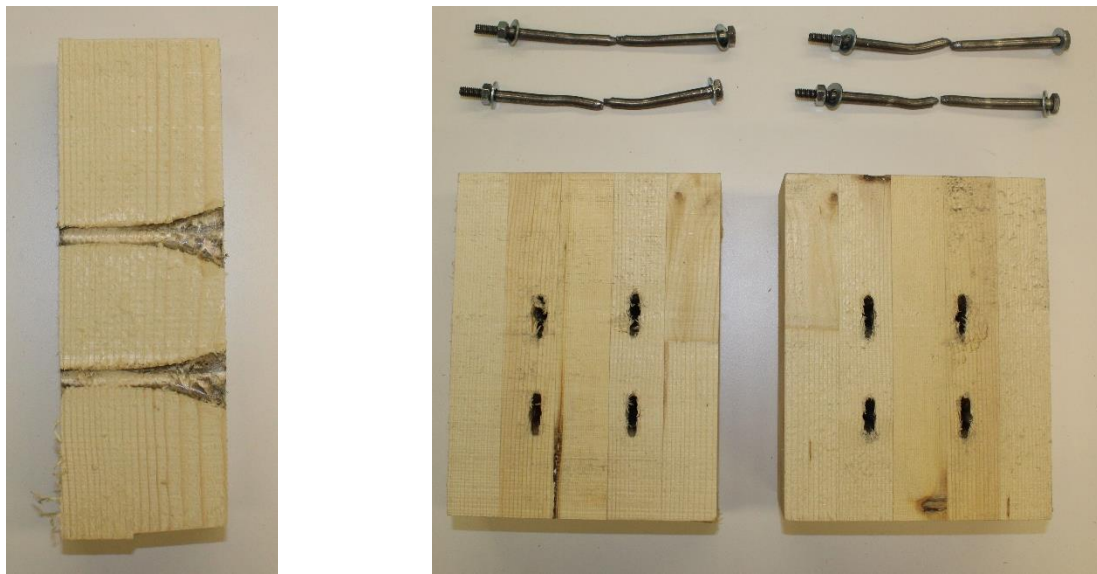

Figure B.23: Force-Displacement Relationship for Specimen 1NC3

a.) Wood Crushing   b.) Embedment and Damaged Bar

Figure B.24: Pictures of Damage on Specimen 1NC3

4SM1 [4 bolts, Steel, Monotonic, Test #1]: Average of every 50 data points.

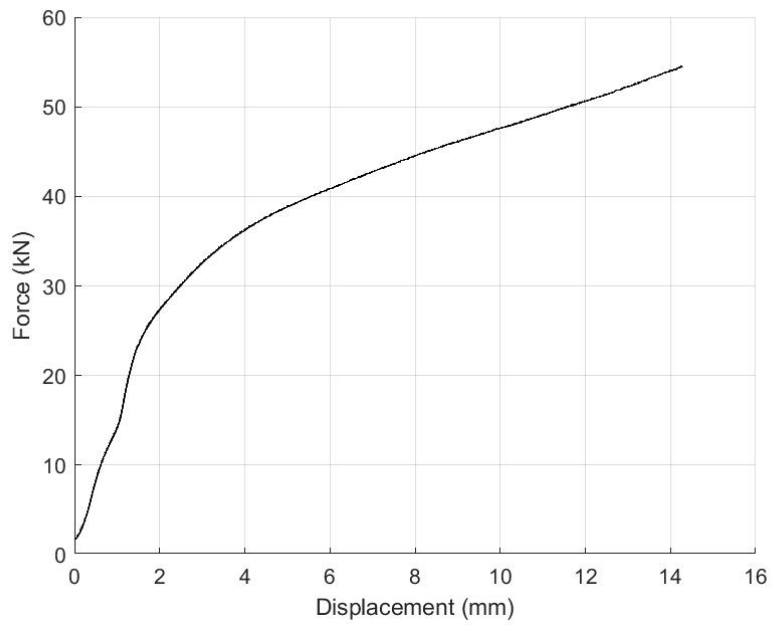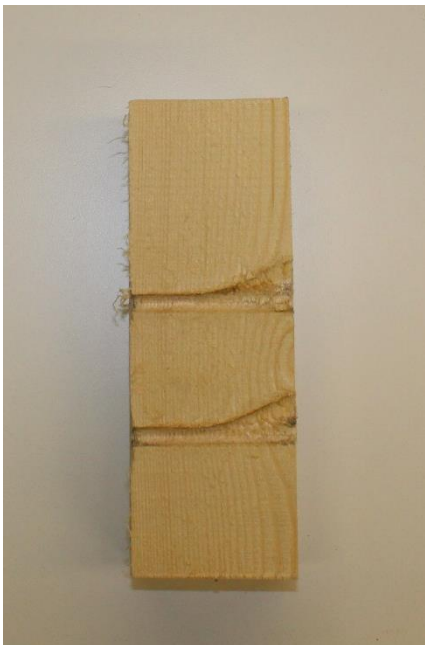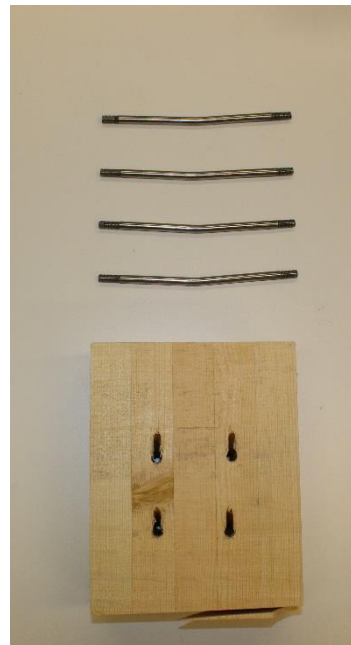

Figure B.25: Force-Displacement Relationship for Specimen 4SM1

a.) Wood Crushing   b.) Embedment and Bent Bolts

Figure B.26: Pictures of Damage on Specimen 4SM1

4SM2 [4 bolts, Steel, Monotonic, Test #2]: Used average of every 25 data points.

Figure B.27: Force-Displacement Relationship for Specimen 4SM2

a.) Wood Crushing

b.) Wood Embedment and Crack, and Damaged Bolts

Figure B.28: Pictures of Damage on Specimen 4SM2

4SM3 [4 bolts, Steel, Monotonic, Test #3]: Used average of every 25 data points.
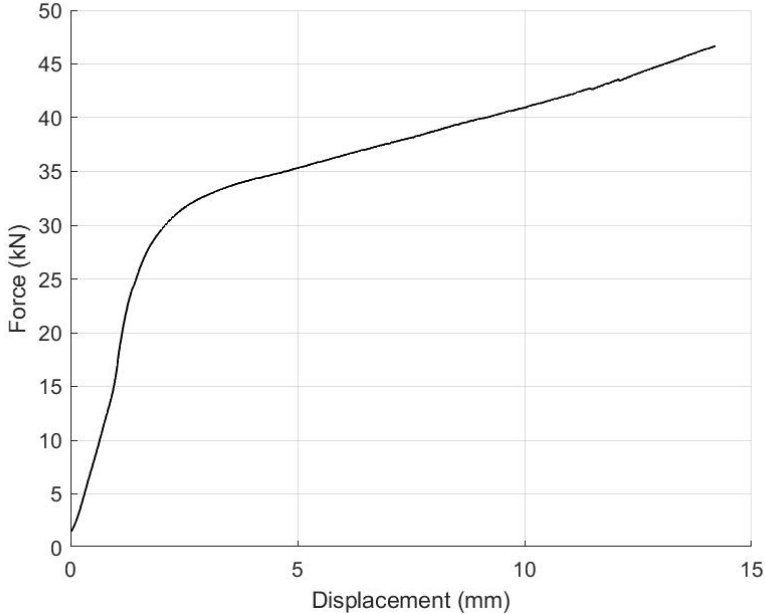
Figure B.29: Force-Displacement Relationship for Specimen 4SM3
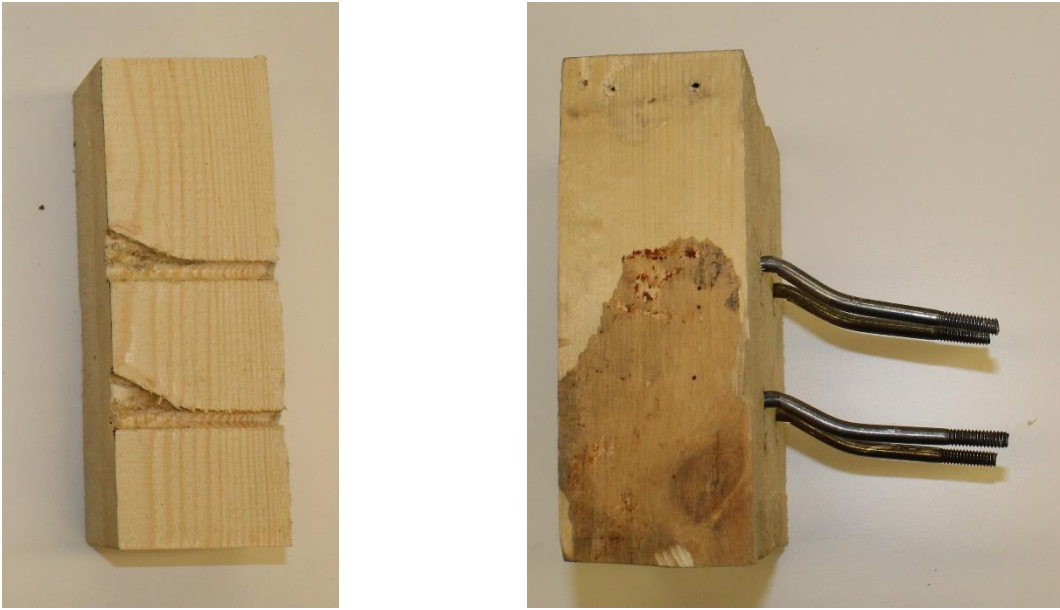
a.) Wood Crushing   b.) Picture of Bent Bolts

Figure B.30: Pictures of Damage on Specimen 4SM3

4SC1 [4 bolts, Steel, Cyclic, Test #1]: Average of every 25 data points.
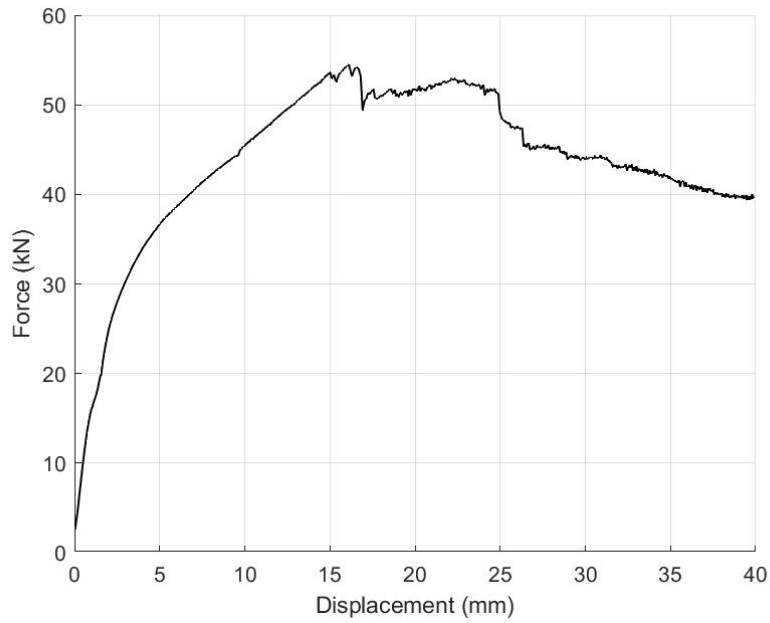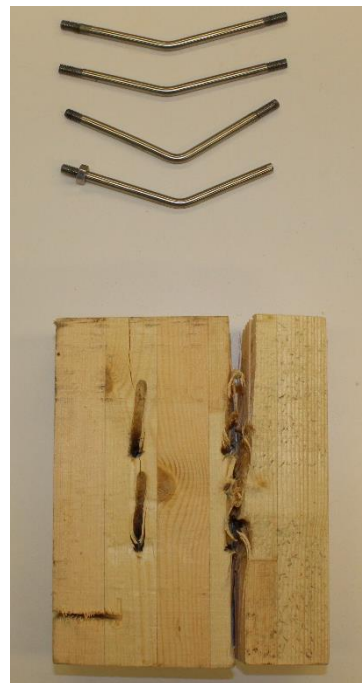

Figure B.31: Force-Displacement Relationship for Specimen 4SC1

a.) Wood Crushing   b.) Embedment and Damaged Bolts

Figure B.32: Pictures of Damage on Specimen 4SC1

4SC2 [4 bolts, Steel, Cyclic, Test #2]: Average of every 25 data points.

Figure B.33: Force-Displacement Relationship for Specimen 4SC2

a.) Wood Crushing   b.) Embedment and Damaged Bolts

Figure B.34: Pictures of Damage on Specimen 4SC2

4SC3 [4 bolts, Steel, Cyclic, Test #3]: Average of every 25 data points.
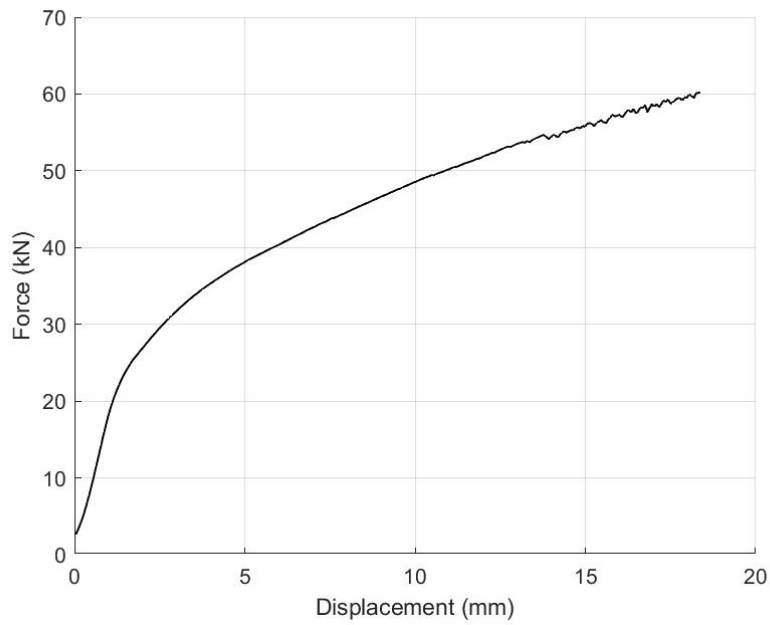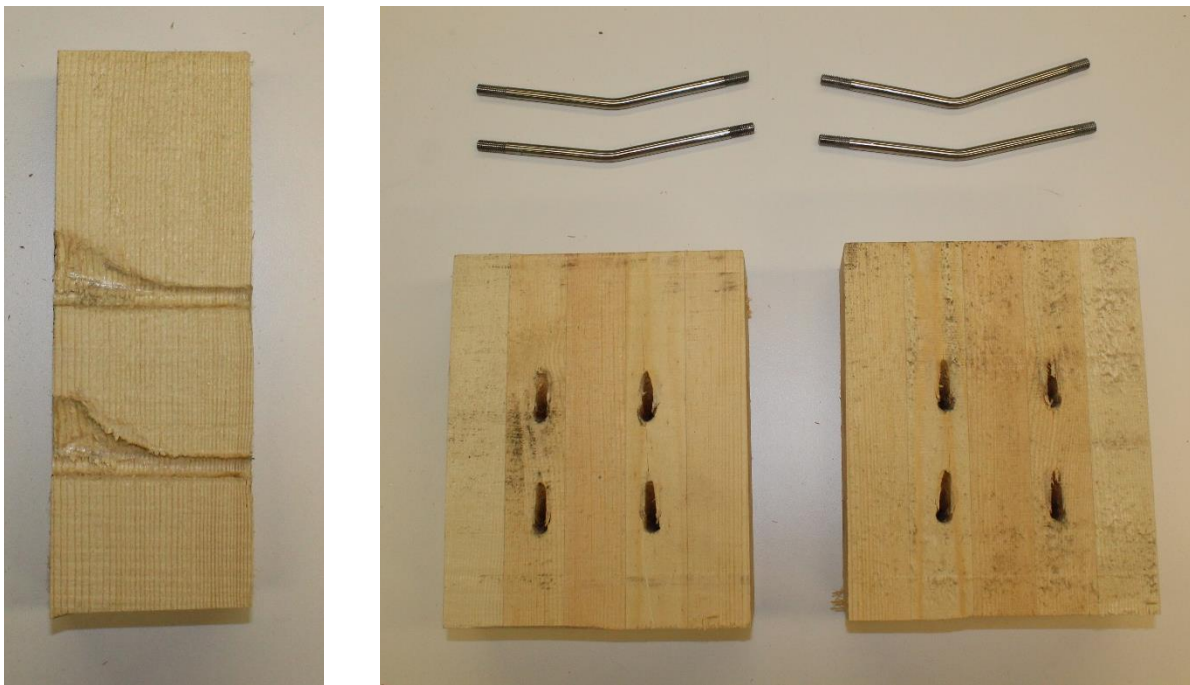

Figure B.35: Force-Displacement Relationship for Specimen 4SC3

a.) Wood Crushing   b.) Embedment and Damaged Bolts

Figure B.36: Pictures of Damage on Specimen 4SC3

4NM1 [4 bolts, Nitinol, Monotonic, Test #1]: Used all data points.

Figure B.37: Force-Displacement Relationship for Specimen 4NM1

a.) Wood Crushing   b.) Embedment and Bent Bolts

Figure B.38: Pictures of Damage on Specimen 4NM1

4NM2 [4 bolts, Nitinol, Monotonic, Test #2]: Used average of every 50 data points.
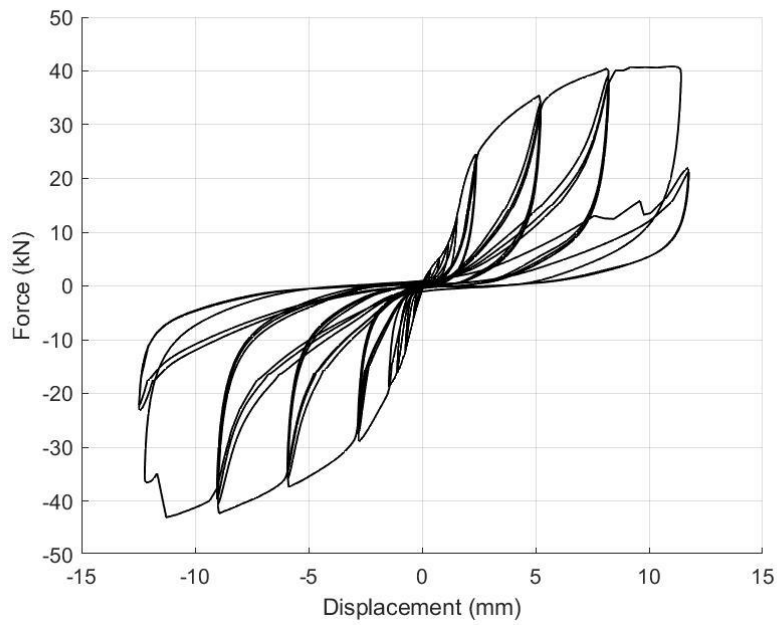

Figure B.39: Force-Displacement Relationship for Specimen 4NM2

a.) Wood Crushing   b.) Embedment and Damaged Bolts

Figure B.40: Pictures of Damage on Specimen 4NM2

4NM3 [4 bolts, Nitinol, Monotonic, Test #3]: Used average of every 50 data points.

Figure B.41: Force-Displacement Relationship for Specimen 4NM3

a.) Wood Crushing   b.) Embedment and Damaged Bolts

Figure B.42: Pictures of Damage on Specimen 4NM3

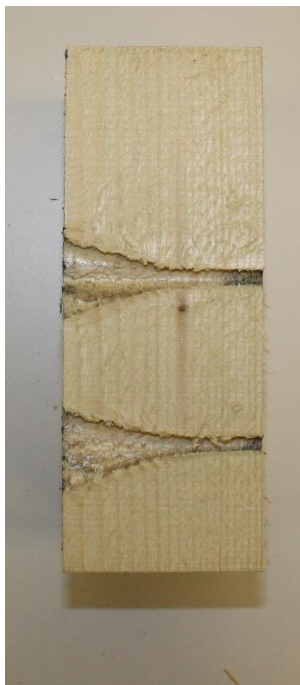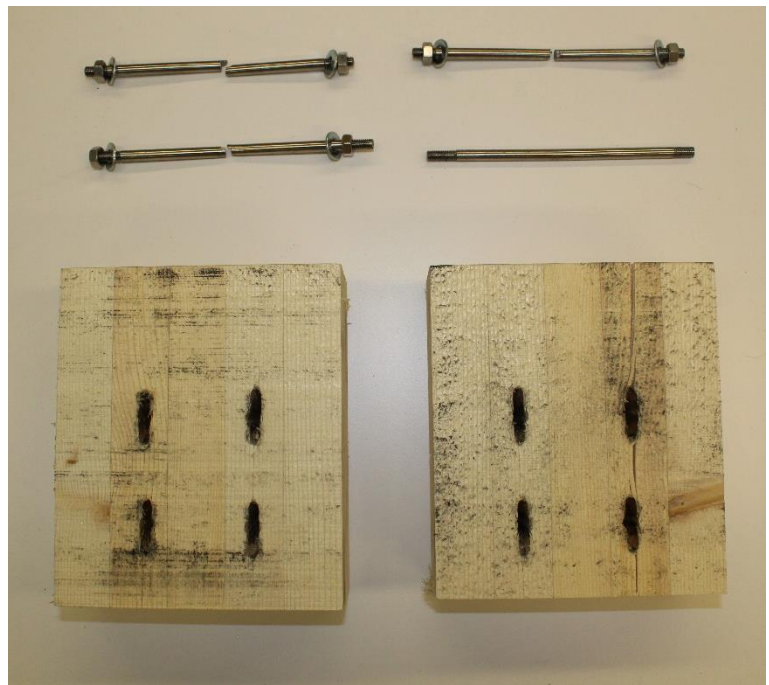**4NC1 [4 bolts, Nitinol, Cyclic, Test #1]:** Average of every 25 data points.

Figure B.43: Force-Displacement Relationship for Specimen 4NC1

a.) Wood Crushing   b.) Embedment and Damaged Bolts

Figure B.44: Pictures of Damage on Specimen 4NC1

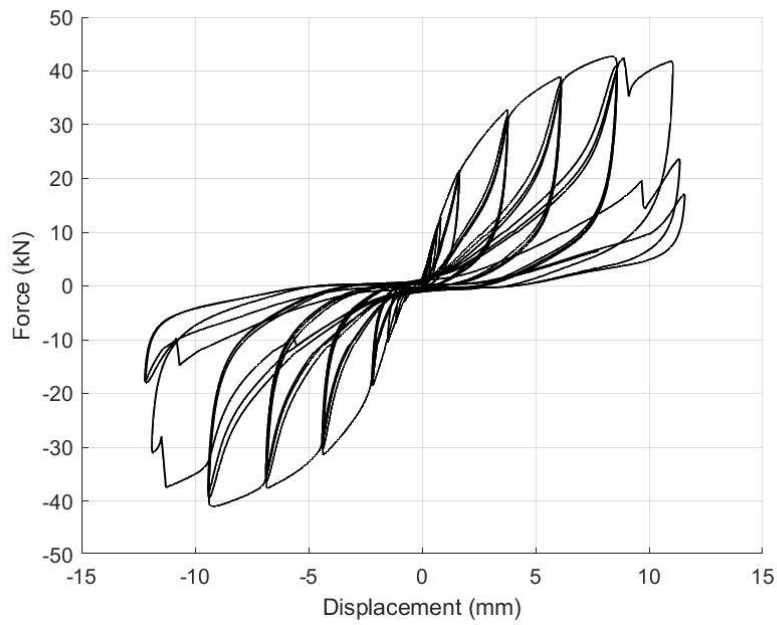**4NC2 [4 bolts, Nitinol, Cyclic, Test #2]:** Average of every 5 data points.

Figure B.45: Force-Displacement Relationship for Specimen 4NC2

a.) Wood Crushing   b.) Embedment and Damaged Bolts

Figure B.46: Pictures of Damage on Specimen 4NC2

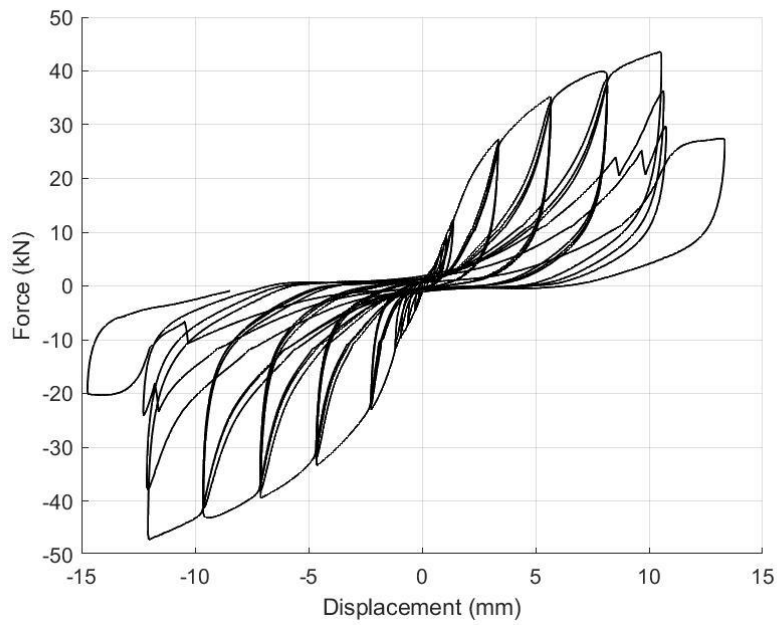**4NC3 [4 bolts, Nitinol, Cyclic, Test #3]:** Average of every 5 data points.
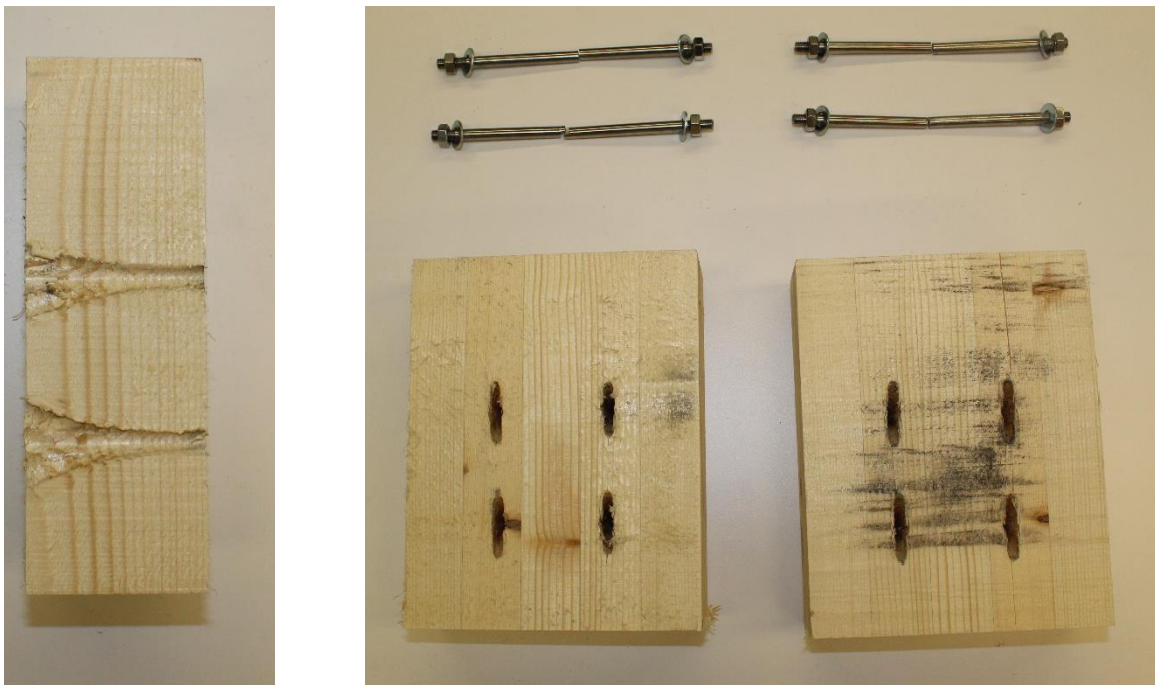

Figure B.47: Force-Displacement Relationship for Specimen 4NC3

a.) Wood Crushing   b.) Embedment and Damaged Bolts

Figure B.48: Pictures of Damage on Specimen 4NC3